

# Overflow metabolism originates from growth optimization and cell heterogeneity

Xin Wang<sup>1,\*</sup>

<sup>1</sup>School of Physics, Sun Yat-sen University, Guangzhou 510275, China

\*Correspondence and requests for materials should be addressed to X.W.  
(Email: wangxin36@mail.sysu.edu.cn).

**Keywords:** Warburg effect, overflow metabolism, aerobic glycolysis, heterogeneity, optimality, metabolic network, extrinsic noise

## Abstract

A classic problem in metabolism is that fast-proliferating cells use the seemingly wasteful fermentation pathway to generate energy in the presence of sufficient oxygen. This counterintuitive phenomenon, known as overflow metabolism or the Warburg effect in cancer, is universal across a wide range of organisms, including bacteria, fungi and mammalian cells. Despite nearly a century of research and with intense interest over the past 20 years, the origin and function of this phenomenon remain unclear. Here, we take *Escherichia coli* as a typical example, and show that overflow metabolism can be understood from growth optimization combined with cell heterogeneity. A model of optimal protein allocation joining with the cell heterogeneity embedded in enzyme catalytic rates quantitatively explains why and how the cell makes the choice between respiration and fermentation in different nutrient conditions. In particular, our model quantitatively illustrates the growth rate dependence of fermentation flux and enzyme allocation under various types of perturbations, which are fully verified by experimental results. Our work solves the long-standing puzzle of overflow metabolism and can be broadly used to explain heterogeneity in cell metabolism.

A prominent feature of cancer metabolism is that tumor cells excrete large quantities of fermentation products in the presence of sufficient oxygen<sup>1-4</sup>. This process, which was discovered by Otto Warburg in the 1920s<sup>5,6</sup>, known as the Warburg effect<sup>1-4</sup>, aerobic glycolysis<sup>1-4</sup> or overflow metabolism<sup>7</sup>, is ubiquitous for fast-proliferating cells across a broad spectrum of organisms<sup>1,7</sup>, ranging from bacteria<sup>7-11</sup>, fungi<sup>12</sup> to mammalian cells<sup>1-4</sup>. For microbes, cells use the standard respiration when nutrients are scarce<sup>1,7</sup>, while they use the counterintuitive aerobic glycolysis when nutrients are adequate<sup>1,7</sup>, just analogous to the normal tissues and cancer cells, respectively<sup>1</sup>. Over the past century, with extensive studies in the past two decades<sup>4</sup>, various rationales of overflow metabolism have been proposed<sup>1,7,13-24</sup>. In particular, Basan *et al.*<sup>7</sup> provided a systematic characterization of this process, including various types of perturbations in experiments. However, the origin and function of overflow metabolism still remain unclear<sup>1-4,25</sup>.

Why have microbes and cancer cells evolved to possess the seemly wasteful aerobic glycolysis strategy? For unicellular organisms, there is evolutionary pressure<sup>1</sup> to optimize cellular resources for rapid growth<sup>26-33</sup>. In particular, it has been shown that cells allocate protein resource for optimal growth<sup>26,28,29,33</sup>, and the most efficient protein allocation corresponds to elementary flux mode<sup>34-36</sup>. In this study, we extend these approaches in a heterogeneous framework to address the puzzle of aerobic glycolysis. We use *Escherichia coli* as a typical example and show that overflow metabolism can be understood from optimal protein allocation further combined with the heterogeneity embedded in enzyme catalytic rates. The optimal growth strategy varies between respiration and fermentation depending on the availability and types of the nutrient, and the combination with cell heterogeneity results in the standard picture<sup>7,9-11</sup> of overflow metabolism. Our model quantitatively illustrates the growth rate dependence of fermentation/respiration fluxes and enzyme allocation under various types of perturbations, and can be used to explain the Warburg effect in tumor cells.

## Results

### Coarse-grained model of carbon source utilization

Based on the topology of metabolic network<sup>8,37</sup> (Fig. 1a), we classify the carbon sources joining from the upper part of glycolysis into Group A<sup>28</sup>, and the precursors of biomass components (amino acids *et al.*) into five pools (see SI. Sec. 1.2 for details): a1 (entry point: G6P/F6P), a2 (entry point: GA3P/3PG/PEP), b (entry point: pyruvate/acetyl-CoA), c (entry point:  $\alpha$ -ketoglutarate) and d (entry point: oxaloacetate). Pools a1 and a2 are lumped summed as Pool a due to joint synthesis of precursors. Then, the metabolic network for Group A carbon source utilization (see Fig. 1a) is coarse-grained into a model shown in Fig. 1b (see SI Sec. 2.1 for details), where node *A* represents an arbitrary source of Group A. Evidently, Fig. 1b is topologically identical to Fig. 1a. Each coarse-grained arrow in Fig. 1b carries a stoichiometric flux  $J_i$ , which delivers carbon flux and may consume or produce energy (e.g.,  $J_1$ ,  $J_{a1}$ , see Figs. 1a-b and S1a).

In fact, the stoichiometric flux  $J_i$  scales with the cell population. For comparison with experiments, we define the normalized flux  $J_i^{(N)} \equiv J_i \cdot m_0 / M_{\text{carbon}}$ , which can be regarded as the flux per biomass (see SI Sec. 1.3-1.4 for details). Here,  $M_{\text{carbon}}$  represents the carbon mass of the cell population and  $m_0$  is the weighted average carbon mass of metabolite molecules at the entrance of precursor pools (see Eq. S17). Then, the cell growth rate  $\lambda$  can be represented by  $\lambda = \sum_i^{a1,a2,b,c,d} J_i^{(N)}$  (see SI Sec. 1.4), and the normalized fluxes of respiration and fermentation are  $J_r^{(N)} \equiv J_4^{(N)}$  and  $J_f^{(N)} \equiv J_6^{(N)}$ , respectively. In practice, each  $J_i^{(N)}$  is characterized by two quantities: the proteomic mass fraction  $\phi_i$  of the enzyme that dedicated to carry the flux and the substrate quality  $\kappa_i$  so that  $J_i^{(N)} = \phi_i \cdot \kappa_i$ . We take the Michaelis-Menten form for the enzyme kinetics,  $\kappa_i \equiv k_i \cdot \frac{[S_i]}{[S_i] + K_i}$  and then  $\kappa_i \approx k_i$  (see Eq. S12 and SI Sec. 1.4 for details), where  $[S_i]$  is the concentration of substrate  $S_i$ . For each intermediate node and reaction along the pathway (e.g., node  $M_1$  in  $J_{a1}$ ), the substrate quality  $\kappa_i$  can be approximated as a constant (see SI Sec. 1.5):  $\kappa_i \equiv k_i \cdot \frac{[S_i]}{[S_i] + K_i} \approx k_i$ , where  $[S_i] \geq K_i$  generally holds true in bacteria<sup>38,39</sup>. However,  $\kappa_A$  is a variable, which depends on the concentration and nutrient type of a Group A carbon source (see Eq. S27).

Generically, there are three distinct destinies of a Group A carbon source in the metabolic network (Fig. S2): fermentation, respiration, and biomass generation. Each draws a proteome fraction of  $\phi_f$ ,  $\phi_r$  and  $\phi_{\text{BM}}$ . The net effect of the first two destinies is energy production, while the last one generates precursors of biomass accompanied by energy production. By applying the proteomic constraint<sup>29</sup> that there is a maximum fraction  $\phi_{\text{max}}$  for proteome allocation ( $\phi_{\text{max}} \approx 0.48$ <sup>29</sup>), we have

$$\phi_f + \phi_r + \phi_{\text{BM}} = \phi_{\text{max}} \quad . \quad (1)$$

In fact, Eq.1 is equivalent to  $\phi_R + \phi_A + \sum_{j=1}^6 \phi_j + \sum_i^{a1,a2,b,c,d} \phi_i = \phi_{\text{max}}$  (see SI Sec. 2.1), where  $\phi_R$  stands for the mass fraction of the active ribosome-affiliated protein. In cell proliferation, ribosomes constitute the majority of enzymes for protein synthesis<sup>8,37</sup>, while other biomass components such as RNA are optimally produced<sup>40,41</sup> following the growth rate set by protein synthesis. Thus,  $\lambda = \phi_R \cdot \kappa_t$ , where  $\kappa_t$  is a parameter determined by translation rate<sup>29</sup> (see SI Sec. 1.1 for details), which can be approximated as a constant in the growth rate range of concern<sup>42</sup>.

For balanced cell growth, the energy demand is generically proportional to the biomass production rate. Thus, the normalized energy production rate  $J_E^{(N)}$  is proportional to growth rate  $\lambda$  (see SI Sec. 2.1 for details):

$$J_E^{(N)} = \eta_E \cdot \lambda, \quad (2)$$

where  $\eta_E$  is the energy coefficient. By converting all the energy currencies into ATPs, the normalized energy fluxes of respiration and fermentation are  $J_r^{(E)} = \beta_r^{(A)} \cdot J_r^{(N)} / 2$  and  $J_f^{(E)} = \beta_f^{(A)} \cdot J_f^{(N)} / 2$ , where  $\beta_r^{(A)}$  and  $\beta_f^{(A)}$  are the stoichiometric coefficients of ATP production per glucose in each pathway (see Fig. S2 and SI Sec. 2.1 for details). The denominator coefficient (“2”) is derived from the stoichiometry of the coarse-grained reaction  $M_1 \rightarrow 2M_2$  (Fig. 1a-b). Using flux balance analysis at each intermediate node ( $M_i$ ,  $i=1, \dots, 5$ ) and precursor pool (Pool  $i$ ,  $i=a1, a2, b, c, d$ ), combined with the constraints of proteome allocation (Eq. 1) and energy demand (Eq. 2), we obtain the relations between energy fluxes and growth rate for a given nutrient condition with fixed  $\kappa_A$  (see SI Sec. 2.1 for details):

$$\begin{cases} J_r^{(E)} + J_f^{(E)} = \varphi \cdot \lambda, \\ \frac{J_r^{(E)}}{\varepsilon_r} + \frac{J_f^{(E)}}{\varepsilon_f} = \phi_{\max} - \psi \cdot \lambda, \end{cases} \quad (3)$$

where  $\varphi$  is a constant coefficient mainly determined by  $\eta_E$  (see Eq. S33), and  $\varphi \cdot \lambda$  represents the normalized energy demand other than biomass pathway. The coefficients  $\psi$ ,  $\varepsilon_r$  and  $\varepsilon_f$  are all functions of  $\kappa_A$ .  $\psi^{-1}$  is the proteome efficiency of biomass pathway (see Eq. S32), with  $\psi^{-1} \equiv \lambda / \phi_{\text{BM}}$ .  $\varepsilon_r$  and  $\varepsilon_f$  are the proteome energy efficiencies of the respiration and fermentation pathways, with  $\varepsilon_r \equiv J_r^{(E)} / \phi_r$  and  $\varepsilon_f \equiv J_f^{(E)} / \phi_f$ :

$$\begin{cases} \varepsilon_r = \frac{\beta_r^{(A)}}{1/\kappa_A + 1/\kappa_r^{(A)}}, \\ \varepsilon_f = \frac{\beta_f^{(A)}}{1/\kappa_A + 1/\kappa_f^{(A)}}, \end{cases} \quad (4)$$

where both  $\kappa_r^{(A)}$  and  $\kappa_f^{(A)}$  are constants, with  $1/\kappa_r^{(A)} \equiv 1/\kappa_1 + 2/\kappa_2 + 2/\kappa_3 + 2/\kappa_4$  and  $1/\kappa_f^{(A)} \equiv 1/\kappa_1 + 2/\kappa_2 + 2/\kappa_6$  (see SI Sec. 2.1 for details).

## Origin of overflow metabolism

The standard picture of overflow metabolism<sup>7,9-11</sup> is exemplified by the experimental data<sup>7</sup> shown in Fig. 1c: the fermentation flux exhibits a threshold-analog dependence on growth rate  $\lambda$ . It is well known that respiration is far more efficient than fermentation in terms of the energy production per carbon (i.e.,  $\beta_r^{(A)} > \beta_f^{(A)}$ )<sup>1,37</sup>. Then, why do cells bother to use the seemingly wasteful fermentation pathway? Influential rationales<sup>7,14</sup> hold that the proteome efficiency of fermentation is higher than that of respiration (i.e.,  $\varepsilon_f > \varepsilon_r$ ) and thus cells use fermentation for optimal growth. If so, why do cells use respiration when they are growing slow<sup>4</sup>? We proceed to solve these puzzles using the optimal protein allocation hypothesis<sup>26,29</sup>.

For cell proliferation in a given nutrient with fixed  $\kappa_A$ , the values of  $\varepsilon_r$ ,  $\varepsilon_f$  and  $\psi$  are determined (Eqs. 4 and S32), yet the growth rate  $\lambda$  can be influenced by protein allocation between  $\phi_r$  and  $\phi_f$  with the governing equation: Eq.3. If  $\varepsilon_f < \varepsilon_r$ , then  $\lambda = \frac{\phi_{\max} - J_f^{(E)}(1/\varepsilon_f - 1/\varepsilon_r)}{\psi + \varphi/\varepsilon_r} \leq \frac{\phi_{\max}}{\psi + \varphi/\varepsilon_r}$ . The optimal solution is  $\phi_f = J_f^{(E)} = 0$ , which means that the cell only use respiration. Conversely, if  $\varepsilon_f > \varepsilon_r$ ,  $\phi_r = J_r^{(E)} = 0$  is optimal and the cell only use fermentation. In either case, the optimal choice between respiration and fermentation is determined by weighing the proteome energy efficiencies.

In practice, both  $\varepsilon_r$  and  $\varepsilon_f$  are functions of  $\kappa_A$  (Eq. 4), and thus the optimal choice may change depending on the nutrient conditions. In nutrient-poor conditions where  $\kappa_A \ll \kappa_r^{(A)}, \kappa_f^{(A)}$ , the proteome energy efficiencies are reduced to  $\varepsilon_r \approx \beta_r^{(A)} \cdot \kappa_A$  and  $\varepsilon_f \approx \beta_f^{(A)} \cdot \kappa_A$  (see Eqs. 4), with  $\varepsilon_r(\kappa_A) > \varepsilon_f(\kappa_A)$ . In rich medium, however, using the parameters of  $\kappa_i$  deduced from the in vivo/ in vitro experimental data of *Escherichia coli* (Table S1, see also SI Sec. 6.1-6.2 and Table S2), we verifies that  $\varepsilon_r(\kappa_{\text{glucose}}^{(\text{ST})}) < \varepsilon_f(\kappa_{\text{glucose}}^{(\text{ST})})$  with Eq. 4 (see also Eqs. S39-S40), where  $\kappa_{\text{glucose}}^{(\text{ST})}$  is the substrate quality of glucose at saturated concentration (short as “ST” in the superscript). Indeed, recent experimental studies confirmed that  $\varepsilon_r(\kappa_{\text{lactose}}^{(\text{ST})}) < \varepsilon_f(\kappa_{\text{lactose}}^{(\text{ST})})$  for lactose<sup>7</sup>. In Fig. 1e, we show the growth rate dependence of proteome energy efficiencies  $\varepsilon_r$  and  $\varepsilon_f$  in a 3-dimensional (3D) form using the data shown in Table S1, where  $\varepsilon_r$ ,  $\varepsilon_f$  and the growth rate  $\lambda$  all vary as functions of  $\kappa_A$ . Therefore, the ratio  $\varepsilon_f/\varepsilon_r$  (defined as  $\Delta(\kappa_A)$ ) is a monotonically increasing function of  $\kappa_A$ , and there exists a critical value of  $\kappa_A$  (denote as  $\kappa_A^{(\text{C})}$ ,

see SI Sec. 2.2 for details) satisfying  $\Delta(\kappa_A^{(C)}) = 1$ . Below which, the cell grows slow and the optimal choice is respiration (with  $\varepsilon_f < \varepsilon_r$ ,  $\lambda = \phi_{\max} \cdot (\psi + \varphi/\varepsilon_r)^{-1}$ ), while above  $\kappa_A^{(C)}$ , the cell grows faster and the optimal growth strategy is fermentation (with  $\varepsilon_f > \varepsilon_r$ ,  $\lambda = \phi_{\max} \cdot (\psi + \varphi/\varepsilon_f)^{-1}$ ). The above analysis qualitatively explains the phenomenon of aerobic glycolysis.

For a quantitative understanding of overflow metabolism, let us first consider the homogenous case that all cells share identical biochemical parameters. For optimal protein allocation, the relation between fermentation flux and growth rate is  $J_f^{(E)} = \varphi \cdot \lambda \cdot \theta(\lambda - \lambda_c)$ , where “ $\theta$ ” is the Heaviside step function, and  $\lambda_c$  is the critical growth rate for  $\kappa_A^{(C)}$  (i.e.,  $\lambda_c \equiv \lambda(\kappa_A^{(C)})$ ). Similarly, we obtain the growth rate dependence of respiration flux:  $J_r^{(E)} = \varphi \cdot \lambda \cdot [1 - \theta(\lambda - \lambda_c)]$ . These digital response results are consistent with a well-known study<sup>13</sup> using numerical simulations. However, they are clearly incompatible with the threshold-analog response in the standard picture of overflow metabolism<sup>7,9-11</sup>.

To resolve this issue, we take into account cell heterogeneity, which is ubiquitous in both microbes<sup>43-49</sup> and tumor cells<sup>2,3,50-52</sup>. For the Warburg effect or overflow metabolism of our concern, experimental studies reported significant metabolic heterogeneity in the choice between respiration and fermentation within a cell population<sup>46,47,50,51</sup>. Motivated by the fact that the turnover number ( $k_{\text{cat}}$  value) of a catalytic enzyme varies considerably between the in vitro and in vivo measurements<sup>53,54</sup>, we note that the concentrations of potassium and phosphate, which vary from cell to cell, have a significant impact on the  $k_{\text{cat}}$  values of the metabolic enzymes<sup>54</sup>. Therefore, in a cell population, there is a distribution of values for a  $k_{\text{cat}}$ , which is commonly referred to as extrinsic noise<sup>55</sup>. For simplicity, we assume that each  $k_{\text{cat}}$  value follows a Gaussian distribution. This gives the distributions of single-cell growth rate in various types of carbon sources (see Eqs. S155, S157, S163-S165), which are full verified by recent experiments using isogenic *Escherichia coli* with single-cell resolution<sup>45</sup> (see Fig. S3b for details). Then, the critical growth rate  $\lambda_c$  should follow a Gaussian distribution  $\mathcal{N}(\mu_{\lambda_c}, \sigma_{\lambda_c}^2)$  in the cell population (see SI Sec. 7 for details), where  $\mu_{\lambda_c}$  is approximated by the deterministic result of  $\lambda_c$  (Eq. S43), and we assume that the coefficient of variance (CV) is  $\sigma_{\lambda_c}/\mu_{\lambda_c} = 12\%$ , or equivalently, the CV for the catalytic rate of each metabolic enzyme is 25%. Thus, we have the growth rate dependence of fermentation and respiration fluxes (see SI Sec. 2.3 for details):

$$\begin{cases} J_f^{(N)}(\lambda) = \frac{\varphi \cdot \lambda}{\beta_f^{(A)}} \cdot \left[ \operatorname{erf}\left(\frac{\lambda - \mu_{\lambda_c}}{\sqrt{2}\sigma_{\lambda_c}}\right) + 1 \right], \\ J_r^{(N)}(\lambda) = \frac{\varphi \cdot \lambda}{\beta_r^{(A)}} \cdot \left[ 1 - \operatorname{erf}\left(\frac{\lambda - \mu_{\lambda_c}}{\sqrt{2}\sigma_{\lambda_c}}\right) \right], \end{cases} \quad (5)$$

where “erf” represents the error function. The fermentation flux exhibits a threshold-analog relation with the growth rate (see the red curves in Figs. 1c-d, 2b-c and 3b, d, f), while the respiration flux (the blue curve in Fig. 1d) decreases with the increase of fermentation flux. In Fig.1c-d, we see that the model results (see Eq.5 and SI Sec. 8, parameters are set by the experimental data shown in Table S1) agree quantitatively with the experimental results of *Escherichia coli*<sup>7,11</sup>, where the fermentation flux was determined by the acetate secretion rate  $J_{ac}^{(N)} = 2J_f^{(N)}$ , and the respiration flux was deduced from the carbon dioxide flux  $J_{CO_2,r}^{(N)} = 6J_r^{(N)}$  (see SI Sec. 8.1 for details). Thus, with the integration of cell heterogeneity, our model of optimal protein allocation quantitatively explains overflow metabolism.

### Testing the model through perturbations

To further test our model, we systematically investigate model predictions under various types of perturbations and compare them with the experimental data from existing studies (see SI Secs.3 and 4.1 for details).

First, we consider the proteomic perturbations by overexpression of useless proteins encoded by the LacZ gene (i.e.,  $\phi_z$  perturbations) in *Escherichia coli*. The net effect of  $\phi_z$  perturbations is that the maximum fraction of proteome available for resource allocation changes from  $\phi_{max}$  to  $\phi_{max} - \phi_z$ <sup>7</sup>, where  $\phi_z$  is the mass fraction of useless protein. In a cell population, the critical growth rate  $\lambda_c(\phi_z)$  still follows a Gaussian distribution  $\mathcal{N}(\mu_{\lambda_c}(\phi_z), \sigma_{\lambda_c}(\phi_z)^2)$ , where the CV of  $\lambda_c(\phi_z)$  remain unchanged. Consequently, the growth rate dependence of fermentation flux

changes into  $J_f^{(N)} = \frac{\varphi \cdot \lambda}{\beta_f^{(A)}} \cdot \left[ \operatorname{erf}\left(\frac{\lambda - \mu_{\lambda_c}(\phi_z)}{\sqrt{2}\sigma_{\lambda_c}(\phi_z)}\right) + 1 \right]$  (see SI Sec. 3 for model perturbations of respiration flux), where both the growth rate  $\lambda(\kappa_A, \phi_z)$  and the normalized fermentation flux  $J_f^{(N)}(\kappa_A, \phi_z)$  are bivariate functions of  $\kappa_A$  and  $\phi_z$  (see Eqs. S49 and S56-S57). For each degree of LacZ expression (with fixed  $\phi_z$ ), just like the wild type strains, the fermentation flux exhibits a threshold-analog response to growth rate as  $\kappa_A$  varies (Fig.2c), which agrees quantitatively

with experimental results<sup>7</sup>. The shifts in the critical growth rate  $\lambda_c(\phi_z)$  are fully captured by  $\mu_{\lambda_c}(\phi_z) = \mu_{\lambda_c}(0)(1 - \phi_z/\phi_{\max})$ . In contrast, for nutrient conditions with each fixed  $\kappa_A$ , since cell growth rate changes with  $\phi_z$  just like  $\lambda_c(\phi_z)$  :  $\lambda(\kappa_A, \phi_z) = \lambda(\kappa_A, 0)(1 - \phi_z/\phi_{\max})$  , the fermentation flux is then proportional to growth rate for the varying levels of LacZ expression:

$$J_f^{(N)} = \frac{\varphi}{\beta_f^{(A)}} \cdot \left[ \operatorname{erf} \left( \frac{\lambda(\kappa_A, 0) - \mu_{\lambda_c}(0)}{\sqrt{2}\sigma_{\lambda_c}(0)} \right) + 1 \right] \cdot \lambda$$

, where the slope is an increasing function of substrate quality  $\kappa_A$ . These results of scaling relations are well validated by the experimental data<sup>7</sup> shown in Fig. 2b. Finally, in the case that both  $\kappa_A$  and  $\phi_z$  are free to vary, the growth rate dependence of fermentation flux presents a threshold-analog response surface in a 3D plot where  $\phi_z$  appears explicitly as the y-axis (Fig. 2a). Experimental data points<sup>7</sup> lie right on this surface (Fig. 2a), which are highly consistent with the model predictions.

Next, we study the influences of energy dissipation, whose net effect is to introduce a energy dissipation coefficient  $w$  into Eq. 2:  $J_E^{(N)} = \eta_E \cdot \lambda + w$ . Likewise, the critical growth rate  $\lambda_c(w)$

follows a Gaussian distribution  $\mathcal{N}(\mu_{\lambda_c}(w), \sigma_{\lambda_c}(w)^2)$  in a cell population, and the relation between growth rate and fermentation flux is characterized by (see SI Sec. 3.2 for details):

$$J_f^{(N)} = \frac{\varphi \cdot \lambda + w}{\beta_f^{(A)}} \cdot \left[ \operatorname{erf} \left( \frac{\lambda - \mu_{\lambda_c}(w)}{\sqrt{2}\sigma_{\lambda_c}(w)^2} \right) + 1 \right]$$

. In Fig. 3a-b, we show the comparison between the model results and experimental data<sup>7</sup> in 3D and 2D plots, which demonstrate good agreement. A prominent feature of energy dissipation distinguished from  $\phi_z$  perturbations is that when  $\kappa_A$  is fixed, the fermentation flux increases despite a decrease in growth rate.

We proceed to analyze the impacts of translation inhibition with different sub-lethal doses of chloramphenicol for *Escherichia coli*. This type of perturbations introduce an inhibition coefficient  $\iota$  in the translation rate, thus turning  $\kappa_t$  into  $\kappa_t/(\iota+1)$ . Still, the critical growth rate  $\lambda_c(\iota)$  follows a Gaussian distribution  $\mathcal{N}(\mu_{\lambda_c}(\iota), \sigma_{\lambda_c}(\iota)^2)$  , and then, the growth rate

$$J_f^{(N)} = \frac{\varphi \cdot \lambda}{\beta_f^{(A)}} \cdot \left[ \operatorname{erf} \left( \frac{\lambda - \mu_{\lambda_c}(\iota)}{\sqrt{2}\sigma_{\lambda_c}(\iota)} \right) + 1 \right]$$

dependence of fermentation flux is: (see SI Sec. 3.3 for details). In Fig. S4, we see that the model predictions are generally consistent with the experimental data<sup>7</sup>. However, there is a noticeable systematic discrepancy when the translation rate is small. Thus, we turn to maintenance energy (with the coefficient  $w_0$ ), which is tiny and

generically negligible in bacteria over the growth rate range of concern<sup>7,56</sup>. Encouragingly, by assigning a very small value to the maintenance energy coefficient  $w_0$  ( $w_0 = 2.5$ ), the model

$$J_f^{(N)} = \frac{\varphi \cdot \lambda + w_0}{\beta_f^{(A)}} \cdot \left[ \operatorname{erf} \left( \frac{\lambda - \mu_{\lambda_c}(\iota)}{\sqrt{2}\sigma_{\lambda_c}(\iota)} \right) + 1 \right]$$

results of the growth rate-fermentation flux relation

agrees quantitatively with experiments<sup>7</sup> (see Fig. 3c-d and SI Sec. 3.3 for details).

Finally, we consider the nutrient category alternation by switching to a non-Group A carbon source: pyruvate, which enters the metabolic network from the end point of glycolysis<sup>8,37</sup>. The coarse-grained model for pyruvate utilization is shown in Fig. 3e (see also Fig. 1a), which shares identical precursor pools as that for Group A carbon sources (Fig. 1b), yet with several differences in the coarse-grained reactions. The growth rate dependence of both the proteome energy efficiencies (Fig. S8c) and energy fluxes present similar forms to those of Group A carbon source utilization, while they are quantitatively different in the coarse-grained parameters (see SI Secs. 4.1 and Sec. 8 for details). Most notably, the critical growth rate  $\lambda_c^{(py)}$  and the ATP production per glucose in the fermentation pathway  $\beta_f^{(py)}$  are noticeably smaller than  $\lambda_c$  and  $\beta_f^{(A)}$  (for Group A sources). Consequently, the growth rate dependence of fermentation flux in pyruvate should present a quite different curve from that of Group A carbon sources (see Eqs. 5 and S105), which are fully validated by experimental results<sup>11</sup> (Fig. 3f).

### Enzyme allocation under growth perturbations

As mentioned above, our coarse-grained model is topologically identical to the central metabolic network (Fig. 1a), and thus it can predict enzyme allocation for each gene in glycolysis and the TCA cycle (see Fig. S1b and Table S1) under various type of perturbations. In Fig. 1b, the intermediate nodes  $M1, M2, M3, M4$ , and  $M5$  stand for G6P, PEP, acetyl-CoA,  $\alpha$ -ketoglutarate, and oxaloacetate, respectively. Then,  $\phi_1$  and  $\phi_2$  correspond to enzymes of glycolysis (or at the junction of glycolysis and the TCA cycle), while  $\phi_3$  and  $\phi_4$  correspond to enzymes in the TCA cycle.

We first consider enzyme allocation under carbon limitation by varying the nutrient type and concentration of a Group A carbon source (i.e.,  $\kappa_A$  perturbations). In fact, this has been extensively studied by more simplified models<sup>26,33</sup>, and the growth rate dependence of enzyme allocation under  $\kappa_A$  perturbations was generally thought to be a C-line response<sup>26,33</sup> that genes responsible for digesting carbon compounds show a linear increase in gene expression as the growth rate decreases<sup>26,33</sup>. However, by collecting the experimental data for metabolic enzymes from existing studies<sup>33</sup>, we find that the enzymes in glycolysis show a completely different response pattern from that of enzymes in the TCA cycle (see Fig. S5a-b), which clearly cannot be explained by the C-line response. To address this issue, we apply the coarse-grained model

described above (Fig. 1b) to calculate the growth rate dependence of enzyme allocation for each  $\phi_i$  ( $i=1,2,3,4$ ) with the same model settings for wild type strains, where no fitting parameters are involved (see Eqs. S118-S119 and Sec.8). In Figs. 4a-b and S5c-d, we see that the model predictions overall match with the experimental data<sup>33</sup> for representative genes from either glycolysis or the TCA cycle, and maintenance energy (with  $w_0 = 2.5$ ) makes negligible effect in this process. Still, there are minor discrepancies stem from the basal expression of metabolic genes, which may be attributed to that our model deals with relatively stable growth conditions while microbes need to be prepared for fluctuating environments<sup>57-59</sup>.

We proceed to analyze the influences of  $\phi_z$  perturbations and energy dissipation. In both cases, our model predicts a linear response to growth rate reduction for all genes in either glycolysis or the TCA cycle (see SI Sec. 5.2-5.3 for details). For  $\phi_z$  perturbations, all the predicted slopes are positive, and there is no fitting parameters involved (see Eqs. S120-S121). In Figs. 4c-d and S6, we show that our model quantitatively illustrates the experimental data<sup>7</sup> for representative genes in the central metabolic network, and there is a better agreement with experiments<sup>7</sup> by incorporating the maintenance energy (with  $w_0 = 2.5$ ). For energy dissipation, however, the predicted slopes of the enzymes corresponding to  $\phi_4$  are surely negative, and there is a constraint that the slope sign of the enzymes corresponding to the same  $\phi_i$  ( $i=1,2,3$ ) should be the same. In Fig. S7, we see that the model results (see Eqs. S127 and S123) are consistent with experiments<sup>7</sup>.

## Discussion

The phenomenon of overflow metabolism, or the Warburg effect is a long-standing puzzle in cell metabolism. Over the past century, although many rationales have been proposed<sup>1,7,13-24</sup>, the origin and function of this phenomenon remain unclear<sup>1-4,25</sup>. Here, we take *Escherichia coli* as a typical example and show that overflow metabolism can be understood from optimal protein allocation combined with cell heterogeneity. In nutrient-poor conditions, the proteome energy efficiency of respiration is higher than that of fermentation (Fig.1e), and thus the cell use respiration to optimize growth. In rich medium, however, the proteome energy efficiency of fermentation increases faster and thus is higher than that of respiration (Fig.1e), then, the cell use fermentation to accelerate growth. In further combination with cell heterogeneity embedded in enzyme catalytic rates<sup>53,54</sup>, our model quantitatively illustrates the threshold-analog response<sup>7,11</sup> in overflow metabolism (Fig.1c).

In fact, the standard picture of overflow metabolism<sup>7,9-11</sup> was mostly illustrated by a threshold-linear response in existing rationales<sup>7,14,16,17,20</sup>, which optimize cell growth rate at a given rate of carbon influx (or some equivalents), and regard the proteome energy efficiencies as constants (see SI Sec. 6.3 for details). In practice, however, for microbes or tumor cells grown in vitro or in vivo, the given factors are the type and concentration of nutrients<sup>29</sup> rather than the rate of carbon influx, and the proteome energy efficiencies vary significantly with the substrate quality  $\kappa_A$

(Fig.1e). Our model is completely different from these rationales in the optimization principles that we purely optimize cell growth rate without further constraint on the carbon influx (see SI Sec. 6.3 for details).

Cell heterogeneity is crucial for the threshold-analog response in overflow metabolism, without which (i.e., the homogenous case) the optimal solution is a digital response (see Eq. S44) that corresponds to elementary flux mode<sup>34,35</sup> and agrees with a notable numerical study<sup>13</sup>. However, the digital response is incompatible with the standard picture of overflow metabolism<sup>7,9-11</sup>. In this study, we show that the heterogeneity embedded in enzyme catalytic rates<sup>53,54</sup> changes the critical growth rate (i.e., threshold,  $\lambda_c$ ) from a single value into a Gaussian distribution (Eq. 45, see SI Sec. 7 for details) for a cell population, and thus turning a digital response into the threshold-analog response in overflow metabolism (Fig.1c). Our model results relying on cell heterogeneity are fully validated by the observed distributions of sing-cell growth rate<sup>45</sup> (Fig. S3b) and experiments with various types of perturbations<sup>7,11,33</sup>, for both acetate secretion patterns and gene expression in the central metabolic network (Figs. 2-4 and S4-S7).

Finally, our model can be broadly used to explain heterogeneity in cell metabolism on a quantitative basis, including the Crabtree effect in yeast<sup>12,47</sup>, the Warburg effect in cancer<sup>14,50</sup> (see SI Sec. 6.4 for explanation of the Warburg effect), and the heterogenous metabolic strategies under various types of environment<sup>28,44,47,50,51,60</sup>.

## References

- 1 Vander Heiden, M. G., Cantley, L. C. & Thompson, C. B. Understanding the Warburg effect: the metabolic requirements of cell proliferation. *Science* **324**, 1029-1033 (2009).
- 2 Hanahan, D. & Weinberg, R. A. Hallmarks of cancer: the next generation. *Cell* **144**, 646-674 (2011).
- 3 Pavlova, N. N., Zhu, J. & Thompson, C. B. The hallmarks of cancer metabolism: Still emerging. *Cell Metabolism* (2022).
- 4 Liberti, M. V. & Locasale, J. W. The Warburg effect: how does it benefit cancer cells? *Trends in Biochemical Sciences* **41**, 211-218 (2016).
- 5 Warburg, O., Posener, K. & Negelein, E. The metabolism of cancer cells. *Biochem. Zeitschrift* **152**, 319-344 (1924).
- 6 Warburg, O. The metabolism of carcinoma cells. *The Journal of Cancer Research* **9**, 148-163 (1925).
- 7 Basan, M. *et al.* Overflow metabolism in Escherichia coli results from efficient proteome allocation. *Nature* **528**, 99-104 (2015).
- 8 Neidhardt, F. C., Ingraham, J. L. & Schaechter, M. *Physiology of the bacterial cell*. (Sinauer associates, 1990).

9 Nanchen, A., Schicker, A., Sauer, U. J. A. & microbiology, e. Nonlinear dependency of intracellular fluxes on growth rate in miniaturized continuous cultures of *Escherichia coli*. *Applied Environmental Microbiology* **72**, 1164-1172 (2006).

10 Meyer, H.-P., Leist, C. & Fiechter, A. Acetate formation in continuous culture of *Escherichia coli* K12 D1 on defined and complex media. *Journal of Biotechnology* **1**, 355-358 (1984).

11 Holms, H. Flux analysis and control of the central metabolic pathways in *Escherichia coli*. *FEMS Microbiology Reviews* **19**, 85-116 (1996).

12 De Deken, R. The Crabtree effect: a regulatory system in yeast. *Microbiology* **44**, 149-156 (1966).

13 Molenaar, D., Van Berlo, R., De Ridder, D. & Teusink, B. Shifts in growth strategies reflect tradeoffs in cellular economics. *Molecular Systems Biology* **5**, 323 (2009).

14 Chen, Y. & Nielsen, J. Energy metabolism controls phenotypes by protein efficiency and allocation. *Proceedings of the National Academy of Sciences* **116**, 17592-17597 (2019).

15 Niebel, B., Leupold, S. & Heinemann, M. An upper limit on Gibbs energy dissipation governs cellular metabolism. *Nature Metabolism* **1**, 125-132 (2019).

16 Majewski, R. & Domach, M. Simple constrained-optimization view of acetate overflow in *E. coli*. *Biotechnology Bioengineering* **35**, 732-738 (1990).

17 Shlomi, T., Benyaminini, T., Gottlieb, E., Sharan, R. & Ruppin, E. Genome-scale metabolic modeling elucidates the role of proliferative adaptation in causing the Warburg effect. *PLoS Computational Biology* **7**, e1002018 (2011).

18 Zhuang, K., Vemuri, G. N. & Mahadevan, R. Economics of membrane occupancy and respiro-fermentation. *Molecular Systems Biology* **7**, 500 (2011).

19 Varma, A. & Palsson, B. O. Stoichiometric flux balance models quantitatively predict growth and metabolic by-product secretion in wild-type *Escherichia coli* W3110. *Applied Environmental Microbiology* **60**, 3724-3731 (1994).

20 Vazquez, A. & Oltvai, Z. N. Macromolecular crowding explains overflow metabolism in cells. *Scientific Reports* **6**, 31007 (2016).

21 Dai, Z., Shestov, A. A., Lai, L. & Locasale, J. W. A flux balance of glucose metabolism clarifies the requirements of the Warburg effect. *Biophysical Journal* **111**, 1088-1100 (2016).

22 Sánchez, B. J. *et al.* Improving the phenotype predictions of a yeast genome-scale metabolic model by incorporating enzymatic constraints. *Molecular Systems Biology* **13**, 935 (2017).

23 Vazquez, A., Liu, J., Zhou, Y. & Oltvai, Z. N. Catabolic efficiency of aerobic glycolysis: the Warburg effect revisited. *BMC Systems Biology* **4**, 1-9 (2010).

24 Pfeiffer, T., Schuster, S. & Bonhoeffer, S. Cooperation and competition in the evolution of ATP-producing pathways. *Science* **292**, 504-507 (2001).

25 DeBerardinis, R. J. & Chandel, N. We need to talk about the Warburg effect. *Nature Metabolism* **2**, 127-129 (2020).

26 You, C. *et al.* Coordination of bacterial proteome with metabolism by cyclic AMP signalling. *Nature* **500**, 301-306 (2013).

27 Li, S. H.-J. *et al.* Escherichia coli translation strategies differ across carbon, nitrogen and phosphorus limitation conditions. *Nature Microbiology* **3**, 939-947 (2018).

28 Wang, X., Xia, K., Yang, X. & Tang, C. Growth strategy of microbes on mixed carbon sources. *Nature Communications* **10**, 1279 (2019).

29 Scott, M., Gunderson, C. W., Mateescu, E. M., Zhang, Z. & Hwa, T. Interdependence of cell growth and gene expression: origins and consequences. *Science* **330**, 1099-1102 (2010).

30 Edwards, J. S., Ibarra, R. U. & Palsson, B. O. In silico predictions of Escherichia coli metabolic capabilities are consistent with experimental data. *Nature biotechnology* **19**, 125-130 (2001).

31 Dekel, E. & Alon, U. Optimality and evolutionary tuning of the expression level of a protein. *Nature* **436**, 588-592 (2005).

32 Towbin, B. D. *et al.* Optimality and sub-optimality in a bacterial growth law. *Nature Communications* **8**, 14123 (2017).

33 Hui, S. *et al.* Quantitative proteomic analysis reveals a simple strategy of global resource allocation in bacteria. *Molecular Systems Biology* **11**, 784 (2015).

34 Müller, S., Regensburger, G. & Steuer, R. Enzyme allocation problems in kinetic metabolic networks: Optimal solutions are elementary flux modes. *Journal of Theoretical Biology* **347**, 182-190 (2014).

35 Wortel, M. T., Peters, H., Hulshof, J., Teusink, B. & Bruggeman, F. J. Metabolic states with maximal specific rate carry flux through an elementary flux mode. *The FEBS Journal* **281**, 1547-1555 (2014).

36 Schuster, S. & Hilgetag, C. On elementary flux modes in biochemical reaction systems at steady state. *Journal of Biological Systems* **2**, 165-182 (1994).

37 Nelson, D. L., Lehninger, A. L. & Cox, M. M. *Lehninger principles of biochemistry*. (Macmillan, 2008).

38 Bennett, B. D. *et al.* Absolute metabolite concentrations and implied enzyme active site occupancy in Escherichia coli. *Nature Chemical Biology* **5**, 593-599 (2009).

39 Park, J. O. *et al.* Metabolite concentrations, fluxes and free energies imply efficient enzyme usage. *Nature Chemical Biology* **12**, 482-489 (2016).

40 Kostinski, S. & Reuveni, S. Ribosome composition maximizes cellular growth rates in E. coli. *Physical Review Letters* **125**, 028103 (2020).

41 Reuveni, S., Ehrenberg, M. & Paulsson, J. Ribosomes are optimized for autocatalytic production. *Nature* **547**, 293-297 (2017).

42 Dai, X. *et al.* Reduction of translating ribosomes enables Escherichia coli to maintain elongation rates during slow growth. *Nature Microbiology* **2**, 1-9 (2016).

43 Ackermann, M. A functional perspective on phenotypic heterogeneity in microorganisms. *Nature Reviews Microbiology* **13**, 497-508 (2015).

44 Solopova, A. *et al.* Bet-hedging during bacterial diauxic shift. *Proceedings of the National Academy of Sciences* **111**, 7427-7432 (2014).

45 Wallden, M., Fange, D., Lundius, E. G., Baltekin, Ö. & Elf, J. The synchronization of replication and division cycles in individual *E. coli* cells. *Cell* **166**, 729-739 (2016).

46 Nikolic, N., Barner, T. & Ackermann, M. Analysis of fluorescent reporters indicates heterogeneity in glucose uptake and utilization in clonal bacterial populations. *BMC Microbiology* **13**, 1-13 (2013).

47 Bagamery, L. E., Justman, Q. A., Garner, E. C. & Murray, A. W. A putative bet-hedging strategy buffers budding yeast against environmental instability. *Current Biology* **30**, 4563-4578. e4564 (2020).

48 Takhayev, V. & Heinemann, M. Metabolic heterogeneity in clonal microbial populations. *Current Opinion in Microbiology* **45**, 30-38 (2018).

49 Balaban, N. Q., Merrin, J., Chait, R., Kowalik, L. & Leibler, S. Bacterial persistence as a phenotypic switch. *Science* **305**, 1622-1625 (2004).

50 Duraj, T. *et al.* Beyond the Warburg effect: Oxidative and glycolytic phenotypes coexist within the metabolic heterogeneity of glioblastoma. *Cells* **10**, 202 (2021).

51 Hensley, C. T. *et al.* Metabolic heterogeneity in human lung tumors. *Cell* **164**, 681-694 (2016).

52 Almendro, V., Marusyk, A. & Polyak, K. Cellular heterogeneity and molecular evolution in cancer. *Annual Review of Pathology: Mechanisms of Disease* **8**, 277-302 (2013).

53 Davidi, D. *et al.* Global characterization of in vivo enzyme catalytic rates and their correspondence to in vitro kcat measurements. *Proceedings of the National Academy of Sciences* **113**, 3401-3406 (2016).

54 García-Contreras, R., Vos, P., Westerhoff, H. V. & Boogerd, F. C. Why in vivo may not equal in vitro—new effectors revealed by measurement of enzymatic activities under the same in vivo-like assay conditions. *The FEBS Journal* **279**, 4145-4159 (2012).

55 Elowitz, M. B., Levine, A. J., Siggia, E. D. & Swain, P. S. Stochastic gene expression in a single cell. *Science* **297**, 1183-1186 (2002).

56 Neidhardt, F. C. *Escherichia coli and Salmonella: cellular and molecular biology*. (ASM Press, 1996).

57 Mori, M., Schink, S., Erickson, D. W., Gerland, U. & Hwa, T. Quantifying the benefit of a proteome reserve in fluctuating environments. *Nature Communications* **8**, 1225 (2017).

58 Basan, M. *et al.* A universal trade-off between growth and lag in fluctuating environments. *Nature* **584**, 470-474 (2020).

59 Kussell, E. & Leibler, S. Phenotypic diversity, population growth, and information in fluctuating environments. *Science* **309**, 2075-2078 (2005).

60 Escalante-Chong, R. *et al.* Galactose metabolic genes in yeast respond to a ratio of galactose and glucose. *Proceedings of the National Academy of Sciences* **112**, 1636-1641 (2015).

## **Acknowledgements**

The author thanks Chao Tang and Kang Xia for helpful discussions. This work was supported by National Natural Science Foundation of China (Grant No.12004443), Guangzhou Municipal Innovation Fund (Grant No.202102020284) and the Hundred Talents Program of Sun Yat-sen University.

## **Author contributions**

X.W. conceived and designed the project, developed the model, carried out the analytical/numerical calculations, and wrote the paper.

## **Competing interests**

The author declares no competing interests.

## Figures

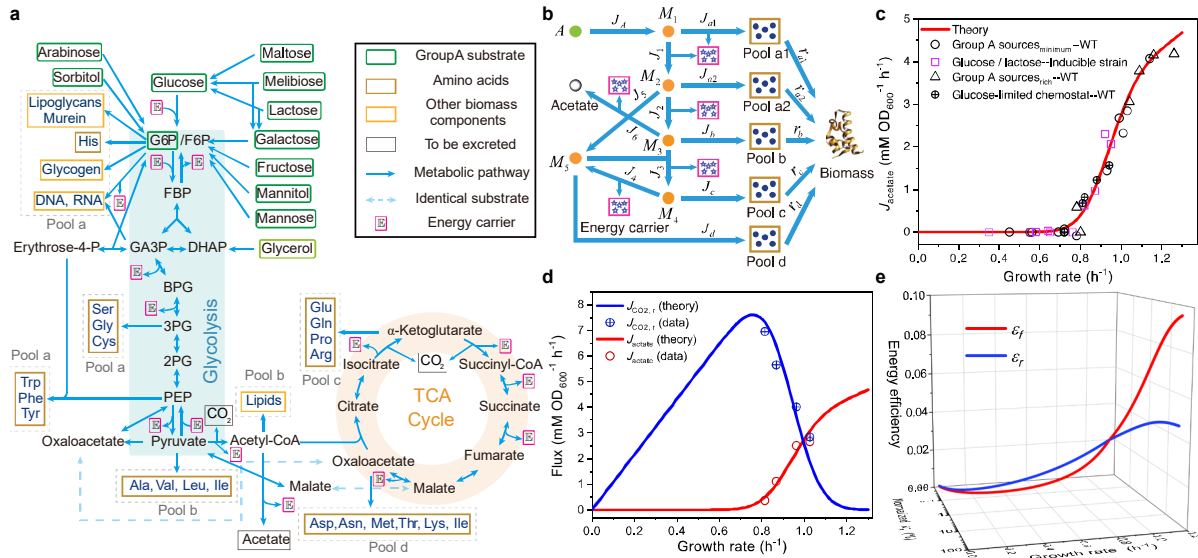


Fig. 1 | The model and results of overflow metabolism.

(a) The central metabolic network of carbon source utilization. The Group A carbon sources<sup>28</sup> are labeled with green squares. (b) The coarse-grained model for Group A carbon source utilization. (c) Model predictions (Eqs. S47 and S160) and experimental results<sup>7,11</sup> of overflow metabolism, covering the data for all the Group A carbon sources shown in (a). (d) Growth rate dependence of the respiration and fermentation fluxes (Eqs. S47 and S160). (e) The energy efficiencies of respiration and fermentation pathway vary with the growth rate as functions of the substrate quality of a Group A carbon source (Eq. S31). See SI Sec. 8 for model parameter settings and experimental data sources<sup>7,11,33</sup> of Figs.1-4. See also Figs. S1-S3 and S8.

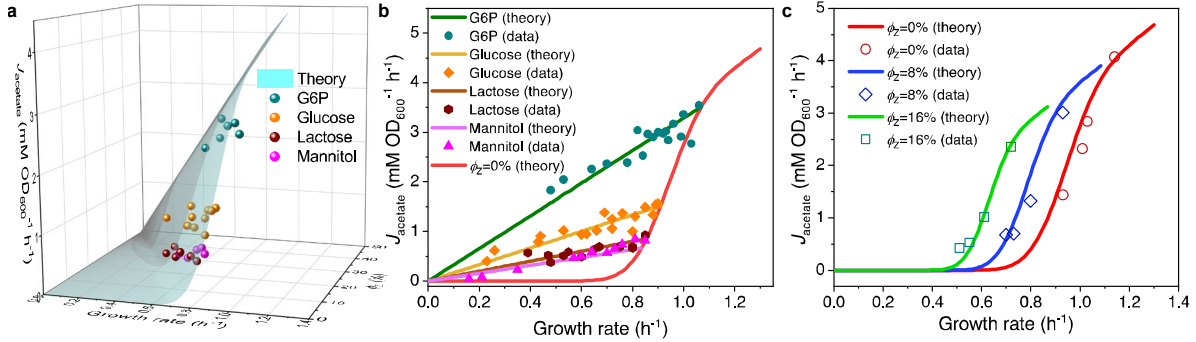


Fig. 2 | Influence of protein overexpression on overflow metabolism.

(a) 3D plot of the relations among fermentation flux, growth rate and the expression level of the useless proteins. Here, both the acetate excretion rate and growth rate vary as bivariate functions of the substrate quality of a Group A carbon source ( $K_A$ ) and the useless protein expression encoded by LacZ ( $\phi_z$  perturbations, see Eqs. S57 and S160). (b) For each fixed nutrient condition, the acetate excretion rate is proportional to growth rate upon  $\phi_z$  perturbations (Eq. S58 and S160), where the slope is a monotonically increasing function of  $K_A$ . (c) The grow rate dependence of acetate excretion rate as  $K_A$  varies, with each fixed expression level of LacZ.

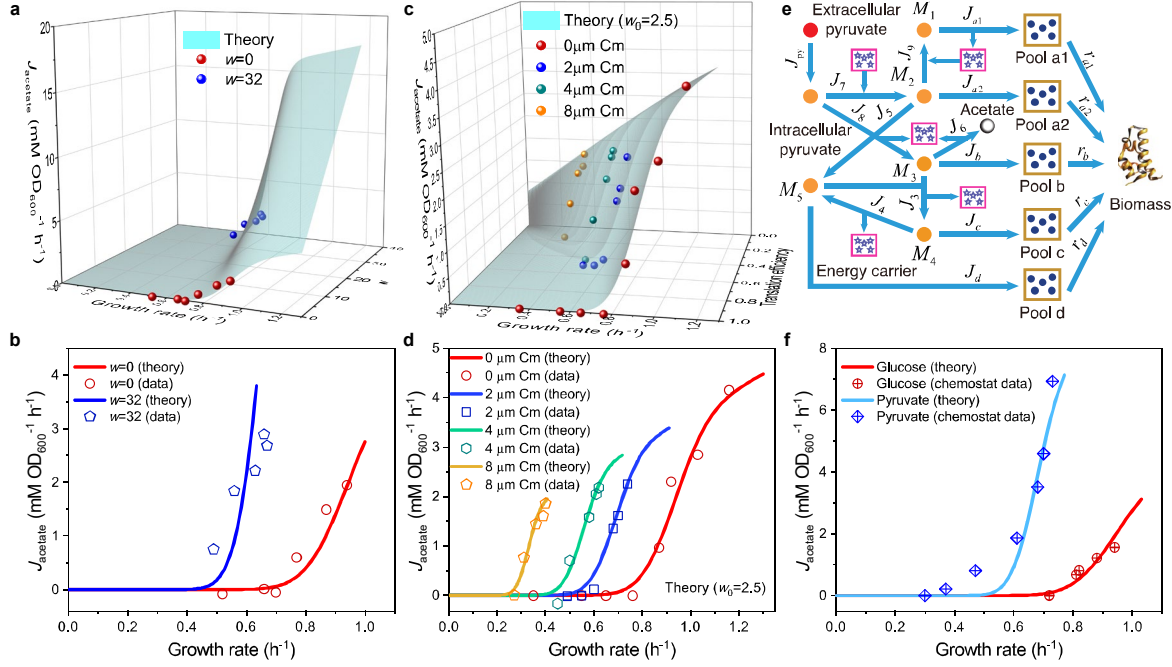


Fig. 3 | Influences of energy dissipation, translation inhibition, and carbon source category alternation on overflow metabolism.

(a) 3D plot of the relations among fermentation flux, growth rate and the energy dissipation coefficient (Eqs. S70 and S160). (b) The grow rate dependence of acetate excretion rate as  $K_A$  varies, with each fixed energy dissipation coefficient determined by/fitted from experimental data. (c) 3D plot of the relations among fermentation flux, growth rate and the translation efficiency (Eqs. 85 and S160, see also Fig. S4). Here, the translation efficiency is tuned by the dose of chloramphenicol (Cm). (d) The grow rate dependence of acetate excretion rate as  $K_A$  varies, with each fixed dose of Cm. (e) The coarse-grained model of pyruvate utilization. (f) The growth rate dependence of the fermentation flux in pyruvate (Eqs. 105 and S160) is significantly different from that of the Group A carbon sources (Eqs. 47 and S160). See also Figs. S4 and S8.

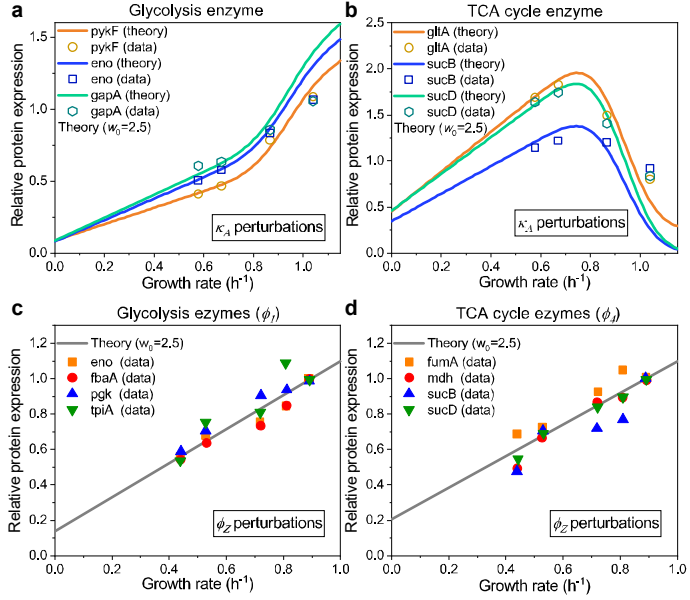


Fig. 4 | The relative protein expression of central metabolic enzymes under  $\kappa_A$  and  $\phi_z$  perturbations.

(a, c) The relative protein expression of representative genes from glycolysis. (b, d) The relative protein expression of representative genes from the TCA cycle. (a-b) The results of  $\kappa_A$  perturbations (Eq. S119, see also Fig. S5). (c-d) The results of  $\phi_z$  perturbations (Eq. S121, see also Fig. S6). See Fig. S7 for the results upon energy dissipation. See also Figs. S5-S6.

# Overflow metabolism originates from growth optimization and cell heterogeneity

## Supplementary information

Xin Wang

S1 Model framework .....	1
S1.1 Proteome partition.....	1
S1.2 Precursor pools .....	1
S1.3 Stoichiometric flux .....	2
S1.4 Carbon flux and cell growth rate .....	3
S1.5 Intermediate nodes.....	4
S2 Model and analysis .....	4
S2.1 Coarse-grained model.....	4
S2.2 The reason for overflow metabolism .....	7
S2.3 The relations between overflow fluxes and growth rate .....	9
S3 Model perturbations.....	11
S3.1 Overexpression of useless proteins.....	11
S3.2 Energy dissipation.....	14
S3.3 Translation inhibition.....	16
S4 Overflow metabolism in substrates other than Group A carbon sources.....	20
S4.1 Pyruvate .....	20
S4.2 Mixtures of a Group A carbon source with extracellular amino acids .....	24
S5 Enzyme allocation upon perturbations .....	27
S5.1 Carbon limitation within Group A carbon sources .....	27
S5.2 Overexpression of useless proteins.....	28
S5.3 Energy dissipation.....	29
S6 Other aspects of the model.....	31
S6.1 A coarse-grained model with more details .....	31
S6.2 Estimation of the in vivo enzyme catalytic rates .....	32
S6.3 Comparisons with existing models that illustrate experimental results.....	33

S6.4 The explanation for the Warburg effect in tumor cells .....	34
S7 Probability density functions of the variables and parameters .....	35
S7.1 Probability density functions of $\kappa_i$ .....	35
S7.2 Probability density function of the growth rate $\lambda$ .....	38
S8 Model comparisons with experiments .....	39
S8.1 Fluxes comparisons with experiments .....	39
S8.2 Model parameter settings using experimental data.....	40
S8.3 Notes on the applications of the reference data .....	43
Supplementary References.....	45
Supplementary Tables.....	48
Table S1. Molecular weight (MW) and in vivo/ in vitro $k_{\text{cat}}$ data of <i>E. coli</i> . .....	48
Table S2. Proteome and flux data <sup>10</sup> used to calculate the in vivo $k_{\text{cat}}$ .....	50
Supplementary Figures .....	51
Fig. S1. Details of the central metabolic network.....	51
Fig. S2. Three destinies of glucose metabolism.....	51
Fig. S3. Model analysis for carbon utilization in mixtures with amino acids.....	52
Fig. S4. Influences of translation inhibition on overflow metabolism.....	52
Fig. S5. The relative protein expression of central metabolic enzymes under $\kappa_A$ perturbations .....	53
Fig. S6. The relative protein expression of central metabolic enzymes under $\phi_Z$ perturbations .....	54
Fig. S7. The relative protein expression of central metabolic enzymes upon energy dissipation.....	55
Fig. S8. A coarse-grained model for experimental comparisons.....	56
Fig. S9. Asymptotic distributions of inverse Gaussian distribution and the inverse of Gaussian distribution.....	56

## S1 Model framework

### S1.1 Proteome partition

Here we adopt the proteome partition framework similar to that introduced by Scott *et al.*<sup>1</sup>. All proteins of a cell are classified into three classes: fixed portion Q-class, active ribosome-affiliated R-class, and the remainder catabolic/anabolic enzymes C-class. Each proteome class is of mass  $M_i^{(p)}$  ( $i = Q, R, C$ ) and mass fraction  $\phi_i$ , where  $\phi_Q$  is a constant, and we define  $\phi_{\max} \equiv 1 - \phi_Q$ . In the exponential growth phase, the ribosome allocation for protein synthesize of each class is  $f_i$ , with  $f_Q + f_R + f_C = 1$ . To analyze cell growth optimization, first we consider the homogenous case that all cells share identical biochemical parameters and simplify the mass accumulation of a cell population into a big cell. Basically, this approximation would not influence the value of growth rate  $\lambda$ . For bacteria, the protein turnover rate is negligible, and then the mass accumulation of each class follows:

$$dM_i^{(p)}/dt = f_i \cdot k_T \cdot N_R \cdot m_{AA} \quad (i = Q, R, C), \quad (S1)$$

where  $m_{AA}$  stands for the averaged molecular weight of amino acids,  $k_T$  is the translation rate,  $N_R = M_{rp}^{(p)} / m_R$  is the number of ribosomes,  $m_R$  is the protein mass of a single ribosome, and  $M_{rp}^{(p)}$  is the protein mass of the ribosomes with  $M_R^{(p)} / M_{rp}^{(p)} = \varsigma \approx 1.67$ <sup>1,2</sup>. For a specific stable nutrient environment,  $f_R$  and  $k_T$  are temporal invariants. Then,

$$M_i^{(p)}(t) = M_i^{(p)}(0) + f_i / f_R \cdot M_R^{(p)}(0) \cdot [\exp(\lambda \cdot t) - 1] \quad (i = Q, R, C), \quad (S2)$$

where  $\lambda = f_R \cdot k_T \cdot m_{AA} / (\varsigma \cdot m_R)$ , and the protein mass of the cell population follows

$$M_{\text{protein}}(t) = M_{\text{protein}}(0) + M_R(0) \cdot [\exp(\lambda \cdot t) - 1] / f_R. \quad (S3)$$

Over a long period in the exponential growth phase ( $t \rightarrow +\infty$ ),  $\phi_i = f_i$  ( $i = Q, R, C$ ) and

$$\lambda = \phi_R \cdot \kappa_t, \quad (S4)$$

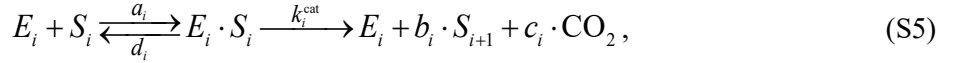
where  $\kappa_t = k_T \cdot m_{AA} / (\varsigma \cdot m_R)$ . For microbes, cells optimize growth rate to survive in the evolution process.

### S1.2 Precursor pools

Based on the entry point of the metabolic network, we classify the precursors of biomass components into five pools (Fig. 1a-b): a1 (entry point: G6P/F6P), a2 (entry point: GA3P/3PG/PEP), b (entry point: pyruvate/acetyl-CoA), c (entry point:  $\alpha$ -ketoglutarate) and d (entry point: oxaloacetate). For bacteria, these five pools draw roughly  $r_{a1} = 24\%$ ,  $r_{a2} = 24\%$ ,  $r_b = 28\%$ ,  $r_c = 12\%$  and  $r_d = 12\%$  of the carbon flux<sup>3,4</sup>. There are overlapping components between Pools a1, a2 due to the joint synthesis of some precursors, thus we also use Pool a to represent Pools a1-a2 in the descriptions.

### S1.3 Stoichiometric flux

We consider the following biochemical reaction between substrate  $S_i$  and enzyme  $E_i$ :



where  $a_i$ ,  $d_i$  and  $k_i^{\text{cat}}$  are the reaction parameters,  $S_{i+1}$  is the product,  $b_i$  and  $c_i$  are the stoichiometric coefficients. For most of the reactions in the central metabolism,  $b_i = 1$  and  $c_i = 0$ . The reaction rate follows Michaelis–Menten kinetics<sup>3</sup>:

$$v_i = k_i^{\text{cat}} \cdot [E_i] \cdot \frac{[S_i]}{[S_i] + K_i}, \quad (\text{S6})$$

where  $K_i \equiv (d_i + k_i^{\text{cat}})/a_i$ ,  $[E_i]$  and  $[S_i]$  are the concentrations of enzyme  $E_i$  and substrate  $S_i$ , respectively. For this reaction (Eq. S5),  $d[S_{i+1}]/dt = b_i \cdot v_i$  and  $d[S_i]/dt = -v_i$ . In the cell populations (the “big cell”), suppose that the cell volume is  $V_{\text{cell}}$ , then, the stoichiometric flux of the reaction is

$$J_i \equiv V_{\text{cell}} \cdot v_i. \quad (\text{S7})$$

The copy number of enzyme  $E_i$  is  $N_{E_i} = V_{\text{cell}} \cdot [E_i]$  with a total weight of  $M_{E_i} = N_{E_i} \cdot m_{E_i}$ , where  $m_{E_i}$  is the molecular weight of  $E_i$ . By defining the enzyme cost of an  $E_i$  molecule as  $n_{E_i} \equiv m_{E_i}/m_0$ , where  $m_0$  is a unit mass, and then the cost of all  $E_i$  molecules are  $\Phi_i \equiv N_{E_i} \cdot n_{E_i}$ <sup>4</sup>. By further defining  $\xi_i \equiv \frac{k_i^{\text{cat}}}{n_{E_i}} \cdot \frac{[S_i]}{[S_i] + K_i}$ , then,

$$J_i = \Phi_i \cdot \xi_i. \quad (\text{S8})$$

The mass fraction of  $E_i$  is  $\phi_i = M_{E_i}/M_{\text{protein}}$ , and thus

$$\phi_i = \Phi_i \cdot \frac{m_0}{M_{\text{protein}}}. \quad (\text{S9})$$

## S1.4 Carbon flux and cell growth rate

To calculate the connection between the stoichiometric flux  $J_i$  and growth rate  $\lambda$ , we consider the carbon flux in the biomass production. The carbon mass of the cell population (the “big cell”) is  $M_{\text{carbon}} = M_{\text{protein}} \cdot r_{\text{carbon}} / r_{\text{protein}}$ , where  $r_{\text{carbon}}$  and  $r_{\text{protein}}$  stand for the mass fraction of the carbon and protein within a cell. In the exponential growth phase, obviously, the carbon flux of the biomass production is:

$$J_{\text{BM}} = \frac{1}{m_{\text{carbon}}} \cdot \frac{dM_{\text{carbon}}}{dt} = \lambda \cdot \frac{M_{\text{carbon}}}{m_{\text{carbon}}}, \quad (\text{S10})$$

where  $m_{\text{carbon}}$  is the mass of a carbon atom. In fact, the carbon mass flux per stoichiometric flux is different depending on the entry point of the precursor pools. Taking Pool b as an example, there are three carbon atoms in a molecule of the entry point metabolite (pyruvate). Assuming that carbon atoms conserve from pyruvate to Pool b, then, the carbon flux of Pool b is  $J_b^{\text{carbon}} = J_b \cdot N_{\text{py}}^{\text{carbon}}$ , where  $J_b$  is the stoichiometric flux from pyruvate to pool b (Fig. 1a-b) and  $N_{\text{py}}^{\text{carbon}}$  stands for the carbon number of a pyruvate molecule. Combined with Eq. S10, and note that  $J_b^{\text{carbon}} = r_b \cdot J_{\text{BM}}$ , then,  $J_b \cdot N_{\text{py}}^{\text{carbon}} \cdot m_{\text{carbon}} = r_b \cdot \lambda \cdot M_{\text{carbon}}$ . Similarly, for each precursor pool, we have

$$J_i \cdot N_{\text{EP}_i}^{\text{carbon}} \cdot m_{\text{carbon}} = r_i \cdot \lambda \cdot M_{\text{carbon}} \quad (i = a1, a2, b, c, d), \quad (\text{S11})$$

where the subscript “ $\text{EP}_i$ ” represents the entry point of Pool  $i$ , and  $N_{\text{EP}_i}^{\text{carbon}}$  stands for the number of carbon atoms in a molecule of the entry point metabolite. Here, for every substrate in the intermediate steps of the metabolic network, we define  $\kappa_i$  as the substrate quality:

$$\kappa_i \equiv \xi_i \cdot \frac{r_{\text{protein}}}{r_{\text{carbon}}} = \frac{r_{\text{protein}}}{r_{\text{carbon}}} \cdot \frac{k_i^{\text{cat}}}{n_{E_i}} \cdot \frac{[S_i]}{[S_i] + K_i}, \quad (\text{S12})$$

and for each precursor pool, we define

$$\eta_i \equiv r_i \cdot m_0 / (N_{\text{EP}_i}^{\text{carbon}} \cdot m_{\text{carbon}}) \quad (i = a1, a2, b, c, d). \quad (\text{S13})$$

Combing Eqs. S8, S9, S11, we have

$$\phi_i \cdot \kappa_i = \eta_i \cdot \lambda \quad (i = a1, a2, b, c, d). \quad (\text{S14})$$

Then, we define

$$J_i^{(\text{N})} \equiv \phi_i \cdot \kappa_i, \quad (\text{S15})$$

where the superscript “(N)” stands for normalized. Combined with Eqs. S8, S9, S12, we have

$$J_i^{(N)} \equiv J_i \cdot \frac{m_0}{M_{\text{carbon}}} \quad (\text{S16})$$

Since  $\sum_i^{a1,a2,b,c,d} r_i = 1$ , by setting that

$$m_0 = \left[ \sum_i r_i / N_{\text{EP}_i}^{\text{carbon}} \right]^{-1} \cdot m_{\text{carbon}} \quad (\text{S17})$$

then,

$$\eta_i = \frac{r_i}{N_{\text{EP}_i}^{\text{carbon}}} \cdot \left[ \sum_j^{a1,a2,b,c,d} \frac{r_j}{N_{\text{EP}_j}^{\text{carbon}}} \right]^{-1} \quad (i = a1, a2, b, c, d), \quad (\text{S18})$$

and we have  $\sum_i^{a1,a2,b,c,d} \eta_i = 1$ , and

$$\sum_i^{a1,a2,b,c,d} \phi_i \cdot \kappa_i = \lambda \quad (\text{S19})$$

## S1.5 Intermediate nodes

In a metabolic network, the metabolites between the carbon source and precursor pools are the intermediate nodes. As specified in Wang *et al.*<sup>4</sup>, to optimize cell growth rate, the substrate of each intermediate node is nearly saturated, and thus

$$\kappa_i \approx \frac{r_{\text{protein}}}{r_{\text{carbon}}} \cdot \frac{k_i^{\text{cat}}}{n_{E_i}} \quad (\text{S20})$$

The real cases could be more complicated because of other metabolic regulations. Recent quantitative studies<sup>5,6</sup> show that at least in *E. coli*, for most of the substrate-enzyme pairs  $[S_i] > K_i$ , which implies

$$\kappa_i \approx \frac{r_{\text{protein}}}{r_{\text{carbon}}} \cdot \frac{k_i^{\text{cat}}}{n_{E_i}}$$

## S2 Model and analysis

### S2.1 Coarse-grained model

In the coarse-grained model shown in Fig. 1b, node *A* represents an arbitrary carbon source of Group A<sup>4</sup>, which joins at the upper part of glycolysis. Nodes *M*<sub>1</sub>, *M*<sub>2</sub>, *M*<sub>3</sub>, *M*<sub>4</sub>, *M*<sub>5</sub> stand for G6P, PEP, acetyl-CoA,  $\alpha$ -ketoglutarate, oxaloacetate, respectively. In the analysis of carbon supply into precursor pools, we lump sum G6P/F6P as *M*<sub>1</sub>, GA3P/3PG/PEP as *M*<sub>2</sub>, and pyruvate/acetyl-CoA as *M*<sub>3</sub> for approximation. For the

biochemical reactions, each follows Eq. S5 with  $b_i = 1$  except that  $M_1 \rightarrow 2M_2$  and  $M_3 + M_5 \rightarrow M_4$ . Basically, there are 3 possible destinies of a Group A carbon source (e.g., glucose, see Fig. S2): the energy contributions in the fermentation and respiration pathways (Fig. S2a-b), or the biomass components with accompanied energy production in the biomass pathway (Fig. S2c). By applying flux balance of the stoichiometric fluxes combined with Eq. S8, we have

$$\begin{cases} \Phi_A \cdot \xi_A = \Phi_1 \cdot \xi_1 + \Phi_{a1} \cdot \xi_{a1}, \\ 2\Phi_1 \cdot \xi_1 = \Phi_2 \cdot \xi_2 + \Phi_5 \cdot \xi_5 + \Phi_{a2} \cdot \xi_{a2}, \\ \Phi_2 \cdot \xi_2 = \Phi_3 \cdot \xi_3 + \Phi_6 \cdot \xi_6 + \Phi_b \cdot \xi_b, \\ \Phi_5 \cdot \xi_5 + \Phi_4 \cdot \xi_4 = \Phi_3 \cdot \xi_3 + \Phi_d \cdot \xi_d, \\ \Phi_3 \cdot \xi_3 = \Phi_4 \cdot \xi_4 + \Phi_c \cdot \xi_c. \end{cases} \quad (S21)$$

Obviously, the stoichiometric fluxes of respiration  $J_r$  and fermentation  $J_f$  (Fig. S2a-b) are

$$\begin{cases} J_r \equiv J_4 = \Phi_4 \cdot \xi_4, \\ J_f \equiv J_6 = \Phi_6 \cdot \xi_6. \end{cases} \quad (S22)$$

We further assume that carbon atoms conserve from the entry point metabolite to each precursor pool, and then,

$$\Phi_i \cdot \xi_i \cdot N_{EP_i}^{\text{carbon}} = r_i \cdot J_{\text{BM}} \quad (i = a1, a2, b, c, d). \quad (S23)$$

In terms of the energy production for each of the relevant reaction, for convenience, we convert all the energy currencies into ATPs, namely, NADH $\rightarrow$ 2ATP<sup>7</sup>, NADPH $\rightarrow$ 2ATP<sup>7,8</sup>, FADH<sub>2</sub> $\rightarrow$ 1ATP<sup>7</sup>. Then, we have

$$\beta_1 \cdot \Phi_1 \cdot \xi_1 + \beta_2 \cdot \Phi_2 \cdot \xi_2 + \beta_3 \cdot \Phi_3 \cdot \xi_3 + \beta_4 \cdot \Phi_4 \cdot \xi_4 + \beta_6 \cdot \Phi_6 \cdot \xi_6 + \beta_{a1} \cdot \Phi_{a1} \cdot \xi_{a1} = J_E, \quad (S24)$$

where  $J_E$  represents the stoichiometric flux of ATPs, and  $\beta_i$  is the stoichiometric coefficient with  $\beta_1 = 4$ ,  $\beta_2 = 3$ ,  $\beta_3 = 2$ ,  $\beta_4 = 6$ ,  $\beta_6 = 1$ , and  $\beta_{a1} = 4$ <sup>7,8</sup>. Generically, the energy demand is proportional to the carbon flux infused into biomass production, thus,

$$J_E = r_E \cdot J_{\text{BM}}, \quad (S25)$$

where  $r_E$  is the ratio which is also a constant. By applying the substitution specified in Eqs. S9, S12, S14-S18, combined with Eqs. S4, S10, S21-S25 and the constraint of proteome resource allocation  $\phi_R + \phi_C = \phi_{\max}$ , we have

$$\left\{
\begin{aligned}
\phi_A \cdot \kappa_A &= \phi_1 \cdot \kappa_1 + \phi_{a1} \cdot \kappa_{a1}, \\
2\phi_1 \cdot \kappa_1 &= \phi_2 \cdot \kappa_2 + \phi_5 \cdot \kappa_5 + \phi_{a2} \cdot \kappa_{a2}, \\
\phi_2 \cdot \kappa_2 &= \phi_3 \cdot \kappa_3 + \phi_6 \cdot \kappa_6 + \phi_b \cdot \kappa_b, \\
\phi_5 \cdot \kappa_5 + \phi_4 \cdot \kappa_4 &= \phi_3 \cdot \kappa_3 + \phi_d \cdot \kappa_d, \\
\phi_3 \cdot \kappa_3 &= \phi_4 \cdot \kappa_4 + \phi_c \cdot \kappa_c, \\
\phi_{a1} \cdot \kappa_{a1} &= \eta_{a1} \cdot \lambda, \phi_{a2} \cdot \kappa_{a2} = \eta_{a2} \cdot \lambda, \phi_b \cdot \kappa_b = \eta_b \cdot \lambda, \phi_c \cdot \kappa_c = \eta_c \cdot \lambda, \phi_d \cdot \kappa_d = \eta_d \cdot \lambda, \\
\beta_1 \cdot \phi_1 \cdot \kappa_1 + \beta_2 \cdot \phi_2 \cdot \kappa_2 + \beta_3 \cdot \phi_3 \cdot \kappa_3 + \beta_4 \cdot \phi_4 \cdot \kappa_4 + \beta_6 \cdot \phi_6 \cdot \kappa_6 + \beta_{a1} \cdot \phi_{a1} \cdot \kappa_{a1} &= J_E^{(N)}, \\
J_E^{(N)} &= \eta_E \cdot \lambda, \lambda = \phi_R \cdot \kappa_t, J_r^{(N)} = \phi_4 \cdot \kappa_4, J_f^{(N)} = \phi_6 \cdot \kappa_6, \\
\phi_R + \phi_A + \phi_1 + \phi_2 + \phi_3 + \phi_4 + \phi_5 + \phi_6 + \phi_{a1} + \phi_{a2} + \phi_b + \phi_c + \phi_d &= \phi_{\max},
\end{aligned}
\right. \quad (S26)$$

where  $\eta_E = r_E \cdot \left[ \sum_i r_i / N_{EP_i}^{\text{carbon}} \right]^{-1}$ . Here, for each intermediate node,  $\kappa_i$  follows Eq. S20, which can be approximated as a constant. The substrate quality of the Group A carbon source  $\kappa_A$  varies with the identity and concentration of the Group A carbon source,

$$\kappa_A \equiv \frac{r_{\text{protein}}}{r_{\text{carbon}}} \cdot \frac{k_A^{\text{cat}}}{m_{E_A}} \cdot \frac{[A]}{[A] + K_A} \cdot m_0, \quad (S27)$$

which is determined externally by the culturing environment. From Eq. S26, all  $\phi_i$  can be expressed by  $J_r^{(N)}$ ,  $J_f^{(N)}$ , and  $\lambda$ :

$$\left\{
\begin{aligned}
\phi_A &= \left[ J_r^{(N)} + J_f^{(N)} + (2\eta_{a1} + \eta_{a2} + \eta_b + 2\eta_c + \eta_d) \lambda \right] / (2 \cdot \kappa_A), \\
\phi_1 &= \left[ J_r^{(N)} + J_f^{(N)} + (\eta_{a2} + \eta_b + 2\eta_c + \eta_d) \lambda \right] / (2 \cdot \kappa_1), \\
\phi_2 &= \left[ J_r^{(N)} + J_f^{(N)} + (\eta_b + \eta_c) \lambda \right] / \kappa_2, \\
\phi_3 &= (J_r^{(N)} + \eta_c \cdot \lambda) / \kappa_3, \phi_4 = J_r^{(N)} / \kappa_4, \\
\phi_5 &= (\eta_c + \eta_d) \lambda / \kappa_5, \phi_6 = J_f^{(N)} / \kappa_6, \\
\phi_i &= \eta_i \cdot \lambda / \kappa_i \quad (i = a1, a2, b, c, d).
\end{aligned}
\right. \quad (S28)$$

By substituting Eq. S28 into Eq. S26, we have

$$\left\{
\begin{aligned}
J_r^{(E)} + J_f^{(E)} &= \varphi \cdot \lambda, \\
\frac{J_r^{(E)}}{\varepsilon_r} + \frac{J_f^{(E)}}{\varepsilon_f} &= \phi_{\max} - \psi \cdot \lambda.
\end{aligned}
\right. \quad (S29)$$

Here,  $J_r^{(E)}$  and  $J_f^{(E)}$  stand for the normalized energy fluxes of respiration and fermentation, with

$$\begin{cases} J_r^{(E)} = (\beta_1/2 + \beta_2 + \beta_3 + \beta_4) \cdot J_r^{(N)}, \\ J_f^{(E)} = (\beta_1/2 + \beta_2 + \beta_6) \cdot J_f^{(N)}. \end{cases} \quad (S30)$$

The coefficients  $\varepsilon_r$  and  $\varepsilon_f$  represent the proteome energy efficiencies of the respiration and fermentation pathways (Fig. S2a-b), with

$$\begin{cases} \varepsilon_r = \frac{\beta_1/2 + \beta_2 + \beta_3 + \beta_4}{1/(2\kappa_A) + 1/(2\kappa_1) + 1/\kappa_2 + 1/\kappa_3 + 1/\kappa_4}, \\ \varepsilon_f = \frac{\beta_1/2 + \beta_2 + \beta_6}{1/(2\kappa_A) + 1/(2\kappa_1) + 1/\kappa_2 + 1/\kappa_6}. \end{cases} \quad (S31)$$

$\psi^{-1}$  is the proteome efficiency of biomass pathway (Fig. S2c), with

$$\psi = \frac{1}{\kappa_t} + \frac{1 + \eta_{a1} + \eta_c}{2\kappa_A} + \frac{\eta_{a2} + \eta_b + 2\eta_c + \eta_d}{2\kappa_1} + \frac{\eta_b + \eta_c}{\kappa_2} + \frac{\eta_c}{\kappa_3} + \frac{\eta_c + \eta_d}{\kappa_5} + \sum_i^{a1, a2, b, c, d} \frac{\eta_i}{\kappa_i}. \quad (S32)$$

$\varphi$  is the energy demand coefficient (a constant), with

$$\varphi \equiv \eta_E - \beta_1 \cdot (\eta_{a2} + \eta_b + 2\eta_c + \eta_d)/2 - \beta_2 \cdot (\eta_b + \eta_c) - \beta_3 \cdot \eta_c - \beta_{a1} \cdot \eta_{a1}, \quad (S33)$$

and  $\varphi \cdot \lambda$  stands for the normalized energy demand other than the accompanied energy production of biomass pathway.

## S2.2 The reason for overflow metabolism

Microbes optimize growth rate to survive through the evolutionary history<sup>9</sup>. Basically, this also applies to tumor cells, which proliferate rapidly ignoring the signal of growth constraint<sup>9</sup>. To optimize cell growth, first, we consider the best strategy for a single cell. The coarse-grained model is summarized in Eq. S26

and further simplified into Eq. S29. Basically,  $\varepsilon_r$ ,  $\varepsilon_f$  and  $\psi$  are functions of  $\kappa_A$  (Eqs. S31, S32), and so we also denote them as  $\varepsilon_r(\kappa_A)$ ,  $\varepsilon_f(\kappa_A)$ ,  $\psi(\kappa_A)$ . Obviously, both fluxes of respiration and fermentation takes nonnegative values, i.e.,  $J_r^{(E)}, J_f^{(E)} \geq 0$ , and all the coefficients are positive:  $\varepsilon_r(\kappa_A), \varepsilon_f(\kappa_A), \psi(\kappa_A), \varphi > 0$ .

Thus, if  $\varepsilon_r > \varepsilon_f$ , then  $(\psi + \varphi/\varepsilon_r) \cdot \lambda = \phi_{\max} - J_f^{(E)}(1/\varepsilon_f - 1/\varepsilon_r) \leq \phi_{\max}$ . Obviously, the optimal solution is

$$\begin{cases} J_f^{(E)} = 0, \\ J_r^{(E)} = \varphi \cdot \lambda. \end{cases} \quad \varepsilon_r > \varepsilon_f. \quad (S34)$$

Similarly, if  $\varepsilon_f > \varepsilon_r$ , then the optimal solution is

$$\begin{cases} J_f^{(E)} = \varphi \cdot \lambda, \\ J_r^{(E)} = 0. \end{cases} \quad \varepsilon_r < \varepsilon_f. \quad (S35)$$

In both cases, the growth rate  $\lambda$  takes the maximum value for a given nutrient condition (i.e., given  $\kappa_A$ ):

$$\lambda = \begin{cases} \lambda_r \equiv \frac{\phi_{\max}}{\varphi/\varepsilon_r(\kappa_A) + \psi(\kappa_A)} & \varepsilon_r(\kappa_A) > \varepsilon_f(\kappa_A), \\ \lambda_f \equiv \frac{\phi_{\max}}{\varphi/\varepsilon_f(\kappa_A) + \psi(\kappa_A)} & \varepsilon_r(\kappa_A) < \varepsilon_f(\kappa_A). \end{cases} \quad (S36)$$

So, in aerobic conditions, why do microbes use the wasteful fermentation pathway when the growth rate is large? An intuitive guess is that the fermentation pathway is more efficient in terms of proteome energy efficiency, i.e.,  $\varepsilon_f > \varepsilon_r$ . If so, then why do microbes still use the normal respiration pathway when the growth is small? The answer lies in that both  $\varepsilon_r(\kappa_A)$  and  $\varepsilon_f(\kappa_A)$  are not constants, yet rather nutrient dependent. In Eq. S31, when  $\kappa_A$  is small, just consider the extreme case of  $\kappa_A \rightarrow 0$ , and then

$$\begin{cases} \varepsilon_r(\kappa_A \rightarrow 0) \approx [\beta_1 + 2(\beta_2 + \beta_3 + \beta_4)] \cdot \kappa_A, \\ \varepsilon_f(\kappa_A \rightarrow 0) \approx [\beta_1 + 2(\beta_2 + \beta_6)] \cdot \kappa_A. \end{cases} \quad (S37)$$

Since  $\beta_3 + \beta_4 \gg \beta_6$ , clearly,

$$\varepsilon_r(\kappa_A \rightarrow 0) > \varepsilon_f(\kappa_A \rightarrow 0). \quad (S38)$$

Combined with Eq. S36, thus cells would certainly use the respiration pathway when the growth rate is very small. Meanwhile, suppose that  $\kappa_A^{\max}$  is the maximum value of  $\kappa_A$  across different Group A carbon sources with saturated concentration, as long as

$$\frac{\beta_3 + \beta_4 - \beta_6}{2\kappa_A^{\max}} < \left( \frac{\beta_1}{2} + \beta_2 + \beta_6 \right) \left( \frac{1}{2\kappa_1} + \frac{1}{\kappa_2} + \frac{1}{\kappa_3} + \frac{1}{\kappa_4} \right) - \left( \frac{\beta_1}{2} + \beta_2 + \beta_3 + \beta_4 \right) \left( \frac{1}{2\kappa_1} + \frac{1}{\kappa_2} + \frac{1}{\kappa_6} \right), \quad (S39)$$

then,

$$\varepsilon_r(\kappa_A^{\max}) < \varepsilon_f(\kappa_A^{\max}), \quad (S40)$$

and cells would use the fermentation pathway when the growth rate is large. In practice, experimental studies<sup>10</sup> reported that the proteome energy efficiency of *E. coli* is higher in fermentation than that of respiration when the carbon source is lactose and with saturated concentration<sup>11</sup>, i.e.,  $\varepsilon_r(\kappa_{\text{lactose}}^{\text{(ST)}}) < \varepsilon_f(\kappa_{\text{lactose}}^{\text{(ST)}})$ , where  $\kappa_{\text{lactose}}$  represents the lactose substrate quality and the superscript “(ST)” denotes for saturation. In fact, *E. coli* actually grows much faster in G6p than lactose<sup>10</sup>, obviously,  $\kappa_A^{\text{max}} > \kappa_{\text{lactose}}^{\text{(ST)}}$ . The above example verifies that Eq. S40 holds for *E. coli*. In fact, more recent studies<sup>12</sup> supported that Eq. S40 holds generically for many microbial species. From the theoretical side, we can verify Eq. S39 and thus Eq. S40 using Eq. S20 combined with the in vivo/ in vitro biochemical parameters obtained from experimental data (see Tables S1-S2). For example, it is easy to check that  $\varepsilon_r(\kappa_{\text{glucose}}^{\text{(ST)}}) < \varepsilon_f(\kappa_{\text{glucose}}^{\text{(ST)}})$  with this method (see Sec.8.2), which confirms the validity of Eq. S40.

Now that both Eqs. S38 and S40 hold, then the function  $\Delta(\kappa_A) \equiv \varepsilon_f(\kappa_A)/\varepsilon_r(\kappa_A)$  increases monotonously with  $\kappa_A$ . Thus, this exists a critical value of  $\kappa_A^{\text{(C)}}$ , which denoted as  $\kappa_A^{\text{(C)}}$ , with

$$\begin{cases} \varepsilon_f(\kappa_A) > \varepsilon_r(\kappa_A), & \kappa_A > \kappa_A^{\text{(C)}}; \\ \varepsilon_f(\kappa_A) = \varepsilon_r(\kappa_A), & \kappa_A = \kappa_A^{\text{(C)}}; \\ \varepsilon_f(\kappa_A) < \varepsilon_r(\kappa_A), & \kappa_A < \kappa_A^{\text{(C)}}. \end{cases} \quad (\text{S41})$$

Combined with Eq. S31, we have

$$\kappa_A^{\text{(C)}} = \frac{\beta_3 + \beta_4 - \beta_6}{(\beta_1/2 + \beta_2 + \beta_6)(1/\kappa_1 + 2/\kappa_2 + 2/\kappa_3 + 2/\kappa_4) - (\beta_1/2 + \beta_2 + \beta_3 + \beta_4)(1/\kappa_1 + 2/\kappa_2 + 2/\kappa_6)}. \quad (\text{S42})$$

By substituting Eq. S42 into Eqs. S31, S32, S36, we obtain the values of  $\varepsilon_r(\kappa_A^{\text{(C)}})$ ,  $\varepsilon_f(\kappa_A^{\text{(C)}})$ , and the growth rate at the transition point,  $\lambda_{\text{C}}$ :

$$\begin{cases} \varepsilon_r(\kappa_A^{\text{(C)}}) = \varepsilon_f(\kappa_A^{\text{(C)}}) = \frac{\beta_3 + \beta_4 - \beta_6}{1/\kappa_3 + 1/\kappa_4 - 1/\kappa_6}, \\ \lambda_{\text{C}} \equiv \lambda(\kappa_A^{\text{(C)}}) = \frac{\phi_{\text{max}}}{\phi/\varepsilon_{r/f}(\kappa_A^{\text{(C)}}) + \psi(\kappa_A^{\text{(C)}})}, \end{cases} \quad (\text{S43})$$

where  $\varepsilon_{r/f}$  represents for either  $\varepsilon_r$  or  $\varepsilon_f$ . In Fig. 1e, we show the dependencies of  $\varepsilon_r(\kappa_A)$ ,  $\varepsilon_f(\kappa_A)$  and  $\lambda(\kappa_A)$  on  $\kappa_A$  in a 3-dimensional form as  $\kappa_A$  changes.

## S2.3 The relations between overflow fluxes and growth rate

We proceed to study the relations between the respiration/fermentation fluxes and the cell growth rate.

From Eqs. S16 and S30, we see that the stoichiometric fluxes  $J_r, J_f$ , the normalized fluxes  $J_r^{(N)}, J_f^{(N)}$  and the normalized energy fluxes  $J_r^{(E)}, J_f^{(E)}$  are interconvertible. For convenience, we first analyze the relations between  $J_r^{(E)}, J_f^{(E)}$  and  $\lambda$  with growth rate optimization. In fact, all these terms are merely functions of  $\kappa_A$  (see Eqs. S34-S36), which is determined by the nutrient condition (Eq. S27).

In the ideal homogenous case, i.e., all microbes share identical biochemical parameters, as  $\lambda(\kappa_A)$  increases with  $\kappa_A$ ,  $J_f^{(E)}$  show up abruptly and  $J_r^{(E)}$  vanish simultaneously as  $\kappa_A$  right exceeds  $\kappa_A^{(C)}$  (Fig. 1e, see also Eqs. S34-S35, S41). Combining Eqs. S34-S36 and S43, we have

$$\begin{cases} J_f^{(E)} = \varphi \cdot \lambda \cdot \theta(\lambda - \lambda_C), \\ J_r^{(E)} = \varphi \cdot \lambda \cdot [1 - \theta(\lambda - \lambda_C)], \end{cases} \quad (S44)$$

where “ $\theta$ ” stands for the Heaviside step function. Defining  $\lambda_{\max} = \lambda(\kappa_A^{\max})$ , and then,  $[0, \lambda_{\max}]$  is the relevant range of the x axis. In fact, the digital responses in Eq. S44 are consistent with the numerical simulation results in Molenaar *et al.*<sup>11</sup>. However, these results are incompatible with the threshold-analog response in the standard picture of overflow metabolism<sup>10,13</sup>.

In practice, the values of  $k_i^{\text{cat}}$  can be greatly influenced by the concentrations of potassium and phosphate<sup>14</sup>, which vary from cell to cell. Then, there is a distribution of the values for  $k_i^{\text{cat}}$  among the cell populations, commonly we call it extrinsic noise<sup>15</sup>. For convenience, we assume that each  $k_i^{\text{cat}}$  (and thus  $\kappa_i$ ) follows a Gaussian distribution with the coefficient of variance (CV) taken as 25%. Then, the distribution of  $\lambda_C$  can be approximated by a Gaussian distribution (see Sec. 7.1):

$$\lambda_C \sim \mathcal{N}(\mu_{\lambda_C}, \sigma_{\lambda_C}^2), \quad (S45)$$

where  $\mu_{\lambda_C}$  and  $\sigma_{\lambda_C}$  stand for the mean and standard deviation of  $\lambda_C$ , with the CV  $\sigma_{\lambda_C}/\mu_{\lambda_C}$  calculated to be 12% (see Sec. 8.2 for details). Note that  $\lambda$  is  $\kappa_A$  dependent, while  $\lambda_C$  is independent of  $\kappa_A$ . Thus, given the growth rate of microbes in a culturing medium (e.g., in a chemostat), the normalized energy fluxes are:

$$\begin{cases} J_f^{(E)}(\lambda) = \frac{1}{2} \varphi \cdot \lambda \cdot \left[ \operatorname{erf}\left(\frac{\lambda - \mu_{\lambda_c}}{\sqrt{2}\sigma_{\lambda_c}}\right) + 1 \right], \\ J_r^{(E)}(\lambda) = \frac{1}{2} \varphi \cdot \lambda \cdot \left[ 1 - \operatorname{erf}\left(\frac{\lambda - \mu_{\lambda_c}}{\sqrt{2}\sigma_{\lambda_c}}\right) \right], \end{cases} \quad (S46)$$

where ‘erf’ represents the error function. In practice, given a culturing medium, there is also a probability distribution for the growth rate (Fig. S3b, see also Eq. S157). For approximation, in plotting the flux-growth rate relations, we use the deterministic (noise free) value of the growth rate as the proxy. To compare with experiments, basically, we are comparing the normalized fluxes  $J_r^{(N)}$ ,  $J_f^{(N)}$  (see Sec. 8.1 for details). Combining Eqs. S30 and S46, we get

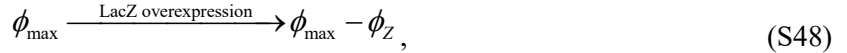
$$\begin{cases} J_f^{(N)}(\lambda) = \frac{\varphi}{\beta_1 + 2(\beta_2 + \beta_6)} \cdot \lambda \cdot \left[ \operatorname{erf}\left(\frac{\lambda - \mu_{\lambda_c}}{\sqrt{2}\sigma_{\lambda_c}}\right) + 1 \right], \\ J_r^{(N)}(\lambda) = \frac{\varphi}{\beta_1 + 2(\beta_2 + \beta_3 + \beta_4)} \cdot \lambda \cdot \left[ 1 - \operatorname{erf}\left(\frac{\lambda - \mu_{\lambda_c}}{\sqrt{2}\sigma_{\lambda_c}}\right) \right]. \end{cases} \quad (S47)$$

In Fig. 1c-d, we see that Eq. S47 quantitatively illustrates the experimental data<sup>10</sup>, where the model parameters were obtained using the biochemical data for the catalytic enzymes (see Table S1 for details).

### S3 Model perturbations

#### S3.1 Overexpression of useless proteins

Here we consider the case that overexpression of the protein encoded by LacZ gene in *E. coli*. Effectively, this limits the proteome by alternating  $\phi_{\max}$ :



where  $\phi_Z$  stands for the fraction of useless proteins, which is controllable in experiments. Then, the growth rate changes into a bivariate function of  $\kappa_A$  and  $\phi_Z$ :

$$\lambda(\kappa_A, \phi_Z) = \begin{cases} \frac{\phi_{\max} - \phi_Z}{\varphi/\varepsilon_r(\kappa_A) + \psi(\kappa_A)} & \varepsilon_r(\kappa_A) > \varepsilon_f(\kappa_A), \\ \frac{\phi_{\max} - \phi_Z}{\varphi/\varepsilon_f(\kappa_A) + \psi(\kappa_A)} & \varepsilon_r(\kappa_A) < \varepsilon_f(\kappa_A), \end{cases} \quad (S49)$$

and thus,

$$\lambda(\kappa_A, \phi_Z) = \lambda(\kappa_A, 0)(1 - \phi_Z/\phi_{\max}). \quad (S50)$$

Obviously,  $\kappa_A^{(C)}$  is still a constant (following Eq. S42), while  $\lambda_C(\phi_Z) \equiv \lambda(\kappa_A^{(C)}, \phi_Z)$  and  $\lambda_{\max}(\phi_Z) \equiv \lambda(\kappa_A^{\max}, \phi_Z)$  turns into functions of  $\phi_Z$ :

$$\begin{cases} \lambda_C(\phi_Z) = \lambda_C(0)(1 - \phi_Z/\phi_{\max}), \\ \lambda_{\max}(\phi_Z) = \lambda_{\max}(0)(1 - \phi_Z/\phi_{\max}). \end{cases} \quad (S51)$$

In the homogenous case,  $J_f^{(E)}$  and  $J_r^{(E)}$  follow

$$\begin{cases} J_f^{(E)}(\kappa_A, \phi_Z) = \varphi \cdot \lambda(\kappa_A, \phi_Z) \cdot \theta(\lambda(\kappa_A, \phi_Z) - \lambda_C(\phi_Z)), \\ J_r^{(E)}(\kappa_A, \phi_Z) = \varphi \cdot \lambda(\kappa_A, \phi_Z) \cdot [1 - \theta(\lambda(\kappa_A, \phi_Z) - \lambda_C(\phi_Z))]. \end{cases} \quad (S52)$$

Combined with Eqs. S50-S51, we have

$$\begin{cases} J_f^{(E)}(\kappa_A, \phi_Z) = \varphi \cdot \lambda(\kappa_A, \phi_Z) \cdot \theta(\lambda(\kappa_A, 0) - \lambda_C(0)), \\ J_r^{(E)}(\kappa_A, \phi_Z) = \varphi \cdot \lambda(\kappa_A, \phi_Z) \cdot [1 - \theta(\lambda(\kappa_A, 0) - \lambda_C(0))]. \end{cases} \quad (S53)$$

To compare with experiments, we still assume that each  $k_i^{\text{cat}}$  and thus  $\kappa_i$  follow a Gaussian distribution with a CV of 25%, and neglect the noise on  $\phi_Z$  and  $\phi_{\max}$ . Combining Eqs. S45 and S51, we see that  $\lambda_C(\phi_Z)$  roughly follows a Gaussian distribution:

$$\lambda_C(\phi_Z) \sim \mathcal{N}(\mu_{\lambda_C}(\phi_Z), \sigma_{\lambda_C}(\phi_Z)^2), \quad (S54)$$

where  $\mu_{\lambda_C}(\phi_Z)$  and  $\sigma_{\lambda_C}(\phi_Z)$  represent the mean and standard deviation of  $\lambda_C(\phi_Z)$ , with

$$\begin{cases} \mu_{\lambda_C}(\phi_Z) = \mu_{\lambda_C}(0)(1 - \phi_Z/\phi_{\max}), \\ \sigma_{\lambda_C}(\phi_Z) = \sigma_{\lambda_C}(0)(1 - \phi_Z/\phi_{\max}). \end{cases} \quad (S55)$$

Here,  $\mu_{\lambda_C}(0)$ ,  $\sigma_{\lambda_C}(0)$ ,  $\lambda_C(0)$ ,  $\lambda_{\max}(0)$  and  $\lambda(\kappa_A, 0)$  represent the parameters or variables free from Lacz perturbations, just as those in Sec. 2.3. From Eq. S55, we see that the CV of  $\lambda_C(\phi_Z)$  (i.e.,  $\sigma_{\lambda_C}(\phi_Z)/\mu_{\lambda_C}(\phi_Z)$ ) is not influenced by  $\phi_Z$ . By combining Eqs. S46 and S48, we obtain the relations between the normalized energy fluxes and growth rate:

$$\begin{cases} J_f^{(E)}(\lambda(\kappa_A, \phi_z), \phi_z) = \frac{1}{2} \varphi \cdot \lambda(\kappa_A, \phi_z) \cdot \left[ \operatorname{erf} \left( \frac{\lambda(\kappa_A, \phi_z) - \mu_{\lambda_c}(\phi_z)}{\sqrt{2} \sigma_{\lambda_c}(\phi_z)} \right) + 1 \right], \\ J_r^{(E)}(\lambda(\kappa_A, \phi_z), \phi_z) = \frac{1}{2} \varphi \cdot \lambda(\kappa_A, \phi_z) \cdot \left[ 1 - \operatorname{erf} \left( \frac{\lambda(\kappa_A, \phi_z) - \mu_{\lambda_c}(\phi_z)}{\sqrt{2} \sigma_{\lambda_c}(\phi_z)} \right) \right], \end{cases} \quad (S56)$$

where  $\lambda(\kappa_A, \phi_z)$ ,  $\mu_{\lambda_c}(\phi_z)$  and  $\sigma_{\lambda_c}(\phi_z)$  follow Eqs. S50 and S55 accordingly. For a given value of  $\phi_z$ , i.e.,  $\phi_z$  is fixed, then,  $\lambda(\kappa_A, \phi_z)$  changes monotonously with  $\kappa_A$ . Combining Eqs. S55-S56 and S30, we have the relation between the normalized fluxes  $J_r^{(N)}$ ,  $J_f^{(N)}$  and growth rate (here  $\phi_z$  is a parameter):

$$\begin{cases} J_f^{(N)}(\lambda, \phi_z) = \frac{\varphi}{\beta_1 + 2(\beta_2 + \beta_6)} \cdot \lambda \cdot \left[ \operatorname{erf} \left( \frac{\lambda - \mu_{\lambda_c}(0)(1 - \phi_z/\phi_{\max})}{\sqrt{2} \sigma_{\lambda_c}(0)(1 - \phi_z/\phi_{\max})} \right) + 1 \right], \\ J_r^{(N)}(\lambda, \phi_z) = \frac{\varphi}{\beta_1 + 2(\beta_2 + \beta_3 + \beta_4)} \cdot \lambda \cdot \left[ 1 - \operatorname{erf} \left( \frac{\lambda - \mu_{\lambda_c}(0)(1 - \phi_z/\phi_{\max})}{\sqrt{2} \sigma_{\lambda_c}(0)(1 - \phi_z/\phi_{\max})} \right) \right]. \end{cases} \quad (S57)$$

In Fig. 2c. we show that the model predictions (Eq. S57) quantitatively agree with the experiments<sup>10</sup>.

Meanwhile, we can also perturb the growth rate by tuning  $\phi_z$  in a stable culturing environment, basically, with fixed concentration of a selected Group A carbon source (i.e., given  $[A]$ ). In fact, in this case, there exists a distribution of values for the  $\kappa_A$ , mainly due to the extrinsic noise on  $k_A^{\text{cat}}$ . Yet, this distribution is fixed, so, for convenience of description, we still call it fixed  $\kappa_A$ . Then, combining Eqs. S30, S50, S55 and S56, we get

$$\begin{cases} J_f^{(N)}(\lambda, \phi_z) = \frac{\varphi}{\beta_1 + 2(\beta_2 + \beta_6)} \cdot \left[ \operatorname{erf} \left( \frac{\lambda(\kappa_A, 0) - \mu_{\lambda_c}(0)}{\sqrt{2} \sigma_{\lambda_c}(0)} \right) + 1 \right] \cdot \lambda, \\ J_r^{(N)}(\lambda, \phi_z) = \frac{\varphi}{\beta_1 + 2(\beta_2 + \beta_3 + \beta_4)} \cdot \left[ 1 - \operatorname{erf} \left( \frac{\lambda(\kappa_A, 0) - \mu_{\lambda_c}(0)}{\sqrt{2} \sigma_{\lambda_c}(0)} \right) \right] \cdot \lambda. \end{cases} \quad (S58)$$

Here,  $\lambda(\kappa_A, 0)$  remains unaltered as  $\kappa_A$  is fixed. Thus, in this case,  $J_f^{(N)}$  and  $J_r^{(N)}$  (combined with Eq. S30) are proportional to  $\lambda$ , where the slopes are functions of  $\kappa_A$ . Specifically, the slope of  $J_f^{(N)}$  is a monotonically increasing function of  $\kappa_A$ , while that of  $J_r^{(N)}$  is a monotonically decreasing function of  $\kappa_A$ . In Fig. 2b, we see that the model predictions (Eq. S58) quantitatively agree with the experiments<sup>10</sup>.

In fact, the growth rate can be altered by tuning  $\phi_z$  and  $K_A$  simultaneously. Then, the relations among the energy fluxes, growth rate and  $\phi_z$  still follow Eq. S57 (here  $\phi_z$  is a variable). In a 3-D representation, these relations correspond to a surface. In Fig. 2a, we show that the model predictions (Eq. S57) match well with the experimental data<sup>10</sup>.

### S3.2 Energy dissipation

In practice, energy dissipation breaks the proportional relationship between the energy demand and biomass production. Thus, Eq. S25 changes into:

$$J_E = r_E \cdot J_{BM} + w \cdot \frac{M_{carbon}}{m_0}, \quad (S59)$$

where  $w$  represents the dissipation coefficient. In fact, the maintenance energy contributes to energy dissipation, and we define the maintenance energy coefficient as  $w_0$ . In bacteria, the impact of  $w_0$  is often negligible, particularly for all the above analysis. While in tumor cell,  $w_0$  plays a much more significant role. The introduction of energy dissipation triggers further modification on Eq. S26, combining Eq. S59 with Eq. S16, we have

$$J_E^{(N)} = \eta_E \cdot \lambda + w. \quad (S60)$$

Then, Eq. S29 changes into

$$\begin{cases} J_r^{(E)} + J_f^{(E)} = \varphi \cdot \lambda + w, \\ \frac{J_r^{(E)}}{\varepsilon_r} + \frac{J_f^{(E)}}{\varepsilon_f} = \phi_{max} - \psi \cdot \lambda. \end{cases} \quad (S61)$$

Consequently, if  $\varepsilon_r > \varepsilon_f$ , the best strategy of a microbe is

$$\begin{cases} J_f^{(E)} = 0, \\ J_r^{(E)} = \varphi \cdot \lambda + w, \end{cases} \quad \varepsilon_r > \varepsilon_f, \quad (S62)$$

and if  $\varepsilon_f > \varepsilon_r$ , the best strategy is

$$\begin{cases} J_f^{(E)} = \varphi \cdot \lambda + w, \\ J_r^{(E)} = 0. \end{cases} \quad \varepsilon_r < \varepsilon_f. \quad (S63)$$

Then, the growth rate turns into a bivariate function of both  $K_A$  and  $w$ :

$$\lambda(\kappa_A, w) = \begin{cases} \frac{\phi_{\max} - w/\varepsilon_r(\kappa_A)}{\varphi/\varepsilon_r(\kappa_A) + \psi(\kappa_A)} & \varepsilon_r(\kappa_A) > \varepsilon_f(\kappa_A), \\ \frac{\phi_{\max} - w/\varepsilon_f(\kappa_A)}{\varphi/\varepsilon_f(\kappa_A) + \psi(\kappa_A)} & \varepsilon_r(\kappa_A) < \varepsilon_f(\kappa_A). \end{cases} \quad (S64)$$

Obviously,  $\kappa_A^{(C)}$  remains a constant, while  $\lambda_C(w) \equiv \lambda(\kappa_A^{(C)}, w)$  and  $\lambda_{\max}(w) \equiv \lambda(\kappa_A^{\max}, w)$  changes into functions of  $w$ :

$$\begin{cases} \lambda_C(w) = \lambda_C(0) \left\{ 1 - w \left[ \varepsilon_{r/f}(\kappa_A^{(C)}) \phi_{\max} \right] \right\}, \\ \lambda_{\max}(w) = \lambda_{\max}(0) \left\{ 1 - w \left[ \varepsilon_f(\kappa_A^{\max}) \phi_{\max} \right] \right\}. \end{cases} \quad (S65)$$

For a cell population, in the homogenous case,  $J_f^{(E)}$  and  $J_r^{(E)}$  follow

$$\begin{cases} J_f^{(E)}(\kappa_A, w) = [\varphi \cdot \lambda(\kappa_A, w) + w] \cdot \theta(\lambda(\kappa_A, w) - \lambda_C(w)), \\ J_r^{(E)}(\kappa_A, w) = [\varphi \cdot \lambda(\kappa_A, w) + w] \cdot [1 - \theta(\lambda(\kappa_A, w) - \lambda_C(w))]. \end{cases} \quad (S66)$$

To compare with experiments, we still assume the same extent of extrinsic noise on  $k_i^{\text{cat}}$  (and thus  $\kappa_i$ ) as that specified in Sec. 2.3. Combining Eqs. S45 and S65, then,  $\lambda_C(w)$  approximately follows a Gaussian distribution:

$$\lambda_C(w) \sim \mathcal{N}(\mu_{\lambda_C}(w), \sigma_{\lambda_C}(w)^2), \quad (S67)$$

where  $\mu_{\lambda_C}(w)$  and  $\sigma_{\lambda_C}(w)$  represent the mean and standard deviation of  $\lambda_C(w)$ , and

$$\begin{cases} \mu_{\lambda_C}(w) = \mu_{\lambda_C}(0) \left\{ 1 - w \left[ \varepsilon_{r/f}(\kappa_A^{(C)}) \phi_{\max} \right] \right\}, \\ \sigma_{\lambda_C}(w) = \sigma_{\lambda_C}(0) \left\{ 1 - w \left[ \varepsilon_{r/f}(\kappa_A^{(C)}) \phi_{\max} \right] \right\}. \end{cases} \quad (S68)$$

Here,  $\mu_{\lambda_C}(0)$ ,  $\sigma_{\lambda_C}(0)$ ,  $\lambda_C(0)$ ,  $\lambda_{\max}(0)$  and  $\lambda(\kappa_A, 0)$  represent the parameters or variables free from energy dissipation. In fact, there is a distribution of values for  $\varepsilon_{r/f}(\kappa_A^{(C)})$ . For approximation, we use the deterministic value of  $\varepsilon_{r/f}(\kappa_A^{(C)})$  in Eq. S68, and then the CV of  $\lambda_C(w)$  is roughly unperturbed by  $w$ . Combining Eqs. S46, S66 and S67, we have

$$\begin{cases} J_f^{(E)}(\lambda(\kappa_A, w), w) = \frac{1}{2}(\varphi \cdot \lambda(\kappa_A, w) + w) \cdot \left[ \operatorname{erf}\left(\frac{\lambda(\kappa_A, w) - \mu_{\lambda_c}(w)}{\sqrt{2}\sigma_{\lambda_c}(w)}\right) + 1 \right], \\ J_r^{(E)}(\lambda(\kappa_A, w), w) = \frac{1}{2}(\varphi \cdot \lambda(\kappa_A, w) + w) \cdot \left[ 1 - \operatorname{erf}\left(\frac{\lambda(\kappa_A, w) - \mu_{\lambda_c}(w)}{\sqrt{2}\sigma_{\lambda_c}(w)}\right) \right]. \end{cases} \quad (S69)$$

Since the dissipation coefficient  $w$  is tunable in experiments, for a given value of  $w$ ,  $\lambda(\kappa_A, w)$  changes monotonously with  $\kappa_A$ . Combining Eqs. S68-S69 and S30, we have (here  $w$  is a parameter)

$$\begin{cases} J_f^{(N)}(\lambda, w) = \frac{\varphi \cdot \lambda + w}{\beta_1 + 2(\beta_2 + \beta_6)} \cdot \left[ \operatorname{erf}\left(\frac{\lambda - \mu_{\lambda_c}(0) \left\{ 1 - w / \left[ \varepsilon_{r/f}(\kappa_A^{(C)}) \phi_{\max} \right] \right\}}{\sqrt{2}\sigma_{\lambda_c}(0) \left\{ 1 - w / \left[ \varepsilon_{r/f}(\kappa_A^{(C)}) \phi_{\max} \right] \right\}}\right) + 1 \right], \\ J_r^{(N)}(\lambda, w) = \frac{\varphi \cdot \lambda + w}{\beta_1 + 2(\beta_2 + \beta_3 + \beta_4)} \cdot \left[ 1 - \operatorname{erf}\left(\frac{\lambda - \mu_{\lambda_c}(0) \left\{ 1 - w / \left[ \varepsilon_{r/f}(\kappa_A^{(C)}) \phi_{\max} \right] \right\}}{\sqrt{2}\sigma_{\lambda_c}(0) \left\{ 1 - w / \left[ \varepsilon_{r/f}(\kappa_A^{(C)}) \phi_{\max} \right] \right\}}\right) \right]. \end{cases} \quad (S70)$$

The comparison between model predictions (Eq. S70) and experimental results<sup>10</sup> is shown in Fig.3b, which agrees quantitatively. Meanwhile, the growth rate can also be perturbed by changing  $\kappa_A$  and  $w$  simultaneously. Then, the relations among the energy fluxes, growth rate and  $w$  follow Eq. S70 (here  $w$  is a variable). In a 3D representation, these relations correspond to a surface. As shown in Fig. 3a, the model predictions (Eq. S70) agree quantitatively with the experimental results<sup>10</sup>.

### S3.3 Translation inhibition

In *E. coli*, the translation rate can be modified by adding different concentrations of translation inhibitor, e.g., chloramphenicol (Cm). Then, the net effect of this perturbation is that:

$$\kappa_t \xrightarrow{\text{Translation inhibition}} \kappa_t / (1 + \iota), \quad (S71)$$

where  $\iota$  stands for the inhibition coefficient with  $\iota > 0$ , and  $(1 + \iota)^{-1}$  represents the translation efficiency. Thus, Eq. S32 changes into

$$\psi(\kappa_A, \iota) = \frac{\iota + 1}{\kappa_t} + \frac{1 + \eta_{a1} + \eta_c}{2\kappa_A} + \frac{\eta_{a2} + \eta_b + 2\eta_c + \eta_d}{2\kappa_1} + \frac{\eta_b + \eta_c}{\kappa_2} + \frac{\eta_c}{\kappa_3} + \frac{\eta_c + \eta_d}{\kappa_5} + \sum_i^{a1, a2, b, c, d} \frac{\eta_i}{\kappa_i}. \quad (S72)$$

First, we consider the case neglecting the maintenance energy, i.e.,  $w_0 = 0$ . Then, the growth rate takes the following form:

$$\lambda(\kappa_A, \iota) = \begin{cases} \frac{\phi_{\max}}{\varphi/\varepsilon_r(\kappa_A) + \psi(\kappa_A, \iota)} & \varepsilon_r(\kappa_A) > \varepsilon_f(\kappa_A), \\ \frac{\phi_{\max}}{\varphi/\varepsilon_f(\kappa_A) + \psi(\kappa_A, \iota)} & \varepsilon_r(\kappa_A) < \varepsilon_f(\kappa_A), \end{cases} \quad (S73)$$

where  $\lambda(\kappa_A, 0)$  and  $\psi(\kappa_A, 0)$  represent the terms free from translation inhibition. Thus,  $\lambda_C(\iota) \equiv \lambda(\kappa_A^{(C)}, \iota)$  and  $\lambda_{\max}(\iota) \equiv \lambda(\kappa_A^{\max}, \iota)$  changes into functions of  $\iota$ :

$$\begin{cases} \lambda_C(\iota) = \lambda_C(0) \frac{\varphi/\varepsilon_{r/f}(\kappa_A^{(C)}) + \psi(\kappa_A^{(C)}, 0)}{\varphi/\varepsilon_{r/f}(\kappa_A^{(C)}) + \psi(\kappa_A^{(C)}, \iota)}, \\ \lambda_{\max}(\iota) = \lambda_{\max}(0) \frac{\varphi/\varepsilon_f(\kappa_A^{\max}) + \psi(\kappa_A^{\max}, 0)}{\varphi/\varepsilon_f(\kappa_A^{\max}) + \psi(\kappa_A^{\max}, \iota)}. \end{cases} \quad (S74)$$

In the homogenous case,  $J_f^{(E)}$  and  $J_r^{(E)}$  follow

$$\begin{cases} J_f^{(E)}(\kappa_A, \iota) = \varphi \cdot \lambda(\kappa_A, \iota) \cdot \theta(\lambda(\kappa_A, \iota) - \lambda_C(\iota)), \\ J_r^{(E)}(\kappa_A, \iota) = \varphi \cdot \lambda(\kappa_A, \iota) \cdot [1 - \theta(\lambda(\kappa_A, \iota) - \lambda_C(\iota))]. \end{cases} \quad (S75)$$

To compare with experiments, we assume that there exists extrinsic noise as specified in Sec. 2.3. Combining Eqs. S45 and S74,  $\lambda_C(\iota)$  can be approximated by a Gaussian distribution:

$$\lambda_C(\iota) \sim \mathcal{N}(\mu_{\lambda_C}(\iota), \sigma_{\lambda_C}(\iota)^2), \quad (S76)$$

where  $\mu_{\lambda_C}(\iota)$  and  $\sigma_{\lambda_C}(\iota)$  represent the mean and standard deviation of  $\lambda_C(\iota)$ , with

$$\begin{cases} \mu_{\lambda_C}(\iota) = \mu_{\lambda_C}(0) \frac{\varphi/\varepsilon_{r/f}(\kappa_A^{(C)}) + \psi(\kappa_A^{(C)}, 0)}{\varphi/\varepsilon_{r/f}(\kappa_A^{(C)}) + \psi(\kappa_A^{(C)}, \iota)}, \\ \sigma_{\lambda_C}(\iota) = \sigma_{\lambda_C}(0) \frac{\varphi/\varepsilon_{r/f}(\kappa_A^{(C)}) + \psi(\kappa_A^{(C)}, 0)}{\varphi/\varepsilon_{r/f}(\kappa_A^{(C)}) + \psi(\kappa_A^{(C)}, \iota)}. \end{cases} \quad (S77)$$

Here,  $\mu_{\lambda_C}(0)$ ,  $\sigma_{\lambda_C}(0)$ ,  $\psi(\kappa_A^{(C)}, 0)$ ,  $\lambda_C(0)$  and  $\lambda_{\max}(0)$  stands for the terms free from translation inhibition. Basically, there are distributions of values for  $\varepsilon_{r/f}(\kappa_A^{(C)})$ ,  $\psi(\kappa_A^{(C)}, 0)$  and  $\psi(\kappa_A^{(C)}, \iota)$ . For

approximation, we use the deterministic values of these terms in Eq. S77, and then the CV of  $\lambda_c(\iota)$  can be approximated by  $\lambda_c(0)$ . Combining Eqs. S46, S75 and S76, we have

$$\begin{cases} J_f^{(E)}(\lambda(\kappa_A, \iota), \iota) = \frac{1}{2} \varphi \cdot \lambda(\kappa_A, \iota) \cdot \left[ \operatorname{erf}\left(\frac{\lambda(\kappa_A, \iota) - \mu_{\lambda_c}(\iota)}{\sqrt{2}\sigma_{\lambda_c}(\iota)}\right) + 1 \right], \\ J_r^{(E)}(\lambda(\kappa_A, \iota), \iota) = \frac{1}{2} \varphi \cdot \lambda(\kappa_A, \iota) \cdot \left[ 1 - \operatorname{erf}\left(\frac{\lambda(\kappa_A, \iota) - \mu_{\lambda_c}(\iota)}{\sqrt{2}\sigma_{\lambda_c}(\iota)}\right) \right]. \end{cases} \quad (S78)$$

In the experiments, the inhibition coefficient  $\iota$  is controllable by tuning the concentration of translation inhibitor. For a given value of  $\iota$ ,  $\lambda(\kappa_A, \iota)$  changes monotonously with  $\kappa_A$ . Combining Eqs. S30 and S78, we have ( $\iota$  is a parameter here)

$$\begin{cases} J_f^{(N)}(\lambda, \iota) = \frac{\varphi \cdot \lambda}{\beta_1 + 2(\beta_2 + \beta_6)} \cdot \left[ \operatorname{erf}\left(\frac{\lambda - \mu_{\lambda_c}(\iota)}{\sqrt{2}\sigma_{\lambda_c}(\iota)}\right) + 1 \right], \\ J_r^{(N)}(\lambda, \iota) = \frac{\varphi \cdot \lambda}{\beta_1 + 2(\beta_2 + \beta_3 + \beta_4)} \cdot \left[ 1 - \operatorname{erf}\left(\frac{\lambda - \mu_{\lambda_c}(\iota)}{\sqrt{2}\sigma_{\lambda_c}(\iota)}\right) \right], \end{cases} \quad (S79)$$

where  $\mu_{\lambda_c}(\iota)$  and  $\sigma_{\lambda_c}(\iota)$  follow Eq. S77. The growth rate can also be perturbed by altering  $\kappa_A$  and  $\iota$  simultaneously. Then, the relations among the energy fluxes, growth rate and  $\iota$  still follow Eq. S79 (here  $\iota$  is a variable). The comparison between Eq. S79 and experimental data<sup>10</sup> is shown in Fig. S4a (3-D) and S4b (2-D). Overall, it shows good consistency, however, there is still a noticeable discrepancy when  $\iota$  is large (i.e., with high concentration of translation inhibitor). Then, it came to our mind the maintenance energy  $w_0$ , which is sure small, yet may account for this discrepancy. Then,  $\lambda(\kappa_A, \iota)$  changes into

$$\lambda(\kappa_A, \iota) = \begin{cases} \frac{\phi_{\max} - w_0 / \varepsilon_r(\kappa_A)}{\varphi / \varepsilon_r(\kappa_A) + \psi(\kappa_A, \iota)} & \varepsilon_r(\kappa_A) > \varepsilon_f(\kappa_A), \\ \frac{\phi_{\max} - w_0 / \varepsilon_f(\kappa_A)}{\varphi / \varepsilon_f(\kappa_A) + \psi(\kappa_A, \iota)} & \varepsilon_r(\kappa_A) < \varepsilon_f(\kappa_A), \end{cases} \quad (S80)$$

while  $\lambda_c(\iota) \equiv \lambda(\kappa_A^{(C)}, \iota)$  and  $\lambda_{\max}(\iota) \equiv \lambda(\kappa_A^{\max}, \iota)$  still follow Eq. S74, although the forms of  $\lambda_c(0)$  and  $\lambda_{\max}(0)$  change into

$$\begin{cases} \lambda_C(0) = \frac{\phi_{\max} - w_0 / \varepsilon_{r/f}(\kappa_A^{(C)})}{\varphi / \varepsilon_{r/f}(\kappa_A^{(C)}) + \psi(\kappa_A^{(C)}, 0)}, \\ \lambda_{\max}(0) = \frac{\phi_{\max} - w_0 / \varepsilon_f(\kappa_A^{\max})}{\varphi / \varepsilon_f(\kappa_A^{\max}) + \psi(\kappa_A^{\max}, 0)}. \end{cases} \quad (S81)$$

In the homogenous case,  $J_f^{(E)}$  and  $J_r^{(E)}$  follow

$$\begin{cases} J_f^{(E)}(\kappa_A, \iota) = [\varphi \cdot \lambda(\kappa_A, \iota) + w_0] \cdot \theta(\lambda(\kappa_A, \iota) - \lambda_C(\iota)), \\ J_r^{(E)}(\kappa_A, \iota) = [\varphi \cdot \lambda(\kappa_A, \iota) + w_0] \cdot [1 - \theta(\lambda(\kappa_A, \iota) - \lambda_C(\iota))]. \end{cases} \quad (S82)$$

To compare with experiments, we assume that the extrinsic noise follows that specified in Sec. 2.3. Combing Eqs. S45, S74 and S81, then,  $\lambda_C(\iota)$  roughly follows a Gaussian distribution:

$$\lambda_C(\iota) \sim \mathcal{N}(\mu_{\lambda_C}(\iota), \sigma_{\lambda_C}(\iota)^2). \quad (S83)$$

Here  $\mu_{\lambda_C}(\iota)$  and  $\sigma_{\lambda_C}(\iota)$  still follow Eq. S77, while  $\mu_{\lambda_C}(0)$  and  $\sigma_{\lambda_C}(0)$  change accordingly with Eq. S81. For approximation, we use the deterministic values of the relevant terms in Eq. S77, and then the CV of  $\lambda_C(\iota)$  is roughly the same as  $\lambda_C(0)$ . Combining Eqs. S46, S82 and S83, we have

$$\begin{cases} J_f^{(E)}(\lambda(\kappa_A, \iota), \iota) = \frac{1}{2}(\varphi \cdot \lambda(\kappa_A, \iota) + w_0) \cdot \left[ \operatorname{erf}\left(\frac{\lambda(\kappa_A, \iota) - \mu_{\lambda_C}(\iota)}{\sqrt{2}\sigma_{\lambda_C}(\iota)}\right) + 1 \right], \\ J_r^{(E)}(\lambda(\kappa_A, \iota), \iota) = \frac{1}{2}(\varphi \cdot \lambda(\kappa_A, \iota) + w_0) \cdot \left[ 1 - \operatorname{erf}\left(\frac{\lambda(\kappa_A, \iota) - \mu_{\lambda_C}(\iota)}{\sqrt{2}\sigma_{\lambda_C}(\iota)}\right) \right]. \end{cases} \quad (S84)$$

Thus, for a given  $\iota$ ,  $\lambda(\kappa_A, \iota)$  changes monotonously with  $\kappa_A$ . Combining Eqs. S30 and S84, we have (here  $\iota$  is a parameter)

$$\begin{cases} J_f^{(N)}(\lambda, \iota) = \frac{\varphi \cdot \lambda + w_0}{\beta_1 + 2(\beta_2 + \beta_6)} \cdot \left[ \operatorname{erf}\left(\frac{\lambda - \mu_{\lambda_C}(\iota)}{\sqrt{2}\sigma_{\lambda_C}(\iota)}\right) + 1 \right], \\ J_r^{(N)}(\lambda, \iota) = \frac{\varphi \cdot \lambda + w_0}{\beta_1 + 2(\beta_2 + \beta_3 + \beta_4)} \cdot \left[ 1 - \operatorname{erf}\left(\frac{\lambda - \mu_{\lambda_C}(\iota)}{\sqrt{2}\sigma_{\lambda_C}(\iota)}\right) \right]. \end{cases} \quad (S85)$$

The growth rate and fluxes can also be perturbed by altering  $K_A$  and  $\iota$  simultaneously. The relations among the energy fluxes, growth rate and  $\iota$  would still follow Eq. S85 other than that now  $\iota$  is regarded as a variable. Assuming that there is a tiny amount of maintenance energy. Basically, we assign  $w_0 = 2.5 (h^{-1})$ . Then, we see that the experimental results<sup>10</sup> agree quantitatively well with the model predictions (Fig.3c-d).

#### S4 Overflow metabolism in substrates other than Group A carbon sources

Due to the topology of metabolic network, Group A carbon sources follow the equation (Eq. S47) of overflow metabolism upon  $K_A$  perturbations (i.e., vary the type or concentration of a Group A carbon source). This has been demonstrated clearly in the above analysis, which agrees quantitatively with experiments. However, further analysis is required for substrates other than Group A sources, due to the topological differences in the carbon utilization<sup>4</sup>. Basically, substrates entering from glycolysis or the points before acetyl-CoA are potentially involved in overflow metabolism, while those join from the TCA cycle are not relevant to this behavior. Still, mixed carbon sources are potential to induce a different feature in the overflow metabolism so long as there is one carbon source coming from glycolysis.

##### S4.1 Pyruvate

The coarse-grained model for pyruvate utilization is shown in Fig. 3e. Here, nodes  $M_1, M_2, M_3, M_4, M_5$  follow everything depicted in Sec. 2.1. Each of the biochemical reactions follows Eq. S5 with  $b_i = 1$  except that  $2M_2 \rightarrow M_1$  and  $M_3 + M_5 \rightarrow M_4$ . By applying flux balance of the stoichiometric fluxes combining with Eq. S8, we have

$$\left\{ \begin{array}{l} \Phi_{py} \cdot \xi_{py} = \Phi_7 \cdot \xi_7 + \Phi_8 \cdot \xi_8, \\ \Phi_7 \cdot \xi_7 = 2\Phi_9 \cdot \xi_9 + \Phi_5 \cdot \xi_5 + \Phi_{a2} \cdot \xi_{a2}, \\ \Phi_9 \cdot \xi_9 = \Phi_{a1} \cdot \xi_{a1}, \\ \Phi_8 \cdot \xi_8 = \Phi_3 \cdot \xi_3 + \Phi_6 \cdot \xi_6 + \Phi_b \cdot \xi_b, \\ \Phi_5 \cdot \xi_5 + \Phi_4 \cdot \xi_4 = \Phi_3 \cdot \xi_3 + \Phi_d \cdot \xi_d, \\ \Phi_3 \cdot \xi_3 = \Phi_4 \cdot \xi_4 + \Phi_c \cdot \xi_c. \end{array} \right. \quad (S86)$$

For energy production, we convert all the energy currencies into ATPs, and then,

$$\beta_8 \cdot \Phi_8 \cdot \xi_8 + \beta_3 \cdot \Phi_3 \cdot \xi_3 + \beta_4 \cdot \Phi_4 \cdot \xi_4 + \beta_6 \cdot \Phi_6 \cdot \xi_6 + \beta_{a1} \cdot \Phi_{a1} \cdot \xi_{a1} - \beta_7 \cdot \Phi_7 \cdot \xi_7 - \beta_9 \cdot \Phi_9 \cdot \xi_9 = J_E. \quad (S87)$$

Here,  $\beta_7 = 1$ ,  $\beta_8 = 2$ ,  $\beta_3 = 2$ ,  $\beta_4 = 6$ ,  $\beta_6 = 1$ ,  $\beta_9 = 6$ ,  $\beta_{a1} = 4$ , and  $J_E$  follows Eq. S25. By applying the substitution specified in Eqs. S9, S12, S14-S18, combined with Eqs. S4, S10, S22, S23, S25, S86-S87 and the constraint of proteome resource allocation, we have

$$\begin{cases}
\phi_{\text{py}} \cdot \kappa_{\text{py}} = \phi_7 \cdot \kappa_7 + \phi_8 \cdot \kappa_8, \\
\phi_7 \cdot \kappa_7 = 2\phi_9 \cdot \kappa_9 + \phi_5 \cdot \kappa_5 + \phi_{a2} \cdot \kappa_{a2}, \\
\phi_9 \cdot \kappa_9 = \phi_{a1} \cdot \kappa_{a1} \\
\phi_8 \cdot \kappa_8 = \phi_3 \cdot \kappa_3 + \phi_6 \cdot \kappa_6 + \phi_b \cdot \kappa_b \\
\phi_3 \cdot \kappa_3 = \phi_4 \cdot \kappa_4 + \phi_c \cdot \kappa_c \\
\phi_5 \cdot \kappa_5 + \phi_4 \cdot \kappa_4 = \phi_3 \cdot \kappa_3 + \phi_d \cdot \kappa_d \\
\phi_{a1} \cdot \kappa_{a1} = \eta_{a1} \cdot \lambda, \phi_{a2} \cdot \kappa_{a2} = \eta_{a2} \cdot \lambda, \phi_b \cdot \kappa_b = \eta_b \cdot \lambda, \phi_c \cdot \kappa_c = \eta_c \cdot \lambda, \phi_d \cdot \kappa_d = \eta_d \cdot \lambda, \\
\beta_8 \cdot \phi_8 \cdot \kappa_8 + \beta_3 \cdot \phi_3 \cdot \kappa_3 + \beta_4 \cdot \phi_4 \cdot \kappa_4 + \beta_6 \cdot \phi_6 \cdot \kappa_6 + \beta_{a1} \cdot \phi_{a1} \cdot \kappa_{a1} - \beta_7 \cdot \phi_7 \cdot \kappa_7 - \beta_9 \cdot \phi_9 \cdot \kappa_9 = J_{\text{E}}^{(\text{N})}, \\
J_{\text{E}}^{(\text{N})} = \eta_{\text{E}} \cdot \lambda, \lambda = \phi_R \cdot \kappa_t, J_r^{(\text{N})} = \phi_4 \cdot \kappa_4, J_f^{(\text{N})} = \phi_6 \cdot \kappa_6, \\
\phi_{\text{R}} + \phi_{\text{py}} + \phi_3 + \phi_4 + \phi_5 + \phi_6 + \phi_7 + \phi_8 + \phi_9 + \phi_{a1} + \phi_{a2} + \phi_b + \phi_c + \phi_d = \phi_{\text{max}}, 
\end{cases} \quad (\text{S88})$$

where  $\eta_{\text{E}} = r_{\text{E}} \cdot \left[ \sum_i r_i / N_{\text{EP}_i}^{\text{carbon}} \right]^{-1}$ .  $\kappa_i$  is roughly a constant which follows Eq. S20 for each of the intermediate node. The substrate quality of  $\kappa_{\text{py}}$  varies with the external concentration of pyruvate ([py]),

$$\kappa_{\text{py}} \equiv \frac{r_{\text{protein}}}{r_{\text{carbon}}} \cdot \frac{k_{\text{py}}^{\text{cat}}}{m_{E_{\text{py}}}} \cdot \frac{[\text{py}]}{[\text{py}] + K_{\text{py}}} \cdot m_0 \quad (\text{S89})$$

From Eq. S88, all  $\phi_i$  can be expressed by  $J_r^{(\text{N})}$ ,  $J_f^{(\text{N})}$ , and  $\lambda$ :

$$\begin{cases}
\phi_{\text{py}} = \left[ (2\eta_{a1} + \eta_{a2} + \eta_b + 2\eta_c + \eta_d) \lambda + J_r^{(\text{N})} + J_f^{(\text{N})} \right] / \kappa_{\text{py}}, \\
\phi_7 = (2\eta_{a1} + \eta_{a2} + \eta_c + \eta_d) \lambda / \kappa_7, \phi_9 = \eta_{a1} \cdot \lambda / \kappa_9 \\
\phi_8 = \left[ J_r^{(\text{N})} + J_f^{(\text{N})} + (\eta_b + \eta_c) \lambda \right] / \kappa_8 \\
\phi_3 = (J_r^{(\text{N})} + \eta_c \cdot \lambda) / \kappa_3, \phi_4 = J_r^{(\text{N})} / \kappa_4, \\
\phi_5 = (\eta_c + \eta_d) \lambda / \kappa_5, \phi_6 = J_f^{(\text{N})} / \kappa_6, \\
\phi_i = \eta_i \cdot \lambda / \kappa_i \quad (i = a1, a2, b, c, d).
\end{cases} \quad (\text{S90})$$

By substituting Eq. S90 into Eq. S88, we have

$$\begin{cases}
J_r^{(\text{E,py})} + J_f^{(\text{E,py})} = \phi_{\text{py}} \cdot \lambda, \\
\frac{J_r^{(\text{E,py})}}{\mathcal{E}_r^{(\text{py})}} + \frac{J_f^{(\text{E,py})}}{\mathcal{E}_f^{(\text{py})}} = \phi_{\text{max}} - \psi_{\text{py}} \cdot \lambda.
\end{cases} \quad (\text{S91})$$

Here,  $J_r^{(\text{E,py})}$  and  $J_f^{(\text{E,py})}$  stand for the normalized energy fluxes of respiration and fermentation, with

$$\begin{cases} J_r^{(E,py)} = (\beta_3 + \beta_4 + \beta_8) \cdot J_r^{(N)}, \\ J_f^{(E,py)} = (\beta_6 + \beta_8) \cdot J_f^{(N)}. \end{cases} \quad (S92)$$

The coefficients  $\varepsilon_r^{(py)}$  and  $\varepsilon_f^{(py)}$  represent the proteome energy efficiencies of respiration and fermentation (Fig. S2a-b), with

$$\begin{cases} \varepsilon_r^{(py)} = \frac{\beta_3 + \beta_4 + \beta_8}{1/\kappa_{py} + 1/\kappa_8 + 1/\kappa_3 + 1/\kappa_4}, \\ \varepsilon_f^{(py)} = \frac{\beta_6 + \beta_8}{1/\kappa_{py} + 1/\kappa_8 + 1/\kappa_6}. \end{cases} \quad (S93)$$

$\psi_{py}^{-1}$  is the proteome efficiency of biomass pathway (Fig. S2c), with

$$\psi_{py} = \frac{1}{\kappa_t} + \frac{1 + \eta_{a1} + \eta_c}{\kappa_{py}} + \frac{1 - \eta_b + \eta_{a1}}{\kappa_7} + \frac{\eta_b + \eta_c}{\kappa_8} + \frac{\eta_{a1}}{\kappa_9} + \frac{\eta_c}{\kappa_3} + \frac{\eta_c + \eta_d}{\kappa_5} + \sum_i^{a1, a2, b, c, d} \frac{\eta_i}{\kappa_i}. \quad (S94)$$

$\varphi_{py}$  is the energy demand coefficient (a constant), with

$$\varphi_{py} \equiv \eta_E + \beta_7 \cdot (1 - \eta_b + \eta_{a1}) + \beta_9 \cdot \eta_{a1} - \beta_8 \cdot (\eta_c + \eta_b) - \beta_3 \cdot \eta_c - \beta_{a1} \cdot \eta_{a1}, \quad (S95)$$

Obviously, Eq. S91 is identical in form with Eq. S29. The growth rate changes into  $\kappa_{py}$  dependent

$$\lambda(\kappa_{py}) = \begin{cases} \frac{\phi_{max}}{\varphi_{py}/\varepsilon_r^{(py)}(\kappa_{py}) + \psi_{py}(\kappa_{py})} & \varepsilon_r^{(py)}(\kappa_{py}) > \varepsilon_f^{(py)}(\kappa_{py}), \\ \frac{\phi_{max}}{\varphi_{py}/\varepsilon_f^{(py)}(\kappa_{py}) + \psi_{py}(\kappa_{py})} & \varepsilon_r^{(py)}(\kappa_{py}) < \varepsilon_f^{(py)}(\kappa_{py}). \end{cases} \quad (S96)$$

When  $\kappa_{py}$  is very small, combined with Eq. S93, then

$$\begin{cases} \varepsilon_r^{(py)}(\kappa_{py} \rightarrow 0) \approx (\beta_3 + \beta_4 + \beta_8) \cdot \kappa_{py}, \\ \varepsilon_f^{(py)}(\kappa_{py} \rightarrow 0) \approx (\beta_6 + \beta_8) \cdot \kappa_{py}. \end{cases} \quad (S97)$$

Obviously,

$$\varepsilon_r^{(py)}(\kappa_{py} \rightarrow 0) > \varepsilon_f^{(py)}(\kappa_{py} \rightarrow 0). \quad (S98)$$

As long as

$$\frac{\beta_3 + \beta_4 - \beta_6}{\kappa_{\text{py}}^{(\text{ST})}} < (\beta_6 + \beta_8) \left( \frac{1}{\kappa_8} + \frac{1}{\kappa_3} + \frac{1}{\kappa_4} \right) - (\beta_3 + \beta_4 + \beta_8) \cdot \left( \frac{1}{\kappa_8} + \frac{1}{\kappa_6} \right), \quad (\text{S99})$$

where the superscript “(ST)” stands for the saturated concentration, then,

$$\varepsilon_r^{(\text{py})} \left( \kappa_{\text{py}}^{(\text{ST})} \right) < \varepsilon_f^{(\text{py})} \left( \kappa_{\text{py}}^{(\text{ST})} \right), \quad (\text{S100})$$

and there exists a critical value of  $\kappa_{\text{py}}^{(\text{C})}$ , which denoted as  $\kappa_{\text{py}}^{(\text{C})}$ , with

$$\begin{cases} \varepsilon_r^{(\text{py})} \left( \kappa_{\text{py}}^{(\text{C})} \right) = \varepsilon_f^{(\text{py})} \left( \kappa_{\text{py}}^{(\text{C})} \right) = \frac{\beta_3 + \beta_4 - \beta_6}{1/\kappa_3 + 1/\kappa_4 - 1/\kappa_6}, \\ \lambda_{\text{C}}^{(\text{py})} \equiv \lambda \left( \kappa_{\text{py}}^{(\text{C})} \right) = \frac{\phi_{\text{max}}}{\varphi_{\text{py}} / \varepsilon_{r/f}^{(\text{py})} \left( \kappa_{\text{py}}^{(\text{C})} \right) + \psi_{\text{py}} \left( \kappa_{\text{py}}^{(\text{C})} \right)}. \end{cases} \quad (\text{S101})$$

Here,  $\lambda_{\text{C}}^{(\text{py})}$  is the growth rate at the transition point, and  $\varepsilon_{r/f}^{(\text{py})}$  stands for either  $\varepsilon_r^{(\text{py})}$  or  $\varepsilon_f^{(\text{py})}$ . In Fig. S8c, we show the dependencies of  $\varepsilon_r^{(\text{py})} \left( \kappa_{\text{py}} \right)$ ,  $\varepsilon_f^{(\text{py})} \left( \kappa_{\text{py}} \right)$  and  $\lambda \left( \kappa_{\text{py}} \right)$  on  $\kappa_{\text{py}}$  in a 3-dimensional form. In the homogenous case,  $J_f^{(\text{E,py})}$  and  $J_r^{(\text{E,py})}$  follow

$$\begin{cases} J_f^{(\text{E,py})} = \varphi_{\text{py}} \cdot \lambda \cdot \theta \left( \lambda - \lambda_{\text{C}}^{(\text{py})} \right), \\ J_r^{(\text{E,py})} = \varphi_{\text{py}} \cdot \lambda \cdot \left[ 1 - \theta \left( \lambda - \lambda_{\text{C}}^{(\text{py})} \right) \right]. \end{cases} \quad (\text{S102})$$

Defining  $\lambda_{\text{max}}^{(\text{py})} = \lambda \left( \kappa_{\text{py}}^{(\text{ST})} \right)$ , and then,  $[0, \lambda_{\text{max}}^{(\text{py})}]$  is the relevant range of the x axis. To compare with experiments, we assume the same extent of extrinsic noise as specified in Sec. 2.3. Then,  $\lambda_{\text{C}}^{(\text{py})}$  roughly follows a Gaussian distribution

$$\lambda_{\text{C}}^{(\text{py})} \sim \mathcal{N} \left( \mu_{\lambda_{\text{C}}^{(\text{py})}}, \sigma_{\lambda_{\text{C}}^{(\text{py})}}^2 \right), \quad (\text{S103})$$

where  $\mu_{\lambda_{\text{C}}^{(\text{py})}}$  and  $\sigma_{\lambda_{\text{C}}^{(\text{py})}}$  stand for the mean and standard deviation of  $\lambda_{\text{C}}^{(\text{py})}$ . Then, the relations between the normalized energy fluxes and growth rate are:

$$\begin{cases} J_f^{(E,py)}(\lambda) = \frac{1}{2} \varphi_{py} \cdot \lambda \cdot \left[ \operatorname{erf} \left( \frac{\lambda - \mu_{\lambda_c^{(py)}}}{\sqrt{2}\sigma_{\lambda_c^{(py)}}} \right) + 1 \right], \\ J_r^{(E,py)}(\lambda) = \frac{1}{2} \varphi_{py} \cdot \lambda \cdot \left[ 1 - \operatorname{erf} \left( \frac{\lambda - \mu_{\lambda_c^{(py)}}}{\sqrt{2}\sigma_{\lambda_c^{(py)}}} \right) \right]. \end{cases} \quad (S104)$$

Combined with Eq. S92, we have

$$\begin{cases} J_f^{(N)}(\lambda) = \frac{\varphi_{py}}{2(\beta_6 + \beta_8)} \cdot \lambda \cdot \left[ \operatorname{erf} \left( \frac{\lambda - \mu_{\lambda_c^{(py)}}}{\sqrt{2}\sigma_{\lambda_c^{(py)}}} \right) + 1 \right], \\ J_r^{(N)}(\lambda) = \frac{\varphi_{py}}{2(\beta_3 + \beta_4 + \beta_8)} \cdot \lambda \cdot \left[ 1 - \operatorname{erf} \left( \frac{\lambda - \mu_{\lambda_c^{(py)}}}{\sqrt{2}\sigma_{\lambda_c^{(py)}}} \right) \right]. \end{cases} \quad (S105)$$

In Fig. 3f, we show that the model predictions (Eq. S105) quantitatively illustrate the experimental results<sup>13</sup>.

#### S4.2 Mixtures of a Group A carbon source with extracellular amino acids

In the case of a Group A carbon source mixed with amino acids, the coarse-grained model is shown in Fig. S3a. In fact, we can use this model to analyze the mixtures with one or multiple types of extracellular amino acids. Here, Eqs. S21, S22, S24 and S25 still apply, yet Eq. S23 changes into ( $i = a1$  stays the same as Eq. S23):

$$\Phi_i \cdot \xi_i \cdot N_{EP_i}^{\text{carbon}} + \Phi'_i \cdot \xi'_i \cdot N_{P_i}^{\text{carbon}} = r_i \cdot J_{\text{BM}} \quad (i = a2, b, c, d). \quad (S106)$$

Here,  $N_{P_i}^{\text{carbon}}$  stands for the number of carbon atoms in a molecule of Pool  $i$ . For simplicity, we assume

$$N_{P_i}^{\text{carbon}} \approx N_{EP_i}^{\text{carbon}}. \quad (S107)$$

In the case that all 21 types of amino acids are present with each saturated concentration (denoted as “21AA”),

$$\begin{cases}
\phi_A \cdot \kappa_A = \phi_1 \cdot \kappa_1 + \phi_{a1} \cdot \kappa_{a1}, \\
2\phi_1 \cdot \kappa_1 = \phi_2 \cdot \kappa_2 + \phi_5 \cdot \kappa_5 + \phi_{a2} \cdot \kappa_{a2}, \\
\phi_2 \cdot \kappa_2 = \phi_3 \cdot \kappa_3 + \phi_6 \cdot \kappa_6 + \phi_b \cdot \kappa_b, \\
\phi_5 \cdot \kappa_5 + \phi_4 \cdot \kappa_4 = \phi_3 \cdot \kappa_3 + \phi_d \cdot \kappa_d, \\
\phi_3 \cdot \kappa_3 = \phi_4 \cdot \kappa_4 + \phi_c \cdot \kappa_c, \\
\phi_{a1} \cdot \kappa_{a1} = \eta_{a1} \cdot \lambda, \phi_{a2} \cdot \kappa_{a2} + \phi_{a2}^{(21AA)} \cdot \kappa_{a2}^{(21AA)} = \eta_{a2} \cdot \lambda, \phi_b \cdot \kappa_b + \phi_b^{(21AA)} \cdot \kappa_b^{(21AA)} = \eta_b \cdot \lambda, \\
\phi_c \cdot \kappa_c + \phi_c^{(21AA)} \cdot \kappa_c^{(21AA)} = \eta_c \cdot \lambda, \phi_d \cdot \kappa_d + \phi_d^{(21AA)} \cdot \kappa_d^{(21AA)} = \eta_d \cdot \lambda, \\
\beta_1 \cdot \phi_1 \cdot \kappa_1 + \beta_2 \cdot \phi_2 \cdot \kappa_2 + \beta_3 \cdot \phi_3 \cdot \kappa_3 + \beta_4 \cdot \phi_4 \cdot \kappa_4 + \beta_6 \cdot \phi_6 \cdot \kappa_6 + \beta_{a1} \cdot \phi_{a1} \cdot \kappa_{a1} = J_E^{(N)}, \\
J_E^{(N)} = \eta_E \cdot \lambda, \lambda = \phi_R \cdot \kappa_t, J_r^{(N)} = \phi_4 \cdot \kappa_4, J_f^{(N)} = \phi_6 \cdot \kappa_6, \\
\phi_R + \phi_A + \sum_i^6 \phi_i + \sum_j^{a1, a2, b, c, d} \phi_j + \phi_{a2}^{(21AA)} + \phi_b^{(21AA)} + \phi_c^{(21AA)} + \phi_d^{(21AA)} = \phi_{\max}, 
\end{cases} \quad (S108)$$

where  $\phi_i$  and  $\kappa_i$  are defined following Eqs. S9 and S12. Since the cell growth rate elevates significantly with the mixture of amino acids, we deduce that Pools a2-d are supplied by amino acids in growth optimization, with

$$\phi_i = 0 \quad (i = a2, b, c, d). \quad (S109)$$

Basically, amino acids should be at least more efficient in the supply of biomass production than the Group A carbon source for Pools a2-d, i.e.,

$$\begin{cases}
1/\kappa_{a2}^{(21AA)} < 1/\kappa_{a2} + 1/(2\kappa_1) + 1/(2\kappa_A), \\
1/\kappa_b^{(21AA)} < 1/\kappa_b + 1/\kappa_2 + 1/(2\kappa_1) + 1/(2\kappa_A), \\
1/\kappa_c^{(21AA)} < 1/\kappa_c + 1/\kappa_5 + 1/\kappa_3 + 1/\kappa_2 + 1/\kappa_1 + 1/\kappa_A, \\
1/\kappa_d^{(21AA)} < 1/\kappa_d + 1/\kappa_5 + 1/(2\kappa_1) + 1/(2\kappa_A),
\end{cases} \quad (S110)$$

while actually it requires more since there is accompanied energy production in the biomass production pathway of the Group A carbon source yet not for amino acids. Combining Eqs. S108 and S109, we have

$$\begin{cases}
J_r^{(E)} + J_f^{(E)} = \varphi_{21AA} \cdot \lambda, \\
\frac{J_r^{(E)}}{\varepsilon_r} + \frac{J_f^{(E)}}{\varepsilon_f} = \phi_{\max} - \psi_{21AA} \cdot \lambda,
\end{cases} \quad (S111)$$

where  $J_r^{(E)}$ ,  $J_f^{(E)}$  follow Eq. S30, while  $\varepsilon_r$  and  $\varepsilon_f$  follow Eq. S31.  $\psi_{21AA}$  is the proteome efficiency of biomass production, with

$$\psi_{21AA} = \frac{1}{\kappa_t} + \frac{\eta_{a1}}{\kappa_A} + \frac{\eta_{a1}}{\kappa_{a1}} + \frac{\eta_{a2}}{\kappa_{a2}^{(21AA)}} + \frac{\eta_b}{\kappa_b^{(21AA)}} + \frac{\eta_c}{\kappa_c^{(21AA)}} + \frac{\eta_d}{\kappa_d^{(21AA)}}. \quad (S112)$$

$\varphi_{21AA}$  is the energy demand coefficient, with

$$\varphi_{21AA} \equiv \eta_E - \beta_{a1} \cdot \eta_{a1}. \quad (S113)$$

Comparing Eq. S111 with Eq. S31, it is easy to obtain the formula of the growth rate

$$\lambda(\kappa_A) = \begin{cases} \lambda_r^{(21AA)} \equiv \frac{\phi_{\max}}{\varphi_{21AA}/\varepsilon_r(\kappa_A) + \psi_{21AA}(\kappa_A)} & \varepsilon_r(\kappa_A) > \varepsilon_f(\kappa_A), \\ \lambda_f^{(21AA)} \equiv \frac{\phi_{\max}}{\varphi_{21AA}/\varepsilon_f(\kappa_A) + \psi_{21AA}(\kappa_A)} & \varepsilon_r(\kappa_A) < \varepsilon_f(\kappa_A). \end{cases} \quad (S114)$$

In fact, Eqs. S37-S42 still apply.  $\varepsilon_{r/f}(\kappa_A^{(C)})$  satisfies Eq. S43, while  $\lambda_C^{(21AA)} \equiv \lambda(\kappa_A^{(C)})$  and  $\lambda_{\max}^{(21AA)} \equiv \lambda(\kappa_A^{\max})$  change into

$$\begin{cases} \lambda_C^{(21AA)} = \frac{\phi_{\max}}{\varphi_{21AA}/\varepsilon_{r/f}(\kappa_A^{(C)}) + \psi_{21AA}(\kappa_A^{(C)})}, \\ \lambda_{\max}^{(21AA)} = \frac{\phi_{\max}}{\varphi_{21AA}/\varepsilon_f(\kappa_A^{\max}) + \psi_{21AA}(\kappa_A^{\max})}. \end{cases} \quad (S115)$$

When extrinsic noise was taken into account,  $\lambda_C^{(21AA)}$  roughly follow a Gaussian distribution

$$\lambda_C^{(21AA)} \sim \mathcal{N}(\mu_{\lambda_C^{(21AA)}}, \sigma_{\lambda_C^{(21AA)}}^2), \quad (S116)$$

and the normalized fluxes  $J_r^{(N)}, J_f^{(N)}$  change into

$$\begin{cases} J_f^{(N)}(\lambda) = \frac{\varphi_{21AA}}{\beta_1 + 2(\beta_2 + \beta_6)} \cdot \lambda \cdot \left[ \operatorname{erf} \left( \frac{\lambda - \mu_{\lambda_C^{(21AA)}}}{\sqrt{2}\sigma_{\lambda_C^{(21AA)}}} \right) + 1 \right], \\ J_r^{(N)}(\lambda) = \frac{\varphi_{21AA}}{\beta_1 + 2(\beta_2 + \beta_3 + \beta_4)} \cdot \lambda \cdot \left[ 1 - \operatorname{erf} \left( \frac{\lambda - \mu_{\lambda_C^{(21AA)}}}{\sqrt{2}\sigma_{\lambda_C^{(21AA)}}} \right) \right]. \end{cases} \quad (S117)$$

In fact, the above analysis can be extended to cases with arbitrary combination of amino acids. Eqs. S111, S114-S117 would remain the form, while Eqs. S112-S113 would change depending on the amino acid combinations. In Fig. S3 b-c, we show the comparisons between model predictions (see also Sec. S7.2

and Eq. S157) experimental data<sup>10,16</sup> in mixtures of 21 or 7 types of amino acids together with a Group A carbon source, which agree quantitatively overall.

## S5 Enzyme allocation upon perturbations

### S5.1 Carbon limitation within Group A carbon sources

In Eq. S28, we show the model predictions of the dependencies of enzyme protein fractions on growth rate and energy fluxes. To compare with experiments, we assume the same extent of extrinsic noise as specified in Sec. 2.3. In fact, the relative protein expression data for the enzyme within glycolysis and TCA cycle are available from existing studies, basically, comparable to the  $\phi_1$ - $\phi_4$  enzymes of our model (Fig. 1b). Upon  $\kappa_A$  perturbations,  $\kappa_A$  is a variable while  $\kappa_i$  is fixed (see Sec. 1.5), combining Eqs. S28 and S47, we have

$$\begin{cases} \phi_1 = \frac{\lambda}{\kappa_1} \left\{ \frac{\varphi \cdot (\beta_3 + \beta_4 - \beta_6)}{[\beta_1 + 2(\beta_2 + \beta_3 + \beta_4)] \cdot [\beta_1 + 2(\beta_2 + \beta_6)]} \cdot \left[ \operatorname{erf} \left( \frac{\lambda - \mu_{\lambda_c}}{\sqrt{2}\sigma_{\lambda_c}} \right) + 1 \right] + \frac{\varphi}{\beta_1 + 2(\beta_2 + \beta_3 + \beta_4)} + \frac{\eta_{a2} + \eta_b + 2\eta_c + \eta_d}{2} \right\}, \\ \phi_2 = \frac{\lambda}{\kappa_2} \left\{ \frac{2\varphi \cdot (\beta_3 + \beta_4 - \beta_6)}{[\beta_1 + 2(\beta_2 + \beta_3 + \beta_4)] \cdot [\beta_1 + 2(\beta_2 + \beta_6)]} \cdot \left[ \operatorname{erf} \left( \frac{\lambda - \mu_{\lambda_c}}{\sqrt{2}\sigma_{\lambda_c}} \right) + 1 \right] + \frac{2\varphi}{\beta_1 + 2(\beta_2 + \beta_3 + \beta_4)} + \eta_b + \eta_c \right\}, \\ \phi_3 = \frac{\lambda}{\kappa_3} \left\{ \frac{\varphi}{\beta_1 + 2(\beta_2 + \beta_3 + \beta_4)} \cdot \left[ 1 - \operatorname{erf} \left( \frac{\lambda - \mu_{\lambda_c}}{\sqrt{2}\sigma_{\lambda_c}} \right) \right] + \eta_c \right\}, \\ \phi_4 = \frac{\lambda}{\kappa_4} \cdot \frac{\varphi}{\beta_1 + 2(\beta_2 + \beta_3 + \beta_4)} \cdot \left[ 1 - \operatorname{erf} \left( \frac{\lambda - \mu_{\lambda_c}}{\sqrt{2}\sigma_{\lambda_c}} \right) \right]. \end{cases} \quad (\text{S118})$$

In Fig. S5c-d, we show the comparisons between model predictions (Eq. S118,  $w_0 = 0$ ) and experimental data<sup>17</sup>, which are well consistent overall. We proceed to consider the influences of maintenance energy as specified in Sec. 3.2. Still, we choose  $w_0 = 2.5 \text{ (h}^{-1}\text{)}$  as previously adopted in Sec. 3.3. Then, Eq. S28 still holds, combined with Eq. S85 in the condition that  $\iota = 0$ , we have

$$\begin{cases} \phi_1 = \frac{1}{2 \cdot \kappa_1} \left\{ \frac{\varphi \cdot \lambda + w_0}{\beta_1 + 2(\beta_2 + \beta_6)} \cdot \left[ \operatorname{erf} \left( \frac{\lambda - \mu_{\lambda_c}}{\sqrt{2}\sigma_{\lambda_c}} \right) + 1 \right] + \frac{\varphi \cdot \lambda + w_0}{\beta_1 + 2(\beta_2 + \beta_3 + \beta_4)} \cdot \left[ 1 - \operatorname{erf} \left( \frac{\lambda - \mu_{\lambda_c}}{\sqrt{2}\sigma_{\lambda_c}} \right) \right] + (\eta_{a2} + \eta_b + 2\eta_c + \eta_d) \lambda \right\}, \\ \phi_2 = \frac{1}{\kappa_2} \left\{ \frac{\varphi \cdot \lambda + w_0}{\beta_1 + 2(\beta_2 + \beta_6)} \cdot \left[ \operatorname{erf} \left( \frac{\lambda - \mu_{\lambda_c}}{\sqrt{2}\sigma_{\lambda_c}} \right) + 1 \right] + \frac{\varphi \cdot \lambda + w_0}{\beta_1 + 2(\beta_2 + \beta_3 + \beta_4)} \cdot \left[ 1 - \operatorname{erf} \left( \frac{\lambda - \mu_{\lambda_c}}{\sqrt{2}\sigma_{\lambda_c}} \right) \right] + (\eta_b + \eta_c) \lambda \right\}, \\ \phi_3 = \frac{1}{\kappa_3} \left\{ \frac{\varphi \cdot \lambda + w_0}{\beta_1 + 2(\beta_2 + \beta_3 + \beta_4)} \cdot \left[ 1 - \operatorname{erf} \left( \frac{\lambda - \mu_{\lambda_c}}{\sqrt{2}\sigma_{\lambda_c}} \right) \right] + \eta_c \cdot \lambda \right\}, \\ \phi_4 = \frac{1}{\kappa_4} \cdot \frac{\varphi \cdot \lambda + w_0}{\beta_1 + 2(\beta_2 + \beta_3 + \beta_4)} \cdot \left[ 1 - \operatorname{erf} \left( \frac{\lambda - \mu_{\lambda_c}}{\sqrt{2}\sigma_{\lambda_c}} \right) \right]. \end{cases} \quad (\text{S119})$$

In Fig. 4a-b, we show that the model predictions (Eq. S119,  $w_0 = 2.5 \text{ (} h^{-1} \text{)}$ ) overall agree with the experiments<sup>17</sup>. Still, there are different basal expressions of these enzymes, which is probably due to the living demands other than growth, such as the preparation for starvation<sup>18</sup> or alternation in the type of the nutrient<sup>19,20</sup>.

## S5.2 Overexpression of useless proteins

In the case that  $\phi_z$  is perturbed in each culturing environment with fixed  $\kappa_A$  (see Sec. 3.1), where we consider the same extent of extrinsic noise as specified in Sec. 2.3, the relations between enzyme allocations and the growth rate can be obtained by combining Eqs. S28 and S58:

$$\left\{ \begin{array}{l} \phi_1 = \frac{\lambda}{2 \cdot \kappa_1} \left\{ \frac{\varphi \cdot \left[ 1 - \text{erf} \left( \frac{\lambda(\kappa_A, 0) - \mu_{\lambda_c}(0)}{\sqrt{2} \sigma_{\lambda_c}(0)} \right) \right]}{\beta_1 + 2(\beta_2 + \beta_3 + \beta_4)} + \frac{\varphi \cdot \left[ \text{erf} \left( \frac{\lambda(\kappa_A, 0) - \mu_{\lambda_c}(0)}{\sqrt{2} \sigma_{\lambda_c}(0)} \right) + 1 \right]}{\beta_1 + 2(\beta_2 + \beta_6)} + (\eta_{a2} + \eta_b + 2\eta_c + \eta_d) \right\}, \\ \phi_2 = \frac{\lambda}{\kappa_2} \left\{ \frac{\varphi \cdot \left[ 1 - \text{erf} \left( \frac{\lambda(\kappa_A, 0) - \mu_{\lambda_c}(0)}{\sqrt{2} \sigma_{\lambda_c}(0)} \right) \right]}{\beta_1 + 2(\beta_2 + \beta_3 + \beta_4)} + \frac{\varphi \cdot \left[ \text{erf} \left( \frac{\lambda(\kappa_A, 0) - \mu_{\lambda_c}(0)}{\sqrt{2} \sigma_{\lambda_c}(0)} \right) + 1 \right]}{\beta_1 + 2(\beta_2 + \beta_6)} + (\eta_b + \eta_c) \right\}, \\ \phi_3 = \frac{\lambda}{\kappa_3} \left\{ \frac{\varphi}{\beta_1 + 2(\beta_2 + \beta_3 + \beta_4)} \cdot \left[ 1 - \text{erf} \left( \frac{\lambda(\kappa_A, 0) - \mu_{\lambda_c}(0)}{\sqrt{2} \sigma_{\lambda_c}(0)} \right) \right] + \eta_c \right\}, \\ \phi_4 = \frac{\lambda}{\kappa_4} \left\{ \frac{\varphi}{\beta_1 + 2(\beta_2 + \beta_3 + \beta_4)} \cdot \left[ 1 - \text{erf} \left( \frac{\lambda(\kappa_A, 0) - \mu_{\lambda_c}(0)}{\sqrt{2} \sigma_{\lambda_c}(0)} \right) \right] \right\}, \end{array} \right. \quad (S120)$$

where  $\lambda(\kappa_A, 0)$  is the growth rate with  $\phi_z = 0$ , and thus is a parameter rather than a variable. The growth rate is defined as  $\lambda(\kappa_A, \phi_z)$ , which follows Eq. S50. Thus,  $\phi_i$  is proportional to the growth rate  $\lambda$ . In Fig. S6a-d, we see that the model predictions (Eq. S120) agree with the experiments<sup>10</sup> overall. Then, we consider the influences of maintenance energy with  $w_0 = 2.5$ . Combining Eqs. S28, S58 and S85 (with  $\iota = 0$ ), we have

$$\begin{cases}
\phi_1 = \frac{w_0}{2 \cdot \kappa_1} \left\{ \frac{1}{\beta_1 + 2(\beta_2 + \beta_6)} \cdot \left[ \operatorname{erf} \left( \frac{\lambda(\kappa_A, 0) - \mu_{\lambda_c}(0)}{\sqrt{2}\sigma_{\lambda_c}(0)} \right) + 1 \right] + \frac{1}{\beta_1 + 2(\beta_2 + \beta_3 + \beta_4)} \cdot \left[ 1 - \operatorname{erf} \left( \frac{\lambda(\kappa_A, 0) - \mu_{\lambda_c}(0)}{\sqrt{2}\sigma_{\lambda_c}(0)} \right) \right] \right\} \\
+ \frac{\lambda}{2 \cdot \kappa_1} \left\{ \frac{\varphi}{\beta_1 + 2(\beta_2 + \beta_6)} \cdot \left[ \operatorname{erf} \left( \frac{\lambda(\kappa_A, 0) - \mu_{\lambda_c}(0)}{\sqrt{2}\sigma_{\lambda_c}(0)} \right) + 1 \right] + \frac{\varphi}{\beta_1 + 2(\beta_2 + \beta_3 + \beta_4)} \cdot \left[ 1 - \operatorname{erf} \left( \frac{\lambda(\kappa_A, 0) - \mu_{\lambda_c}(0)}{\sqrt{2}\sigma_{\lambda_c}(0)} \right) \right] + (\eta_{a2} + \eta_b + 2\eta_c + \eta_d) \right\}, \\
\phi_2 = \frac{w_0}{\kappa_2} \left\{ \frac{1}{\beta_1 + 2(\beta_2 + \beta_6)} \cdot \left[ \operatorname{erf} \left( \frac{\lambda(\kappa_A, 0) - \mu_{\lambda_c}(0)}{\sqrt{2}\sigma_{\lambda_c}(0)} \right) + 1 \right] + \frac{1}{\beta_1 + 2(\beta_2 + \beta_3 + \beta_4)} \cdot \left[ 1 - \operatorname{erf} \left( \frac{\lambda(\kappa_A, 0) - \mu_{\lambda_c}(0)}{\sqrt{2}\sigma_{\lambda_c}(0)} \right) \right] \right\} \\
+ \frac{\lambda}{\kappa_2} \left\{ \frac{\varphi}{\beta_1 + 2(\beta_2 + \beta_6)} \cdot \left[ \operatorname{erf} \left( \frac{\lambda(\kappa_A, 0) - \mu_{\lambda_c}(0)}{\sqrt{2}\sigma_{\lambda_c}(0)} \right) + 1 \right] + \frac{\varphi}{\beta_1 + 2(\beta_2 + \beta_3 + \beta_4)} \cdot \left[ 1 - \operatorname{erf} \left( \frac{\lambda(\kappa_A, 0) - \mu_{\lambda_c}(0)}{\sqrt{2}\sigma_{\lambda_c}(0)} \right) \right] + (\eta_b + \eta_c) \right\}, \\
\phi_3 = \frac{\lambda}{\kappa_3} \left\{ \frac{\varphi}{\beta_1 + 2(\beta_2 + \beta_3 + \beta_4)} \cdot \left[ 1 - \operatorname{erf} \left( \frac{\lambda(\kappa_A, 0) - \mu_{\lambda_c}(0)}{\sqrt{2}\sigma_{\lambda_c}(0)} \right) \right] + \eta_c \right\} + \frac{w_0}{\kappa_3} \cdot \frac{1}{\beta_1 + 2(\beta_2 + \beta_3 + \beta_4)} \cdot \left[ 1 - \operatorname{erf} \left( \frac{\lambda(\kappa_A, 0) - \mu_{\lambda_c}(0)}{\sqrt{2}\sigma_{\lambda_c}(0)} \right) \right], \\
\phi_4 = \frac{\lambda}{\kappa_4} \cdot \frac{\varphi}{\beta_1 + 2(\beta_2 + \beta_3 + \beta_4)} \cdot \left[ 1 - \operatorname{erf} \left( \frac{\lambda(\kappa_A, 0) - \mu_{\lambda_c}(0)}{\sqrt{2}\sigma_{\lambda_c}(0)} \right) \right] + \frac{w_0}{\kappa_4} \cdot \frac{1}{\beta_1 + 2(\beta_2 + \beta_3 + \beta_4)} \cdot \left[ 1 - \operatorname{erf} \left( \frac{\lambda(\kappa_A, 0) - \mu_{\lambda_c}(0)}{\sqrt{2}\sigma_{\lambda_c}(0)} \right) \right].
\end{cases} \quad (S121)$$

Here, the grow rate is defined as  $\lambda(\kappa_A, \phi_z)$ , and  $\lambda(\kappa_A, 0)$  is a parameter rather than a variable. Thus,  $\phi_i$  is a linear function of the growth rate  $\lambda$ , with a positive slope and a positive intercept. In Figs. 4c-d and S6e-f, we show that the model predictions (Eq. S121) agree quantitatively with the experimental data<sup>10</sup>.

### S5.3 Energy dissipation

In the case that energy dissipation is perturbed in each nutrient environment, basically,  $w$  is perturbed while  $\kappa_A$  is fixed. The relationship between protein allocation and the growth rate can be obtained by combining Eqs. S28 and S70. However, since  $w$  is explicitly present in Eq. S70, we need to reduce this variable to get the desired relations. In fact, from Eq. S64, we have

$$\lambda(\kappa_A, w) = \lambda(\kappa_A, 0) \left\{ 1 - \frac{w}{\phi_{\max}} \cdot \left[ \frac{1}{\varepsilon_r(\kappa_A)} - \theta(\varepsilon_f(\kappa_A) - \varepsilon_r(\kappa_A)) \cdot \left( \frac{1}{\varepsilon_r(\kappa_A)} - \frac{1}{\varepsilon_f(\kappa_A)} \right) \right] \right\}, \quad (S122)$$

where  $\lambda(\kappa_A, 0) = \lambda(\kappa_A, w=0)$  (satisfying Eq. S64), which is a parameter rather than a variable. “ $\theta$ ” stands for the Heaviside step function. Thus, we have

$$w(\lambda) = \frac{\phi_{\max} \cdot [1 - \lambda/\lambda(\kappa_A, 0)]}{\left[ 1/\varepsilon_r(\kappa_A) - \theta(\varepsilon_f(\kappa_A) - \varepsilon_r(\kappa_A)) \cdot (1/\varepsilon_r(\kappa_A) - 1/\varepsilon_f(\kappa_A)) \right]}, \quad (S123)$$

where the energy dissipation coefficient  $w$  is regarded as a function of the growth rate. Combining Eqs. S28, S70 and S123, we have

$$\begin{cases}
\phi_1 = \frac{1}{2\kappa_1} \left[ \left[ \frac{\varphi \cdot \lambda + w(\lambda)}{\beta_1 + 2(\beta_2 + \beta_6)} - \frac{\varphi \cdot \lambda + w(\lambda)}{\beta_1 + 2(\beta_2 + \beta_3 + \beta_4)} \right] \cdot \text{erf} \left( \frac{\lambda - \mu_{\lambda_c}(0) \left\{ 1 - w \left[ \frac{\varepsilon_{r/f}(\kappa_A^{(C)}) \phi_{\max}}{\sqrt{2} \sigma_{\lambda_c}(0)} \right] \right\}}{\sqrt{2} \sigma_{\lambda_c}(0) \left\{ 1 - w \left[ \frac{\varepsilon_{r/f}(\kappa_A^{(C)}) \phi_{\max}}{\sqrt{2} \sigma_{\lambda_c}(0)} \right] \right\}} \right) + 1 \right] + \frac{2[\varphi \cdot \lambda + w(\lambda)]}{\beta_1 + 2(\beta_2 + \beta_3 + \beta_4)} + (\eta_{a2} + \eta_b + 2\eta_c + \eta_d) \cdot \lambda, \\
\phi_2 = \frac{1}{\kappa_2} \left[ \left[ \frac{\varphi \cdot \lambda + w(\lambda)}{\beta_1 + 2(\beta_2 + \beta_6)} - \frac{\varphi \cdot \lambda + w(\lambda)}{\beta_1 + 2(\beta_2 + \beta_3 + \beta_4)} \right] \cdot \text{erf} \left( \frac{\lambda - \mu_{\lambda_c}(0) \left\{ 1 - w \left[ \frac{\varepsilon_{r/f}(\kappa_A^{(C)}) \phi_{\max}}{\sqrt{2} \sigma_{\lambda_c}(0)} \right] \right\}}{\sqrt{2} \sigma_{\lambda_c}(0) \left\{ 1 - w \left[ \frac{\varepsilon_{r/f}(\kappa_A^{(C)}) \phi_{\max}}{\sqrt{2} \sigma_{\lambda_c}(0)} \right] \right\}} \right) + 1 \right] + \frac{2[\varphi \cdot \lambda + w(\lambda)]}{\beta_1 + 2(\beta_2 + \beta_3 + \beta_4)} + (\eta_b + \eta_c) \cdot \lambda, \\
\phi_3 = \frac{1}{\kappa_3} \left[ \frac{\varphi \cdot \lambda + w(\lambda)}{\beta_1 + 2(\beta_2 + \beta_3 + \beta_4)} \cdot \left[ 1 - \text{erf} \left( \frac{\lambda - \mu_{\lambda_c}(0) \left\{ 1 - w(\lambda) \left[ \frac{\varepsilon_{r/f}(\kappa_A^{(C)}) \phi_{\max}}{\sqrt{2} \sigma_{\lambda_c}(0)} \right] \right\}}{\sqrt{2} \sigma_{\lambda_c}(0) \left\{ 1 - w(\lambda) \left[ \frac{\varepsilon_{r/f}(\kappa_A^{(C)}) \phi_{\max}}{\sqrt{2} \sigma_{\lambda_c}(0)} \right] \right\}} \right) \right] + \eta_c \cdot \lambda, \\
\phi_4 = \frac{1}{\kappa_4} \cdot \frac{\varphi \cdot \lambda + w(\lambda)}{\beta_1 + 2(\beta_2 + \beta_3 + \beta_4)} \cdot \left[ 1 - \text{erf} \left( \frac{\lambda - \mu_{\lambda_c}(0) \left\{ 1 - w(\lambda) \left[ \frac{\varepsilon_{r/f}(\kappa_A^{(C)}) \phi_{\max}}{\sqrt{2} \sigma_{\lambda_c}(0)} \right] \right\}}{\sqrt{2} \sigma_{\lambda_c}(0) \left\{ 1 - w(\lambda) \left[ \frac{\varepsilon_{r/f}(\kappa_A^{(C)}) \phi_{\max}}{\sqrt{2} \sigma_{\lambda_c}(0)} \right] \right\}} \right) \right], 
\end{cases} \quad (S124)$$

where  $w(\lambda)$  follows Eq. S123. When  $\kappa_A$  lies in the vicinity of  $\kappa_A^{(C)}$  or  $w$  is small so that

$$\left( 1 - \frac{w}{\varepsilon_{r/f}(\kappa_A) \cdot \phi_{\max}} \right) \left/ \left( 1 - \frac{w}{\varepsilon_{r/f}(\kappa_A^{(C)}) \cdot \phi_{\max}} \right) \right. \approx 1, \quad (S125)$$

then, we have

$$\begin{cases}
J_f^{(N)}(\lambda, w) = \frac{\varphi \cdot \lambda + w}{\beta_1 + 2(\beta_2 + \beta_6)} \cdot \left[ \text{erf} \left( \frac{\lambda(\kappa_A, 0) - \mu_{\lambda_c}(0)}{\sqrt{2} \sigma_{\lambda_c}(0)} \right) + 1 \right], \\
J_r^{(N)}(\lambda, w) = \frac{\varphi \cdot \lambda + w}{\beta_1 + 2(\beta_2 + \beta_3 + \beta_4)} \cdot \left[ 1 - \text{erf} \left( \frac{\lambda(\kappa_A, 0) - \mu_{\lambda_c}(0)}{\sqrt{2} \sigma_{\lambda_c}(0)} \right) \right],
\end{cases} \quad (S126)$$

and thus

$$\begin{cases}
\phi_1 = \frac{1}{2\kappa_1} \left[ \left[ \frac{\varphi \cdot \lambda + w(\lambda)}{\beta_1 + 2(\beta_2 + \beta_6)} - \frac{\varphi \cdot \lambda + w(\lambda)}{\beta_1 + 2(\beta_2 + \beta_3 + \beta_4)} \right] \cdot \text{erf} \left( \frac{\lambda(\kappa_A, 0) - \mu_{\lambda_c}(0)}{\sqrt{2} \sigma_{\lambda_c}(0)} \right) + 1 \right] + \frac{2[\varphi \cdot \lambda + w(\lambda)]}{\beta_1 + 2(\beta_2 + \beta_3 + \beta_4)} + (\eta_{a2} + \eta_b + 2\eta_c + \eta_d) \cdot \lambda, \\
\phi_2 = \frac{1}{\kappa_2} \left[ \left[ \frac{\varphi \cdot \lambda + w(\lambda)}{\beta_1 + 2(\beta_2 + \beta_6)} - \frac{\varphi \cdot \lambda + w(\lambda)}{\beta_1 + 2(\beta_2 + \beta_3 + \beta_4)} \right] \cdot \text{erf} \left( \frac{\lambda(\kappa_A, 0) - \mu_{\lambda_c}(0)}{\sqrt{2} \sigma_{\lambda_c}(0)} \right) + 1 \right] + \frac{2[\varphi \cdot \lambda + w(\lambda)]}{\beta_1 + 2(\beta_2 + \beta_3 + \beta_4)} + (\eta_b + \eta_c) \cdot \lambda, \\
\phi_3 = \frac{1}{\kappa_3} \left[ \frac{\varphi \cdot \lambda + w(\lambda)}{\beta_1 + 2(\beta_2 + \beta_3 + \beta_4)} \cdot \left[ 1 - \text{erf} \left( \frac{\lambda(\kappa_A, 0) - \mu_{\lambda_c}(0)}{\sqrt{2} \sigma_{\lambda_c}(0)} \right) \right] + \eta_c \cdot \lambda \right], \\
\phi_4 = \frac{1}{\kappa_4} \cdot \frac{\varphi \cdot \lambda + w(\lambda)}{\beta_1 + 2(\beta_2 + \beta_3 + \beta_4)} \cdot \left[ 1 - \text{erf} \left( \frac{\lambda(\kappa_A, 0) - \mu_{\lambda_c}(0)}{\sqrt{2} \sigma_{\lambda_c}(0)} \right) \right],
\end{cases} \quad (S127)$$

Note that in Eq. S123,  $w$  is a linear function of  $\lambda$  with a negative slope, and thus  $\phi_i$  presents a linear relation with  $\lambda$  when Eq. S125 is satisfied (see Eq. S127). In fact, the slope of  $\phi_4$  is surely negative

(combining Eqs. S64, S123 and S127), while the slope sign of other  $\phi_i$  depends on the parameters. For a given nutrient, enzymes correspond to the same  $\phi_i$  should present the same sign in the slope, and if the sign of slope is negative for  $\phi_1$ , it is then surely negative for  $\phi_2$ . In Fig. S7, we show that our model agrees well with the experimental results<sup>10</sup> (Eq. S127).

## S6 Other aspects of the model

### S6.1 A coarse-grained model with more details

To compare with experiments, we consider a coarse-grained model with more details as shown in Fig. S8a. Here, nodes  $M_6$ ,  $M_7$  stand for GA3P and DHAP, respectively. Other nodes follow descriptions specified in Sec. 2.1. The biochemical reaction each follow Eq. S5 with  $b_i = 1$  except that  $M_1 \rightarrow M_6 + M_7$  and  $M_3 + M_5 \rightarrow M_4$ . By applying flux balance of the stoichiometric fluxes combining with Eq. S8, we have

$$\left\{ \begin{array}{l} \Phi_A \cdot \xi_A = \Phi_1 \cdot \xi_1 + \Phi_{a1} \cdot \xi_{a1}, \\ \Phi_{11} \cdot \xi_{11} = \Phi_{10} \cdot \xi_{10} + \Phi_1 \cdot \xi_1, \Phi_{10} \cdot \xi_{10} = \Phi_1 \cdot \xi_1, \\ \Phi_{11} \cdot \xi_{11} = \Phi_2 \cdot \xi_2 + \Phi_5 \cdot \xi_5 + \Phi_{a2} \cdot \xi_{a2}, \\ \Phi_2 \cdot \xi_2 = \Phi_3 \cdot \xi_3 + \Phi_6 \cdot \xi_6 + \Phi_b \cdot \xi_b, \\ \Phi_5 \cdot \xi_5 + \Phi_4 \cdot \xi_4 = \Phi_3 \cdot \xi_3 + \Phi_d \cdot \xi_d, \\ \Phi_3 \cdot \xi_3 = \Phi_4 \cdot \xi_4 + \Phi_c \cdot \xi_c, \end{array} \right. \quad (S128)$$

while Eqs. S22-S25 still hold. By applying the substitution specified in Eqs. S9, S12, S14-S18, combined with Eqs. S4, S10, S22-S25, S128 and the constraint of proteome resource allocation, we have

$$\left\{ \begin{array}{l} \phi_A \cdot \kappa_A = \phi_1 \cdot \kappa_1 + \phi_{a1} \cdot \kappa_{a1}, \\ \phi_{11} \cdot \kappa_{11} = \phi_{10} \cdot \kappa_{10} + \phi_1 \cdot \kappa_1, \phi_{10} \cdot \kappa_{10} = \phi_1 \cdot \kappa_1, \\ \phi_{11} \cdot \kappa_{11} = \phi_2 \cdot \kappa_2 + \phi_5 \cdot \kappa_5 + \phi_{a2} \cdot \kappa_{a2}, \\ \phi_2 \cdot \kappa_2 = \phi_3 \cdot \kappa_3 + \phi_6 \cdot \kappa_6 + \phi_b \cdot \kappa_b, \\ \phi_5 \cdot \kappa_5 + \phi_4 \cdot \kappa_4 = \phi_3 \cdot \kappa_3 + \phi_d \cdot \kappa_d, \\ \phi_3 \cdot \kappa_3 = \phi_4 \cdot \kappa_4 + \phi_c \cdot \kappa_c, \\ \phi_{a1} \cdot \kappa_{a1} = \eta_{a1} \cdot \lambda, \phi_{a2} \cdot \kappa_{a2} = \eta_{a2} \cdot \lambda, \phi_b \cdot \kappa_b = \eta_b \cdot \lambda, \phi_c \cdot \kappa_c = \eta_c \cdot \lambda, \phi_d \cdot \kappa_d = \eta_d \cdot \lambda, \\ \beta_1 \cdot \phi_1 \cdot \kappa_1 + \beta_2 \cdot \phi_2 \cdot \kappa_2 + \beta_3 \cdot \phi_3 \cdot \kappa_3 + \beta_4 \cdot \phi_4 \cdot \kappa_4 + \beta_6 \cdot \phi_6 \cdot \kappa_6 + \beta_{a1} \cdot \phi_{a1} \cdot \kappa_{a1} = J_E^{(N)}, \\ J_E^{(N)} = \eta_E \cdot \lambda, \lambda = \phi_R \cdot \kappa_t, J_r^{(N)} = \phi_4 \cdot \kappa_4, J_f^{(N)} = \phi_6 \cdot \kappa_6, \\ \phi_R + \phi_A + \phi_1 + \phi_2 + \phi_3 + \phi_4 + \phi_5 + \phi_6 + \phi_7 + \phi_8 + \phi_{a1} + \phi_{a2} + \phi_b + \phi_c + \phi_d = \phi_{\max}. \end{array} \right. \quad (S129)$$

Then, Eq. S28 still hold, while  $\phi_{10}$  and  $\phi_{11}$  are

$$\begin{cases} \phi_{10} = \left[ J_r^{(N)} + J_f^{(N)} + (\eta_{a2} + \eta_b + 2\eta_c + \eta_d) \lambda \right] / (2 \cdot \kappa_{10}), \\ \phi_{11} = \left[ J_r^{(N)} + J_f^{(N)} + (\eta_{a2} + \eta_b + 2\eta_c + \eta_d) \lambda \right] / \kappa_{11}. \end{cases} \quad (S130)$$

By substituting Eqs. S28 and S130 into Eq. S129, we have

$$\begin{cases} J_r^{(E)} + J_f^{(E)} = \varphi \cdot \lambda, \\ \frac{J_r^{(E)}}{\varepsilon_r^{(dt)}} + \frac{J_f^{(E)}}{\varepsilon_f^{(dt)}} = \phi_{\max} - \psi_{dt} \cdot \lambda, \end{cases} \quad (S131)$$

where “dt” stands for details. Eqs. S30 and S33 still hold.  $\varepsilon_r^{(dt)}$  and  $\varepsilon_f^{(dt)}$  represent the proteome energy efficiencies of respiration and fermentation, with

$$\begin{cases} \varepsilon_r^{(dt)} = \frac{\beta_1/2 + \beta_2 + \beta_3 + \beta_4}{1/(2\kappa_A) + 1/(2\kappa_1) + 1/(2\kappa_{10}) + 1/\kappa_{11} + 1/\kappa_2 + 1/\kappa_3 + 1/\kappa_4}, \\ \varepsilon_f^{(dt)} = \frac{\beta_1/2 + \beta_2 + \beta_6}{1/(2\kappa_A) + 1/(2\kappa_1) + 1/(2\kappa_{10}) + 1/\kappa_{11} + 1/\kappa_2 + 1/\kappa_6}. \end{cases} \quad (S132)$$

$\psi_{dt}^{-1}$  is the proteome efficiency of biomass pathway, with

$$\psi_{dt} = \frac{1}{\kappa_t} + \frac{1 + \eta_{a1} + \eta_c}{2\kappa_A} + (\eta_{a2} + \eta_b + 2\eta_c + \eta_d) \left( \frac{1}{2\kappa_1} + \frac{1}{2\kappa_{10}} + \frac{1}{\kappa_{11}} \right) + \frac{\eta_b + \eta_c}{\kappa_2} + \frac{\eta_c}{\kappa_3} + \frac{\eta_c + \eta_d}{\kappa_5} + \sum_i^{a1, a2, b, c, d} \frac{\eta_i}{\kappa_i}. \quad (S133)$$

## S6.2 Estimation of the in vivo enzyme catalytic rates

We use the method introduced by Davidi *et al.*<sup>21</sup> combined with proteome experimental data<sup>10</sup> (Table S2) to estimate the in vivo enzyme catalytic rates. Combing Eqs. S28 and S130, we have

$$\begin{cases} \kappa_1 = \left[ J_r^{(N)} + J_f^{(N)} + (\eta_{a2} + \eta_b + 2\eta_c + \eta_d) \lambda \right] / (2 \cdot \phi_1), \\ \kappa_2 = \left[ J_r^{(N)} + J_f^{(N)} + (\eta_b + \eta_c) \lambda \right] / \phi_2, \\ \kappa_3 = (J_r^{(N)} + \eta_c \cdot \lambda) / \phi_3, \kappa_4 = J_r^{(N)} / \phi_4, \\ \kappa_5 = (\eta_c + \eta_d) \lambda / \phi_5, \kappa_6 = J_f^{(N)} / \phi_6, \\ \kappa_{10} = \left[ J_r^{(N)} + J_f^{(N)} + (\eta_{a2} + \eta_b + 2\eta_c + \eta_d) \lambda \right] / (2 \cdot \phi_{10}), \\ \kappa_{11} = \left[ J_r^{(N)} + J_f^{(N)} + (\eta_{a2} + \eta_b + 2\eta_c + \eta_d) \lambda \right] / \phi_{11}. \end{cases} \quad (S134)$$

Here,  $J_r^{(N)}$ ,  $J_f^{(N)}$ ,  $\lambda$  and  $\phi_i$  ( $i=1-6,10-11$ ) are measurable from experiments (see Sec.8.1). Thus, we can obtain the in vivo values of  $\kappa_i$  from Eq. S134. Combined with Eqs. S17 and S20, we have

$$k_i^{\text{cat}} = \frac{r_{\text{carbon}}}{r_{\text{protein}}} \cdot \frac{m_{E_i}}{m_{\text{carbon}}} \cdot \kappa_i \cdot \left[ \sum_i r_i / N_{\text{EP}_i}^{\text{carbon}} \right], \quad (\text{S135})$$

which are the in vivo results of the enzyme catalytic rates. In Fig. S8b, we show the comparison between the in vivo and in intro results of the  $k_{\text{cat}}$  values for enzymes within glycolysis and the TCA cycle, which show good consistency overall. In the applications, we prioritize the use of in vivo results of enzyme catalytic rates, and use in intro data as the substitute when there is a vacancy.

### S6.3 Comparisons with existing models that illustrate experimental results

In Sec.2, the normalized stoichiometric influx of a Group A carbon source is

$$J_{in}^{(N)} \equiv J_A^{(N)} = \phi_A \cdot \kappa_A. \quad (\text{S136})$$

Combined with the first equation in Eq. S28, we have

$$J_{in}^{(N)} - \vartheta \cdot \lambda = \frac{J_r^{(E)}}{e_r} + \frac{J_f^{(E)}}{e_f}, \quad (\text{S137})$$

where  $e_r = \beta_1 + 2(\beta_2 + \beta_3 + \beta_4)$ ,  $e_f = \beta_1 + 2(\beta_2 + \beta_6)$ , and  $\vartheta = \eta_{a1} + \eta_c + (\eta_{a2} + \eta_b + \eta_d)/2$ .

Obviously,  $e_r$ ,  $e_f$  and  $\vartheta$  are constant parameters. Below we show the major differences of our model presented in Sec. 2 with the existing models that may illustrate the growth rate dependence of fermentation flux in the standard picture<sup>10,13,22,23</sup> of overflow metabolism. Basically, based on the modeling principles rather than the detailed mechanisms, there are two major classes of existing models that illustrate experimental results. In fact, both classes of models regard the proteome energy efficiencies  $\varepsilon_r$  and  $\varepsilon_f$  as constants, with  $\varepsilon_f > \varepsilon_r$  if used, or follow functionally equivalent propositions. By contrast, in our model,  $\varepsilon_r$  and  $\varepsilon_f$  are both functions of  $\kappa_A$  which vary significantly upon nutrient perturbations, where  $\varepsilon_r(\kappa_A \rightarrow 0) > \varepsilon_f(\kappa_A \rightarrow 0)$  and  $\varepsilon_r(\kappa_A^{\max}) < \varepsilon_f(\kappa_A^{\max})$  (see Eqs. S38, S40-S41). Furthermore, in terms of modeling/optimization principles, there are significant differences as listed below.

The first class of models<sup>12,24-31</sup> optimize the ratio of influx to biomass outflow:  $J_{in}^{(N)}/\lambda$ . Either to optimize growth rate for a given influx, or to minimize the influx for a given growth rate. For a given quantity of the Group A carbon source, e.g., glucose, the respiration pathway generates much more ATPs than the fermentation pathway. Thus, to optimize the ratio  $J_{in}^{(N)}/\lambda$ , the cells would preferentially use the respiration pathway when the influx is small. As the influx increases above a threshold, factors such as

proteome allocation navigate the cells into the fermentation pathway in an analog way since  $\varepsilon_f > \varepsilon_r$ . Our model is significantly different from this class of models in the optimization principles, where we purely optimize the growth rate without any further constraint on the influx, while the first class of models effectively impose restrictions on the influx.

The representative of the second class of models<sup>10,32</sup> is Basan *et al.*<sup>10</sup>. Although Basan *et al.*<sup>10</sup> also adopted the optimization of  $J_{in}^{(N)}/\lambda$  in the interpretations of their model results, the growth rate dependence of fermentation flux was derived before the growth rate optimization. In fact, Eqs. S29 and S137 in our model present a very similar form to that of Basan *et al.*<sup>10</sup>. Below, we list the critical differences. In Eq. S29, by regarding  $J_r^{(E)}$  and  $J_f^{(E)}$  as the two variables in quadratic equations, we have the following expression:

$$\begin{cases} J_r^{(E)} = \frac{\phi_{\max} - (\psi + \varphi/\varepsilon_f) \cdot \lambda}{1/\varepsilon_r - 1/\varepsilon_f}, \\ J_f^{(E)} = \frac{(\psi + \varphi/\varepsilon_r) \cdot \lambda - \phi_{\max}}{1/\varepsilon_r - 1/\varepsilon_f}. \end{cases} \quad (S138)$$

In Basan *et al.*<sup>10</sup>, Eq. S138 is regarded as the relationships between  $J_{r/f}^{(E)}$  and  $\lambda$  upon nutrient (and thus  $J_{in}^{(N)}$ ) perturbations, while  $\varepsilon_r$  and  $\varepsilon_f$  are deemed as constants through the perturbations. By contrast, in our model, Eq. S138 is the constraint for a given nutrient condition with fixed  $\kappa_A$ , yet not relevant for nutrient perturbations. For wild type strains, suppose that  $\varepsilon_r(\kappa_A) > \varepsilon_f(\kappa_A)$  (or vis versa), then, the optimal solution is  $J_r^{(E)}(\kappa_A) = \varphi \cdot \lambda(\kappa_A)$  and  $J_f^{(E)}(\kappa_A) = 0$ , with  $\lambda(\kappa_A) = \frac{\varepsilon_r(\kappa_A) \cdot \phi_{\max}}{\varphi + \varepsilon_r(\kappa_A) \cdot \psi(\kappa_A)}$ . Basically, this solution (which satisfies Eq. S138) corresponds to a point rather than a line in the relations between  $J_{r/f}^{(E)}$  and  $\lambda$  upon  $\kappa_A$  perturbations.

#### S6.4 The explanation for the Warburg effect in tumor cells

Overflow metabolism was originally found in tumor cells by Otto Warburg in 1920s<sup>33,34</sup>, known as the celebrated Warburg effect<sup>9,35</sup>. Our model and analysis shown in Sec. 2 can be naturally extended to explain the Warburg effect in tumor cell metabolism with the following modifications in the model settings. In the applications for tumor cell metabolism, the fermentation flux changes from acetate secretion rate into the lactate secretion rate, and thus the stoichiometric coefficients ( $\beta_i$ ) for ATP production change accordingly. Consequently, in the coarse-grained model shown in Fig. 1b,  $M_3$  stands for pyruvate, and  $\beta_2, \beta_6$  change into  $\beta_2 = 1, \beta_6 = -2$ .

Evidently, Eqs. S37-S38 still hold. As long as  $\varepsilon_r(\kappa_A^{\max}) < \varepsilon_f(\kappa_A^{\max})$  (Eq. S40), then, there exists a critical switching point for  $\kappa_A$  (denoted as  $\kappa_A^{(C)}$ , see Eq. S41), below which the respiration pathway is more efficient, while above  $\kappa_A^{(C)}$ , the fermentation pathway is more efficient in the proteome energy production. To maximize proliferation rate, the tumor cells would preferentially use the respiration pathway upon starvation while use the aerobic glycolysis pathway with abundant nutrient (Warburg effect). Based on the facts that the rate of glucose metabolism is 10-100 times faster in aerobic glycolysis than that of respiration<sup>35</sup>, and oncogenes induce Warburg effect intrinsically to promote cell proliferation<sup>35,36</sup>, it is suggested that  $\varepsilon_r(\kappa_A^{\max}) < \varepsilon_f(\kappa_A^{\max})$ . Thus, the aerobic glycolysis with abundant nutrients provides a fitness advantage for tumor cell proliferation.

## S7 Probability density functions of the variables and parameters

### S7.1 Probability density functions of $\kappa_i$

Enzyme catalysis is crucial for the survival of living organisms, which can significantly accelerate the rate of a biochemical reaction by moderating the energy barrier between the substrate and product<sup>3</sup>. However, the maximal turnover rate of enzymes,  $k_{\text{cat}}$  values, vary notably between the in vivo and in vitro measurements<sup>21</sup>. Recent studies suggest that differences in the aquatic medium should be the causes<sup>14,21</sup>.

In particular, the concentrations of metal ions such as potassium have a big influence on  $k_{\text{cat}}$ , which possess certain degree of variations among the cell populations under intracellular conditions<sup>14</sup>. For simplicity, we assume that the turnover rate of each  $E_i$  enzyme  $k_i^{\text{cat}}$  follows a Gaussian distribution  $\mathcal{N}(\mu_{k_i^{\text{cat}}}, \sigma_{k_i^{\text{cat}}}^2)$  with  $k_i^{\text{cat}} > 0$  among cells (extrinsic noise<sup>15</sup>, denoted as  $\eta_{\text{ext}}$ ), and then the probability density function of  $k_i^{\text{cat}}$  is given by

$$k_i^{\text{cat}} \sim \mathcal{N}'(x, \mu_{k_i^{\text{cat}}}, \sigma_{k_i^{\text{cat}}}^2) = \begin{cases} \frac{1}{\sigma_{k_i^{\text{cat}}} \sqrt{2\pi}} e^{-\frac{1}{2} \left( \frac{x - \mu_{k_i^{\text{cat}}}}{\sigma_{k_i^{\text{cat}}}^2} \right)^2}, & x \geq 0. \\ 0, & x < 0. \end{cases} \quad (\text{S139})$$

When the CV of the  $k_i^{\text{cat}}$  distribution  $\sigma_{k_i^{\text{cat}}} / \mu_{k_i^{\text{cat}}}$  is less than  $1/3$ ,  $\mathcal{N}'(x, \mu_{k_i^{\text{cat}}}, \sigma_{k_i^{\text{cat}}}^2)$  is almost identical to  $\mathcal{N}(\mu_{k_i^{\text{cat}}}, \sigma_{k_i^{\text{cat}}}^2)$ . In this regard,  $1/k_i^{\text{cat}}$  follows the positive inverse of Gaussian distribution (IOG), and the probability density function is:

$$\text{IOG}\left(x, \mu_{1/k_i^{\text{cat}}}, \zeta_{1/k_i^{\text{cat}}}\right) = \begin{cases} \sqrt{\frac{\zeta_{1/k_i^{\text{cat}}}}{2\pi x^4}} \exp\left(-\frac{1}{2} \frac{\zeta_{1/k_i^{\text{cat}}} (x - \mu_{1/k_i^{\text{cat}}})^2}{x^2 \mu_{1/k_i^{\text{cat}}}^2}\right), & x \geq 0, \\ 0, & x < 0, \end{cases} \quad (\text{S140})$$

where  $\zeta_{1/k_i^{\text{cat}}} = 1/\sigma_{k_i^{\text{cat}}}^2$  and  $\mu_{1/k_i^{\text{cat}}} = 1/\mu_{k_i^{\text{cat}}}$ . Meanwhile, due to the stochasticity of biochemical reactions, we apply Gillespie's chemical Langevin equation<sup>37</sup> to account for the intrinsic noise<sup>15</sup> (denoted as  $\eta_{\text{int}}$ ). For cell size regulation of *E. coli* within a cell cycle, the cell mass at initiation of DNA per chromosome origin remains constant<sup>38</sup>. Thus, the duration of enzyme  $E_i$  to finish a catalytic job (with a timescale of  $1/k_i^{\text{cat}}$ ) can be approximated as the first passage time of a stochastic process with

$$\begin{cases} X_i(t=0) = 0, \\ dX_i/dt = \alpha_i + \sqrt{\alpha_i} \Gamma_i(t), \\ T_\Theta = \inf \{t > 0 \mid X_i(t) = \Theta\}. \end{cases} \quad (\text{S141})$$

Here  $\alpha_i \equiv k_i^{\text{cat}} \cdot \Theta$ ,  $\Theta$  is proportional to the cell volume, and  $\Gamma_i(t)$  is the independent temporally uncorrelated Gaussian white noise. Then, for a given value of  $k_i^{\text{cat}}$ , the first passage time  $T_\Theta$  follows an Inverse Gaussian distribution (IG)<sup>39</sup>:

$$\text{IG}\left(x, \mu'_{1/k_i^{\text{cat}}}, \zeta'_{1/k_i^{\text{cat}}}\right) = \begin{cases} \sqrt{\frac{\zeta'_{1/k_i^{\text{cat}}}}{2\pi x^3}} \exp\left(-\frac{1}{2} \frac{\zeta'_{1/k_i^{\text{cat}}} (x - \mu'_{1/k_i^{\text{cat}}})^2}{x \mu'_{1/k_i^{\text{cat}}}^2}\right), & x \geq 0, \\ 0, & x < 0, \end{cases} \quad (\text{S142})$$

where  $\mu'_{1/k_i^{\text{cat}}} = 1/k_i^{\text{cat}}$ ,  $\zeta'_{1/k_i^{\text{cat}}} = \Theta/k_i^{\text{cat}}$ , and the variance  $\sigma'^2_{1/k_i^{\text{cat}}} \equiv \mu'^3_{1/k_i^{\text{cat}}} / \zeta'_{1/k_i^{\text{cat}}} = 1/\left[\Theta \cdot (k_i^{\text{cat}})^2\right]$ . Thus, we can obtain the CV:

$$\sigma'_{1/k_i^{\text{cat}}} / \mu'_{1/k_i^{\text{cat}}} = \Theta^{-\frac{1}{2}}, \quad (\text{S143})$$

which is inversely scaled with the square root of cell volume. Evidently, the intrinsic and extrinsic noise make orthogonal contributions to the total noise<sup>15</sup> (denoted as  $\eta_{\text{tot}}$ ), i.e.,

$$\eta_{\text{tot}}^2 = \eta_{\text{int}}^2 + \eta_{\text{ext}}^2. \quad (\text{S144})$$

In fact, when the CV is small (i.e.,  $\text{CV} \ll 1$ ), both IOG and IG distributions converge into Gaussian distributions (Fig. S9). In the back-of-the-envelope calculations, we approximate  $x$  in all the denominator

terms of  $\text{IOG}(x, \mu, \zeta)$  and  $\text{IG}(x, \mu, \zeta)$  as  $\mu$  (since  $\text{CV} \ll 1$ ). Then, both IOG and IG distributions can be approximated as follows:

$$\text{IOG}\left(x, \mu_{1/k_i^{\text{cat}}}, \zeta_{1/k_i^{\text{cat}}}\right) \xrightarrow{\text{CV} \ll 1} \mathcal{N}\left(\mu_{1/k_i^{\text{cat}}}, \sigma_{1/k_i^{\text{cat}}}^2\right), \quad (\text{S145})$$

with  $\sigma_{1/k_i^{\text{cat}}}^2 = \mu_{1/k_i^{\text{cat}}}^4 / \zeta_{1/k_i^{\text{cat}}}$ , and

$$\text{IG}\left(x, \mu'_{1/k_i^{\text{cat}}}, \zeta'_{1/k_i^{\text{cat}}}\right) \xrightarrow{\text{CV} \ll 1} \mathcal{N}\left(\mu'_{1/k_i^{\text{cat}}}, \sigma'^2_{1/k_i^{\text{cat}}}\right), \quad (\text{S146})$$

with  $\sigma'^2_{1/k_i^{\text{cat}}} = \mu'^3_{1/k_i^{\text{cat}}} / \zeta'_{1/k_i^{\text{cat}}}$ . Rigorously, we show it below that  $\text{IG}(x, \mu, \zeta)$  shrinks to be  $\mathcal{N}(\mu, \mu^3 / \zeta)$  when the CV is small. Here, the characteristic function of the variable is<sup>39,40</sup>

$$G(k) = \int_{-\infty}^{\infty} e^{ikx} \cdot \text{IG}(x, \mu, \zeta) dx = \exp \left\{ \frac{\zeta}{\mu} \left[ 1 - \sqrt{1 - \frac{2i\mu^2 k}{\zeta}} \right] \right\}, \quad (\text{S147})$$

and thus,

$$\text{IG}(x, \mu, \zeta) = \frac{1}{2\pi} \int_{-\infty}^{\infty} e^{-ikx} \cdot G(k) dk. \quad (\text{S148})$$

When the variance  $\sigma^2 \equiv \mu^3 / \zeta$  is very small, basically, we require  $2\mu^2 k / \zeta = 2\sigma^2 k / \mu \ll 1$ , and then  $\sqrt{1 - \frac{2i\mu^2 k}{\zeta}} \approx 1 - \frac{\mu^2}{\zeta} ki + \frac{\mu^4}{2\zeta^2} k^2$ . Thus,

$$\begin{cases} G(k) \approx \exp \left( \mu ki - \frac{\mu^3}{2\zeta} k^2 \right), \\ \text{IG}(x, \mu, \zeta) \approx \sqrt{\frac{\zeta}{2\pi\mu^3}} e^{-\frac{\zeta(x-\mu)^2}{2\mu^3}} = \mathcal{N}(\mu, \mu^3 / \zeta). \end{cases} \quad (\text{S149})$$

Then, we have

$$\lim_{\sigma \rightarrow 0} \text{IG}(x, \mu, \zeta) = \mathcal{N}(\mu, \mu^3 / \zeta). \quad (\text{S150})$$

In fact, for cell population growth in a long term, the contribution of the intrinsic noise becomes negligible. Thus,  $\eta_{\text{tot}} \approx \eta_{\text{ext}}$ . Combined with Eqs.S146-S147, it is easy to check that  $1/k_i^{\text{cat}}$  shares roughly identical CV as  $k_i^{\text{cat}}$ :

$$\sigma_{1/k_i^{\text{cat}}} / \mu_{1/k_i^{\text{cat}}} = \sigma_{k_i^{\text{cat}}} / \mu_{k_i^{\text{cat}}} . \quad (\text{S151})$$

For convenience, in the model analysis, we approximate both IOG and IG distributions as Gaussian distributions. Then, all  $1/k_i^{\text{cat}}$  are normally distributed independent random variables following Gaussian distributions:

$$1/k_i^{\text{cat}} \sim \mathcal{N}(\mu_{1/k_i^{\text{cat}}}, \sigma_{1/k_i^{\text{cat}}}^2) . \quad (\text{S152})$$

Using the properties of Gaussian distributions, for a series of constant real numbers  $\gamma_i$ , the summation of  $\gamma_i/k_i^{\text{cat}}$ , where we defined it as  $\Xi \equiv \sum_{i=1}^n \gamma_i/k_i^{\text{cat}}$ , follows a Gaussian distribution<sup>40</sup>:

$$\Xi \sim \mathcal{N}(\mu_{\Xi}, \sigma_{\Xi}^2) , \quad (\text{S153})$$

with  $\mu_{\Xi} = \sum_{i=1}^n \gamma_i \mu_{1/k_i^{\text{cat}}}$  and  $\sigma_{\Xi}^2 = \sum_{i=1}^n (\gamma_i \sigma_{1/k_i^{\text{cat}}})^2$ . The relationship between  $\kappa_i$  and  $k_i^{\text{cat}}$  is shown in Eq. S12. To optimize growth rate, each  $\kappa_i$  of the intermediate nodes satisfies Eq. S20, while  $\kappa_A$  satisfies Eq. S27. Thus, for a given nutrient environment ( $[A]$  is fixed), all the ratios  $k_i^{\text{cat}}/\kappa_i$  are constants. Combined with Eqs. S139, S145-S146, S152, then, the distributions of all  $\kappa_i$  and  $1/\kappa_i$  can be approximated as Gaussian distributions:

$$\begin{cases} \kappa_i \sim \mathcal{N}(\mu_{\kappa_i}, \sigma_{\kappa_i}^2), \\ 1/\kappa_i \sim \mathcal{N}(\mu_{1/\kappa_i}, \sigma_{1/\kappa_i}^2), \end{cases} \quad (\text{S154})$$

where  $\mu_{\kappa_i}$  and  $\mu_{1/\kappa_i}$  represent the mean, while  $\sigma_{\kappa_i}$  and  $\sigma_{1/\kappa_i}$  represent the standard deviations. Using the properties of Gaussian distributions combined with Eq. S31, S32, S36, S42-S43, S145-S146 and S153, then  $\varepsilon_r$ ,  $\varepsilon_f$ ,  $\psi$ ,  $\lambda_r$ ,  $\lambda_f$ ,  $\kappa_A^{(C)}$  and  $\lambda_c$  also roughly follow Gaussian distributions.

## S7.2 Probability density function of the growth rate $\lambda$

From Sec. 7.1, we note that  $\lambda_r$  and  $\lambda_f$  (see Eq. S36) roughly follow Gaussian distributions, with

$$\begin{cases} \lambda_r \sim \mathcal{N}(\mu_{\lambda_r}, \sigma_{\lambda_r}^2), \\ \lambda_f \sim \mathcal{N}(\mu_{\lambda_f}, \sigma_{\lambda_f}^2), \end{cases} \quad (\text{S155})$$

where  $\mu_{\lambda_{rf}}$  and  $\sigma_{\lambda_{rf}}$  represent the mean and the standard deviations, respectively. We further assume that the correlation between  $\lambda_r$  and  $\lambda_f$  is  $\rho_{rf}$ . From Eq. S36, the growth rate  $\lambda$  takes the maximum value of  $\lambda_r$  and  $\lambda_f$ , i.e.,

$$\lambda = \max(\lambda_r, \lambda_f). \quad (\text{S156})$$

Then, the cumulative distribution function of  $\lambda$  is  $P(\lambda \leq x) = \int_{-\infty}^x \int_{-\infty}^x f(x_1, x_2) dx_1 dx_2$ , where

$$f(x_1, x_2) = \frac{(1 - \rho_{rf}^2)^{-\frac{1}{2}}}{2\pi\sigma_{\lambda_r}\sigma_{\lambda_f}} \exp\left(-\frac{1}{2(1 - \rho_{rf}^2)} \left[ \left( \frac{x_1 - \mu_{\lambda_r}}{\sigma_{\lambda_r}} \right)^2 - 2\rho_{rf} \left( \frac{x_1 - \mu_{\lambda_r}}{\sigma_{\lambda_r}} \right) \left( \frac{x_2 - \mu_{\lambda_f}}{\sigma_{\lambda_f}} \right) + \left( \frac{x_2 - \mu_{\lambda_f}}{\sigma_{\lambda_f}} \right)^2 \right]\right). \quad \text{Thus, the probability density function of the growth rate } \lambda \text{ is}$$

$$f_\lambda(x) = \frac{1}{2\sqrt{2\pi}\sigma_{\lambda_r}} e^{-\frac{1}{2}\left(\frac{x-\mu_{\lambda_r}}{\sigma_{\lambda_r}}\right)^2} \left[ \text{erf}\left(\frac{(x-\mu_{\lambda_r})\sigma_{\lambda_r} - \rho_{rf}\sigma_{\lambda_f}(x-\mu_{\lambda_f})}{\sigma_{\lambda_r}\sigma_{\lambda_f}\sqrt{2(1-\rho_{rf}^2)}}\right) + 1 \right] + \frac{1}{2\sqrt{2\pi}\sigma_{\lambda_f}} e^{-\frac{1}{2}\left(\frac{x-\mu_{\lambda_f}}{\sigma_{\lambda_f}}\right)^2} \left[ \text{erf}\left(\frac{(x-\mu_{\lambda_f})\sigma_{\lambda_f} - \rho_{rf}\sigma_{\lambda_r}(x-\mu_{\lambda_r})}{\sigma_{\lambda_r}\sigma_{\lambda_f}\sqrt{2(1-\rho_{rf}^2)}}\right) + 1 \right]. \quad (\text{S157})$$

In Fig. S3b, we show that Eq. S157 quantitatively illustrate the experimental data of *E. coli* under the relevant conditions.

## S8 Model comparisons with experiments

### S8.1 Fluxes comparisons with experiments

In Sec. 6.2, we see that the values of  $J_f^{(\text{N})}$  and  $J_r^{(\text{N})}$  are required to calculate the in vivo enzyme catalytic rates of the intermediate nodes. Here, we use  $J_{\text{ac}}$  and  $J_{\text{CO}_2,r}$  to represent the stoichiometric fluxes of acetate from fermentation pathway and  $\text{CO}_2$  from respiration pathway, respectively. Combined with the stoichiometric coefficients of both pathways, we have

$$\begin{cases} J_{\text{ac}} = J_f, \\ J_{\text{CO}_2,r} = 3 \cdot J_r. \end{cases} \quad (\text{S158})$$

By further combining with Eqs. S16-S17, and then,

$$\begin{cases} J_f^{(\text{N})} = J_{\text{ac}} \cdot \frac{m_{\text{carbon}}}{M_{\text{carbon}}} \cdot \left[ \sum_i r_i / N_{\text{EP}_i}^{\text{carbon}} \right]^{-1}, \\ J_r^{(\text{N})} = \frac{1}{3} \cdot J_{\text{CO}_2,r} \cdot \frac{m_{\text{carbon}}}{M_{\text{carbon}}} \cdot \left[ \sum_i r_i / N_{\text{EP}_i}^{\text{carbon}} \right]^{-1}. \end{cases} \quad (\text{S159})$$

In fact, the values of  $J_{ac}$  and  $J_{CO_2,r}$  scale with the mass of the “big cell”, which increase with time. In experiments, the corresponding measurable fluxes,  $J_{ac}^{(N)}$  and  $J_{CO_2,r}^{(N)}$ , generally come with the unit of mM/OD<sub>600</sub>/h<sup>10</sup>. For *E. coli*, we use the following biochemical data collected from published literatures: 1 OD<sub>600</sub> roughly corresponds to  $6 \times 10^8$  cells/mL<sup>41</sup>, the average mass of a cell is 1pg<sup>42</sup>, the biomass percentage of the cell weight is 30%<sup>7</sup>, the molar mass of carbon is 12g<sup>3</sup>,  $r_{carbon} = 0.48$ <sup>7</sup> and  $r_{protein} = 0.55$ <sup>7</sup>. Combined with the values of  $r_i$  (see Sec.1.2) and  $N_{EP_i}^{carbon}$ , where  $N_{EP_{a1}}^{carbon} = 6$ ,  $N_{EP_{a2}}^{carbon} = 3$ ,  $N_{EP_b}^{carbon} = 3$ ,  $N_{EP_c}^{carbon} = 5$ , and  $N_{EP_d}^{carbon} = 4$ <sup>3</sup>, we have

$$\begin{cases} J_f^{(N)} \approx J_{ac}^{(N)} / 2, \\ J_r^{(N)} \approx J_{CO_2,r}^{(N)} / 6. \end{cases} \quad (S160)$$

From Eq. S18, we obtain the values of  $\eta_i$  for each precursor pool :  $\eta_{a1} = 0.15$ ,  $\eta_{a2} = 0.30$ ,  $\eta_b = 0.35$ ,  $\eta_c = 0.09$ ,  $\eta_d = 0.11$ . Still, the value of  $\eta_E$  is required to compare the growth rate-flux relations with experiments, and we specify the model parameter settings in Sec. 8.2.

## S8.2 Model parameter settings using experimental data

To compare with experiments, we collect biochemical data of *E. coli* shown in Table S1-S2 to set the model parameters. Basically, the molecular weight (MW) and in vitro  $k_{cat}$  values of the catalytic enzymes, and the proteome and flux data used to calculate the in vivo turnover numbers. To reduce the measurement noise, we take the average rather than the maximum value of in vivo  $k_{cat}$  from calculations with data from four cultures (Table S2). Here, we prioritize the use of in vivo  $k_{cat}$  wherever applicable unless there is a vacancy (Table S1).

Note that our models are coarse grained, e.g., the flux  $J_3$  shown in Fig. 1b actually corresponds to three different reactions in the metabolic network (see Fig.1a and Table S1), where we label them as  $J_3^{(i)}$  ( $i=1,2,3$ ). For each  $J_3^{(i)}$ , there are corresponding variables/parameters of  $\Phi_3^{(i)}$ ,  $\xi_3^{(i)}$ ,  $\phi_3^{(i)}$ ,  $\kappa_3^{(i)}$  satisfying Eqs. S8, S9 and S12, Evidently,  $J_3^{(i)} = J_3$  ( $i=1,2,3$ ), and it is easy to get the following relationship between  $\kappa_3^{(i)}$  and  $\kappa_3$ :

$$1/\kappa_3 = \sum_{i=1}^3 1/\kappa_3^{(i)} \quad . \quad (S161)$$

In fact, Eq. S161 can be generalize to determine the values of other  $\kappa_i$  in the coarse-grained models combined with the biochemical data. For the coarse-grained model of Group A carbon source utilization

shown in Fig. 1b, we have the values for parameters  $\kappa_i$  ( $i=1, \dots, 6$ ), and then  $\varepsilon_{r/f}(\kappa_A^{(C)}) = 122 \text{ (h}^{-1}\text{)}$ .

Evidently,  $\varepsilon_r(\kappa_{\text{glucose}}^{(\text{ST})}) < \varepsilon_f(\kappa_{\text{glucose}}^{(\text{ST})})$ ,  $\varepsilon_r(\kappa_{\text{lactose}}^{(\text{ST})}) < \varepsilon_f(\kappa_{\text{lactose}}^{(\text{ST})})$ , and thus  $\varepsilon_r(\kappa_A^{\text{max}}) < \varepsilon_f(\kappa_A^{\text{max}})$ . For

pyruvate, we have  $\varepsilon_{r/f}^{(\text{py})}(\kappa_{\text{py}}^{(\text{C})}) = \varepsilon_{r/f}(\kappa_A^{(\text{C})}) = 122 \text{ (h}^{-1}\text{)}$  (see Eqs. S43 and S101), and it is easy to check

that  $\varepsilon_r(\kappa_{\text{py}}^{(\text{ST})}) < \varepsilon_f(\kappa_{\text{py}}^{(\text{ST})})$ .

For the remaining model parameters, note that we have classified the inactive ribosomal-affiliated proteins into Q-class, then  $\phi_{\text{max}} = 48\%$ <sup>1</sup>. The values of  $\kappa_t$  is obtainable from experiments: the translational speed is  $20.1 \text{ aa/s}^1$ , and there are 7336 amino acids per ribosome<sup>2</sup>, with  $\zeta \approx 1.67$ <sup>1,2</sup>(Sec. 1.1), then,  $\kappa_t = 1/610 \text{ (s}^{-1}\text{)}$ . However, there are insufficient data to determine the values of  $\kappa_i$  ( $i=a1, a2, b, c, d$ ) from the entry point metabolites to the precursor pools. Basically, it involves a lot of steps, and thus these values should be considerably large. Here, we lump sum the contributions of  $\kappa_t$  and  $\kappa_i$  ( $i=a1, a2, b, c, d$ ) by defining a composed parameter:

$$\Omega \equiv 1/\kappa_t + \sum_i^{a1, a2, b, c, d} \eta_i/\kappa_i. \quad (\text{S162})$$

Then, we proceed to estimate the values of  $\Omega$  and  $\varphi$  using the  $J_{\text{ac}}^{(\text{N})}$ - $\lambda$  experimental data of the wild type strain (Fig. 1c), and thus, all the rest of model parameters are set accordingly.

For the case of  $w_0 = 0 \text{ (h}^{-1}\text{)}$ , where all  $k_{\text{cat}}$  values follow a Gaussian form extrinsic noise with a CV of 25%, which is the general setting we use unless otherwise specified, then  $\varphi = 10.8$  and  $\Omega = 1345 \text{ (s)}$ . Accordingly, we have  $\eta_E = 14.78$ ,  $\mu_{\lambda_c} = 0.92 \text{ (h}^{-1}\text{)}$ , and  $\sigma_{\lambda_c} = 0.12 \mu_{\lambda_c}$ , where the noisy extent of  $\Omega$  is estimated with the average CV of other  $\kappa_i$ . For the translation inhibition effect of Cm, we estimate the values for  $\iota$  as  $\iota_{w_0=0}^{(2\mu\text{m Cm})} = 1.15$ ,  $\iota_{w_0=0}^{(4\mu\text{m Cm})} = 2.33$ ,  $\iota_{w_0=0}^{(8\mu\text{m Cm})} = 6.25$ , where the superscript stands for the concentrations of Cm, and the subscript represents our choice of  $w_0$ .

For pyruvate, with the value of  $\eta_E$ , we get  $\varphi_{\text{py}} = 14.82$ . However, we are still lack of the proteome data to determine the value of  $\kappa_9$ , which actually involves a lot of steps in the metabolic network and thus can be considerably large. Here we define another composed parameter  $\Omega'_{\text{Gg}} \equiv (\eta_b + \eta_c)/\kappa_8 + \eta_{a1}/\kappa_9$ , and estimate its value as  $\Omega'_{\text{Gg}} = 690 \text{ (s)}$ , where the subscript “Gg” stands for glucogenesis. Then,  $\mu_{\lambda_c^{(\text{py})}} = 0.67 \text{ (h}^{-1}\text{)}$ , and  $\sigma_{\lambda_c^{(\text{py})}} = 0.10 \mu_{\lambda_c^{(\text{py})}}$ , where the same noisy extent of  $\Omega$  is applied on  $\Omega'_{\text{Gg}}$ .

For the case that a Group A carbon source mixed with 21 amino acids (21AA, with saturated concentration), then  $\varphi_{21AA} = 14.2$ . Comparing Eq. S32 with Eq. S112, the parameter  $\Omega$  should change

into  $\Omega_{21AA} \equiv 1/\kappa_t + \eta_{a1}/\kappa_{a1} + \sum_i^{a2,b,c,d} \eta_i/\kappa_i^{(21AA)}$ . Evidently,  $1/\kappa_t < \Omega_{21AA} < \Omega$ , and we estimate

$\Omega_{21AA} = 1000$  (s) with the mean value of growth rate data. Then, we have  $\mu_{\lambda_c^{(21AA)}} = 1.13$  (h<sup>-1</sup>), and  $\sigma_{\lambda_c^{(21AA)}} = 0.12\mu_{\lambda_c^{(21AA)}}$ .

For the case that a Group A carbon source mixed with 7 amino acids (7AA: His, Iso, Leu, Lys, Met, Phe, and Val), similar to the roles of  $\varphi_{21AA}$  and  $\Omega_{21AA}$ , we define  $\varphi_{7AA}$  and  $\Omega_{7AA}$ . Using the mass fraction of the 7AA combining with Eq. S18, we have  $\varphi_{7AA} = 11.6$ . For the value of  $\Omega_{7AA}$ , evidently,  $\Omega_{21AA} < \Omega_{7AA} < \Omega$ , and we estimate  $\Omega_{7AA} = 1215$  (s) with the growth rate data. Then,  $\mu_{\lambda_c^{(7AA)}} = 0.98$  (h<sup>-1</sup>), and  $\sigma_{\lambda_c^{(21AA)}} = 0.12\mu_{\lambda_c^{(21AA)}}$ .

For the case of  $w_0 = 2.5$  (h<sup>-1</sup>), we have  $\varphi = 8.3$ , and thus  $\eta_E = 12.28$ , while other parameters such as  $\Omega$ ,  $\mu_{\lambda_c}$  and  $\sigma_{\lambda_c}$  remain the same values as that of  $w_0 = 0$ . Nevertheless, the values for  $t$  upon translation inhibition with Cm are influenced by the choice of  $w_0$ , where the values of  $t$  change into  $t_{w_0=2.5}^{(2\mu\text{m Cm})} = 1.05$ ,  $t_{w_0=2.5}^{(4\mu\text{m Cm})} = 2.00$ ,  $t_{w_0=2.5}^{(8\mu\text{m Cm})} = 5.40$ .

From Sec. 7.1-7.2, combined with Eq. S114, the distributions of  $\lambda_r^{(21AA)}$  and  $\lambda_f^{(21AA)}$  can be approximated by Gaussian distributions:

$$\begin{cases} \lambda_r^{(21AA)} \sim \mathcal{N}\left(\mu_{\lambda_r^{(21AA)}}, \sigma_{\lambda_r^{(21AA)}}^2\right), \\ \lambda_f^{(21AA)} \sim \mathcal{N}\left(\mu_{\lambda_f^{(21AA)}}, \sigma_{\lambda_f^{(21AA)}}^2\right), \end{cases} \quad (S163)$$

where  $\mu_{\lambda_r^{(21AA)}}$  and  $\mu_{\lambda_f^{(21AA)}}$  stand for the mean values, while  $\sigma_{\lambda_r^{(21AA)}}$  and  $\sigma_{\lambda_f^{(21AA)}}$  represent the standard deviations. For the case of glucose mixed with 21AA (labeled as “Glucose+21AA”), the distribution of the growth rate  $\lambda_{\text{glucose}}^{(21AA)}$  follows Eq. S157. With  $\Omega_{21AA} = 1000$  (s), we have  $\mu_{\lambda_{\text{glucose},r}^{(21AA)}} = 1.34$  (h<sup>-1</sup>),  $\mu_{\lambda_{\text{glucose},f}^{(21AA)}} = 1.46$  (h<sup>-1</sup>) (both definitions follow Eq. S163), and  $\rho_{rf} \approx 1.0$  (obtained with numerical results).

For the case of succinate mixed with 21AA (labeled as “Succinate+21AA”), the respiration pathway is always more efficient since succinate lies within the TCA cycle, then the cell growth rate (defined as  $\lambda_{\text{succinate}}^{(21AA)}$ ) would just take the value of the respiration one and thus follows a Gaussian distribution:

$$\lambda_{\text{succinate}}^{(21\text{AA})} \sim \mathcal{N}\left(\mu_{\lambda_{\text{succinate}}^{(21\text{AA})}}, \sigma_{\lambda_{\text{succinate}}^{(21\text{AA})}}^2\right). \quad (\text{S164})$$

For the case that acetate is the sole carbon source, evidently, the cells only use the respiration pathway, and thus the growth rate (defined as  $\lambda_{\text{actate}}$ ) follows a Gaussian distribution:

$$\lambda_{\text{actate}} \sim \mathcal{N}\left(\mu_{\lambda_{\text{actate}}}, \sigma_{\lambda_{\text{actate}}}^2\right). \quad (\text{S165})$$

With the grow rate data, we estimate  $\mu_{\lambda_{\text{succinate}}^{(21\text{AA})}} = 0.67 \text{ (h}^{-1}\text{)}$  and  $\mu_{\lambda_{\text{actate}}} = 0.253 \text{ (h}^{-1}\text{)}$ . To illustrate the distributions of growth rate  $\lambda_{\text{glucose}}^{(21\text{AA})}$ ,  $\lambda_{\text{succinate}}^{(21\text{AA})}$  and  $\lambda_{\text{actate}}$  shown in Fig. S3b, were there no measurement noise, extrinsic noise with a CV of 40% is required for every  $k_{\text{cat}}$  value. Then,  $\sigma_{\lambda_{\text{glucose},r}^{(21\text{AA})}} \approx 0.21\mu_{\lambda_{\text{glucose},r}^{(21\text{AA})}}$ ,  $\sigma_{\lambda_{\text{glucose},f}^{(21\text{AA})}} \approx 0.23\mu_{\lambda_{\text{glucose},f}^{(21\text{AA})}}$ ,  $\sigma_{\lambda_{\text{succinate}}^{(21\text{AA})}} = 0.22\mu_{\lambda_{\text{succinate}}^{(21\text{AA})}}$ , and  $\sigma_{\lambda_{\text{actate}}} = 0.22\mu_{\lambda_{\text{actate}}}$ . Allowing for the measurement noise, we still use extrinsic noise with a CV of 25% other for those shown in Fig. S3b.

### S8.3 Notes on the applications of the reference data

**Data calibrations:** We use experimental data of the original references throughout our manuscript other for two calibrations. The first calibration is shown in the footnote of Table S2. With this calibration, the  $J_{\text{ac}}^{(\text{N})}\text{-}\lambda$  data<sup>10</sup> in Table S2 align to the same curve as that of Fig. 1c. The second calibration is for the data shown in Figs. 3f and 1c (chemostat data). The unit in the original reference<sup>13</sup> is mmol/(dry mass)g/h, to convert it into the unit we applied in our text, mM/OD<sub>600</sub>/h, the conversion factor should be 0.18. Here, to calibrate with other experimental results, we deduce that only 60% of the measured dry biomass in centrifuged material is effective. Then, there is a calibration factor of 0.6, and the conversion factor changes into 0.3.

**Data of the inducible strains:** We note that part of the experiment data in the original references<sup>10,17</sup> were obtained using strains with titratable systems (e.g. titratable ptsG, LacY). Basically, the  $J_{\text{ac}}^{(\text{N})}\text{-}\lambda$  relation of these inducible strains align to the same curve as that of the wild type *E.coli* (Fig. 1c). Given that evolution treatment is not involved for the inducible strain, we regard the titration perturbation as a technique to fool the strains. That is, these inducible strains behave as if they were cultured in a less efficient Group A carbon source.

**Experimental data sources:** The batch culture data shown in Figs. 1c (labeled with minimum/rich medium or inducible strain) and S3c were taken from the source data of the reference's figure 1<sup>10</sup>. The chemostat data shown in Figs. 1c were taken from the reference's table 7<sup>13</sup>. The data shown in Fig. 1d were taken from the reference's extended data figure 3a<sup>10</sup> with calibrations specified in the footnote of Table S2.

The data shown in Fig. 2a were adopted from the reference's extended data figure 4a-b<sup>10</sup>. The data shown in Fig. 2b were taken from the source data of the reference's figure 2a<sup>10</sup>. The data shown in Fig. 2c were taken from the source data of the reference's figure 3a<sup>10</sup>. The data shown in Fig. 3a-b were taken from the source data of the reference's figure 3d<sup>10</sup>.

The data shown in Figs. 3c-d and S4 were taken from the source data of the reference's figure 3c<sup>10</sup>. The data shown in Fig. 3f were taken from the reference's table 7<sup>13</sup>, with a calibration factor specified in the above paragraph ("Data calibrations").

The data shown in Figs.4a-b and S5 were taken from the reference's table S2 with label "C-lim"<sup>17</sup>, where we did not incorporate the reference's data with  $\lambda=0.45205$  (h<sup>-1</sup>) for there are other unconsidered factors involved during slow growth<sup>43</sup> (for  $\lambda<0.5$  h<sup>-1</sup>), and we speculate that there are might be unknown calibration factors. The data shown in Figs. 4c-d, S6-S7 were adopted from the reference's extended data figure 6-7<sup>10</sup>.

The gene names shown in Fig. S1b were identified using KEGG database. The data shown S8b were drawn from Table S1, which includes the original references itself. The flux data shown in Table S2 were taken from the reference's extended data figure 3a<sup>10</sup> with calibrations specified in the footnote. The proteome data shown in Table S2 were taken from the reference's supplementary Table N5<sup>10</sup>.

## Supplementary References

- 1 Scott, M., Gunderson, C. W., Mateescu, E. M., Zhang, Z. & Hwa, T. Interdependence of cell growth and gene expression: origins and consequences. *Science* **330**, 1099-1102 (2010).
- 2 Neidhardt, F. C. *Escherichia coli and Salmonella: cellular and molecular biology*. (ASM Press, 1996).
- 3 Nelson, D. L., Lehninger, A. L. & Cox, M. M. *Lehninger principles of biochemistry*. (Macmillan, 2008).
- 4 Wang, X., Xia, K., Yang, X. & Tang, C. Growth strategy of microbes on mixed carbon sources. *Nature Communications* **10**, 1279 (2019).
- 5 Bennett, B. D. *et al.* Absolute metabolite concentrations and implied enzyme active site occupancy in *Escherichia coli*. *Nature Chemical Biology* **5**, 593-599 (2009).
- 6 Park, J. O. *et al.* Metabolite concentrations, fluxes and free energies imply efficient enzyme usage. *Nature Chemical Biology* **12**, 482-489 (2016).
- 7 Neidhardt, F. C., Ingraham, J. L. & Schaechter, M. *Physiology of the bacterial cell*. (Sinauer associates, 1990).
- 8 Sauer, U., Canonaco, F., Heri, S., Perrenoud, A. & Fischer, E. The soluble and membrane-bound transhydrogenases UdhA and PntAB have divergent functions in NADPH metabolism of *Escherichia coli*. *Journal of Biological Chemistry* **279**, 6613-6619 (2004).
- 9 Vander Heiden, M. G., Cantley, L. C. & Thompson, C. B. Understanding the Warburg effect: the metabolic requirements of cell proliferation. *Science* **324**, 1029-1033 (2009).
- 10 Basan, M. *et al.* Overflow metabolism in *Escherichia coli* results from efficient proteome allocation. *Nature* **528**, 99-104 (2015).
- 11 Molenaar, D., Van Berlo, R., De Ridder, D. & Teusink, B. Shifts in growth strategies reflect tradeoffs in cellular economics. *Molecular Systems Biology* **5**, 323 (2009).
- 12 Chen, Y. & Nielsen, J. Energy metabolism controls phenotypes by protein efficiency and allocation. *Proceedings of the National Academy of Sciences* **116**, 17592-17597 (2019).
- 13 Holms, H. Flux analysis and control of the central metabolic pathways in *Escherichia coli*. *FEMS Microbiology Reviews* **19**, 85-116 (1996).
- 14 García-Contreras, R., Vos, P., Westerhoff, H. V. & Boogerd, F. C. Why *in vivo* may not equal *in vitro*—new effectors revealed by measurement of enzymatic activities under the same *in vivo*-like assay conditions. *The FEBS Journal* **279**, 4145-4159 (2012).
- 15 Elowitz, M. B., Levine, A. J., Siggia, E. D. & Swain, P. S. Stochastic gene expression in a single cell. *Science* **297**, 1183-1186 (2002).
- 16 Wallden, M., Fange, D., Lundius, E. G., Baltekin, Ö. & Elf, J. The synchronization of replication and division cycles in individual *E. coli* cells. *Cell* **166**, 729-739 (2016).
- 17 Hui, S. *et al.* Quantitative proteomic analysis reveals a simple strategy of global resource allocation in bacteria. *Molecular Systems Biology* **11**, 784 (2015).
- 18 Mori, M., Schink, S., Erickson, D. W., Gerland, U. & Hwa, T. Quantifying the benefit of a proteome reserve in fluctuating environments. *Nature Communications* **8**, 1225 (2017).
- 19 Basan, M. *et al.* A universal trade-off between growth and lag in fluctuating environments. *Nature* **584**, 470-474 (2020).
- 20 Kussell, E. & Leibler, S. Phenotypic diversity, population growth, and information in fluctuating environments. *Science* **309**, 2075-2078 (2005).

21 Davidi, D. *et al.* Global characterization of in vivo enzyme catalytic rates and their correspondence to in vitro kcat measurements. *Proceedings of the National Academy of Sciences* **113**, 3401-3406 (2016).

22 Nanchen, A., Schicker, A., Sauer, U. J. A. & microbiology, e. Nonlinear dependency of intracellular fluxes on growth rate in miniaturized continuous cultures of Escherichia coli. *Applied Environmental Microbiology* **72**, 1164-1172 (2006).

23 Meyer, H.-P., Leist, C. & Fiechter, A. Acetate formation in continuous culture of Escherichia coli K12 D1 on defined and complex media. *Journal of Biotechnology* **1**, 355-358 (1984).

24 Niebel, B., Leupold, S. & Heinemann, M. An upper limit on Gibbs energy dissipation governs cellular metabolism. *Nature Metabolism* **1**, 125-132 (2019).

25 Majewski, R. & Domach, M. Simple constrained-optimization view of acetate overflow in E. coli. *Biotechnology Bioengineering* **35**, 732-738 (1990).

26 Shlomi, T., Benyamin, T., Gottlieb, E., Sharan, R. & Ruppin, E. Genome-scale metabolic modeling elucidates the role of proliferative adaptation in causing the Warburg effect. *PLoS Computational Biology* **7**, e1002018 (2011).

27 Zhuang, K., Vemuri, G. N. & Mahadevan, R. Economics of membrane occupancy and respiro-fermentation. *Molecular Systems Biology* **7**, 500 (2011).

28 Varma, A. & Palsson, B. O. Stoichiometric flux balance models quantitatively predict growth and metabolic by-product secretion in wild-type Escherichia coli W3110. *Applied Environmental Microbiology* **60**, 3724-3731 (1994).

29 Dai, Z., Shestov, A. A., Lai, L. & Locasale, J. W. A flux balance of glucose metabolism clarifies the requirements of the Warburg effect. *Biophysical Journal* **111**, 1088-1100 (2016).

30 Sánchez, B. J. *et al.* Improving the phenotype predictions of a yeast genome-scale metabolic model by incorporating enzymatic constraints. *Molecular Systems Biology* **13**, 935 (2017).

31 Vazquez, A., Liu, J., Zhou, Y. & Oltvai, Z. N. Catabolic efficiency of aerobic glycolysis: the Warburg effect revisited. *BMC Systems Biology* **4**, 1-9 (2010).

32 Vazquez, A. & Oltvai, Z. N. Macromolecular crowding explains overflow metabolism in cells. *Scientific Reports* **6**, 31007 (2016).

33 Warburg, O., Posener, K. & Negelein, E. The metabolism of cancer cells. *Biochem. Zeitschrift* **152**, 319-344 (1924).

34 Warburg, O. The metabolism of carcinoma cells. *The Journal of Cancer Research* **9**, 148-163 (1925).

35 Liberti, M. V. & Locasale, J. W. The Warburg effect: how does it benefit cancer cells? *Trends in Biochemical Sciences* **41**, 211-218 (2016).

36 Hanahan, D. & Weinberg, R. A. Hallmarks of cancer: the next generation. *Cell* **144**, 646-674 (2011).

37 Gillespie, D. T. The chemical Langevin equation. *The Journal of Chemical Physics* **113**, 297-306 (2000).

38 Donachie, W. D. Relationship between cell size and time of initiation of DNA replication. *Nature* **219**, 1077-1079 (1968).

39 Folks, J. L. & Chhikara, R. S. The inverse Gaussian distribution and its statistical application—a review. *Journal of the Royal Statistical Society: Series B* **40**, 263-275 (1978).

40 Van Kampen, N. G. *Stochastic processes in physics and chemistry*. Vol. 1 (Elsevier, 1992).

41 Stevenson, K., McVey, A. F., Clark, I. B., Swain, P. S. & Pilizota, T. General calibration of  
microbial growth in microplate readers. *Scientific Reports* **6**, 1-7 (2016).

42 Milo, R. & Phillips, R. *Cell biology by the numbers*. (Garland Science, 2015).

43 Dai, X. *et al.* Reduction of translating ribosomes enables *Escherichia coli* to maintain elongation  
rates during slow growth. *Nature Microbiology* **2**, 1-9 (2016).

## Supplementary Tables

**Table S1. Molecular weight (MW) and in vivo/ in vitro  $k_{cat}$  data of *E. coli*.**

No. <sup>†</sup>	Reaction	Enzyme	Gene name	EC	MW (kDa)	In vitro $k_{cat}$ (s <sup>-1</sup> )	References	In vivo* $k_{cat}$ (s <sup>-1</sup> )	Chosen $k_{cat}$ (s <sup>-1</sup> )
<b>J<sub>1</sub></b>	Glucose-6P $\leftrightarrow$ Fructose-6P	Glucose-6-phosphate isomerase	pgi	EC:5.3.1.9	1.2×10 <sup>2</sup>	2.6×10 <sup>2</sup>	PMID: 7004378; DOI:10.1016/j.ijms.2004.09.017	8.7×10 <sup>2</sup>	8.7×10 <sup>2</sup>
	Fructose-6P $\rightarrow$ Fructose-1,6P	Phosphofructokinase	pfkA <sup>‡</sup>	EC:2.7.1.11	1.4×10 <sup>2</sup>	4.4×10 <sup>2</sup>	PMID: 6218375; 70226	1.7×10 <sup>3</sup>	1.7×10 <sup>3</sup>
	Fructose-1,6P $\leftrightarrow$ Glyceraldehyde 3-phosphate+Dihydroxy acetone phosphate	Fructose-bisphosphate aldolase	fbaA <sup>‡</sup>	EC:4.1.2.13	7.8×10	1.4×10	PMID: 8939754; 15531627	1.6×10 <sup>2</sup>	1.6×10 <sup>2</sup>
	Dihydroxyacetone phosphate $\leftrightarrow$ Glyceraldehyde 3-phosphate	Triosephosphate Isomerase	tpiA	EC:5.3.1.1	5.4×10	4.3×10 <sup>2</sup>	PMID: 3887397; 6092857	2.7×10 <sup>2</sup>	2.7×10 <sup>2</sup>
	Glyceraldehyde 3-phosphate $\leftrightarrow$ 1,3-Bisphosphoglycerate	Glyceraldehyde-3-phosphate dehydrogenase	gapA	EC:1.2.1.12	1.4×10 <sup>2</sup>	9.5×10	PMID: 4932978; 2200929	1.5×10 <sup>2</sup>	1.5×10 <sup>2</sup>
	1,3-Bisphosphoglycerate $\leftrightarrow$ 3-Phosphoglycerate	Phosphoglycerate kinase	pgk	EC:2.7.2.3	4.4×10	3.5×10 <sup>2</sup>	PMID: 367367; 166274	1.9×10 <sup>2</sup>	1.9×10 <sup>2</sup>
	3-Phosphoglycerate $\leftrightarrow$ 2-Phosphoglycerate	Phosphoglycerate mutase	gpmA <sup>‡</sup>	EC:5.4.2.11	4.9×10	3.3×10 <sup>2</sup>	PMID: 10437801	4.5×10 <sup>2</sup>	4.5×10 <sup>2</sup>
	2-Phosphoglycerate $\leftrightarrow$ Phosphoenolpyruvate	Enolase	eno	EC:4.2.1.11	9.0×10	2.2×10 <sup>2</sup>	PMID: 1094232; 4942326	1.7×10 <sup>2</sup>	1.7×10 <sup>2</sup>
<b>J<sub>2</sub></b>	Phosphoenolpyruvate $\rightarrow$ Pyruvate	Pyruvate kinase	pykF <sup>‡</sup>	EC:2.7.1.40	2.4×10 <sup>2</sup>	5.0×10 <sup>2</sup>	PMID: 6759852	1.6×10 <sup>3</sup>	1.6×10 <sup>3</sup>
	Pyruvate $\rightarrow$ Acetyl-CoA	Pyruvate dehydrogenase	aceE <sup>‡</sup>	EC:1.2.4.1	1.0×10 <sup>2</sup>	1.2×10 <sup>2</sup>	PMID: 23088422	3.4×10 <sup>2</sup>	3.4×10 <sup>2</sup>
<b>J<sub>3</sub></b>	Oxaloacetate +Acetyl-CoA $\rightarrow$ Citrate	Citrate synthase	gltA	EC:2.3.3.1	9.7×10	2.4×10 <sup>2</sup>	PMID: 4900996; 23954305	7.1×10	7.1×10
	Citrate $\leftrightarrow$ Isocitrate	Aconitate hydratase	acnB <sup>‡</sup>	EC:4.2.1.3	9.4×10	7.0×10	PMID: 15963579; 12473114	6.3×10	6.3×10
	Isocitrate $\rightarrow$ $\alpha$ -Ketoglutarate	Isocitrate dehydrogenase	icd	EC:1.1.1.42	9.5×10	2.0×10 <sup>2</sup>	PMID: 8141; 36923; 2200929	3.3×10	3.3×10
<b>J<sub>4</sub></b>	$\alpha$ -Ketoglutarate $\rightarrow$ Succinyl-CoA	$\alpha$ -Ketoglutarate dehydrogenase complex E1 component	suc A suc B <sup>‡</sup>	EC:1.2.4.2, EC:2.3.1.61	1.9×10 <sup>2</sup>	1.5×10 <sup>2</sup>	PMID: 6380583; 4588679	1.3×10 <sup>2</sup>	1.3×10 <sup>2</sup>
	Succinyl-CoA $\leftrightarrow$ Succinate	Succinyl-CoA synthetase	suc C suc D	EC:6.2.1.5	1.6×10 <sup>2</sup>	9.1×10	PMID: 5338130	1.0×10 <sup>2</sup>	1.0×10 <sup>2</sup>
	Succinate $\rightarrow$ Fumarate	Succinate dehydrogenase	sdh A sdh B <sup>‡</sup>	EC:1.3.5.1	1.0×10 <sup>2</sup>	1.1×10 <sup>2</sup>	PMID: 4334990; 16484232	1.1×10 <sup>2</sup>	1.1×10 <sup>2</sup>
	Fumarate $\leftrightarrow$ Malate	Fumarase	fumA <sup>‡</sup>	EC:4.2.1.2	2.0×10 <sup>2</sup>	1.2×10 <sup>3</sup>	PMID: 3282546; 12021453	4.9×10 <sup>2</sup>	4.9×10 <sup>2</sup>
	Malate $\leftrightarrow$ Oxaloacetate	Malate dehydrogenase	mdh	EC:1.1.1.37	6.1×10	5.5×10 <sup>2</sup>	doi:10.1016/0076-6879(69)13029-3	6.6×10	6.6×10
<b>J<sub>5</sub></b>	Phosphoenolpyruvate $\rightarrow$ Oxaloacetate	Phosphoenolpyruvate carboxylase	ppc	EC:4.1.1.31	4.0×10 <sup>2</sup>	1.5×10 <sup>2</sup>	PMID: 9927652; 4932977	/	1.5×10 <sup>2</sup>
<b>J<sub>6</sub></b>	Acetyl-CoA $\leftrightarrow$ Acetyl phosphate	Phosphate acetyltransferase	pta	EC:2.3.1.8	7.7×10	3.0×10	PMID: 20236319	3.7×10 <sup>2</sup>	3.7×10 <sup>2</sup>
	Acetyl phosphate $\leftrightarrow$ Acetate	Acetate kinase	ackA	EC:2.7.2.1	4.3×10	3.6×10 <sup>3</sup>	EcoCyc: EG10027; PMID: 24801996	3.3×10 <sup>2</sup>	3.3×10 <sup>2</sup>
	Acetate (intracellular) $\leftrightarrow$ Acetate (extracellular)	Acetate transporter	actP	/	2×10	4.7×10 <sup>2</sup>	PMID: 31405984 (Estimated)	/	4.7×10 <sup>2</sup>
<b>J<sub>7</sub></b>	Pyruvate $\rightarrow$ Phosphoenolpyruvate	Pyruvate, water dikinase	ppsA	EC:2.7.9.2	2.5×10 <sup>2</sup>	3.5×10	PMID: 4319237	/	3.5×10

$J_A$	Glucose-6P (extracellular) $\rightarrow$ Glucose-6P (intracellular)	Glucose-6-phosphate transporter	UhpT	/	5×10	2×10 <sup>2</sup>	PMID: 3283129; 2197272; 20018695 (Estimated)	/	2×10 <sup>2</sup>
	Glucose (extracellular) $\rightarrow$ Glucose-6P	Glucose-specific PTS enzyme	ptsG	EC: 2.7.1.199	5×10	1×10 <sup>2</sup>	PMID: 9575173; 20018695; 12146972	/	1×10 <sup>2</sup>
	Lactose (extracellular) $\rightarrow$ Lactose (intracellular)	Lactose transporter	lacY	/	4.6×10	6×10	PMID: 6444453; 20018695	/	6×10
	Lactose $\rightarrow$ Glucose + Galactose	$\beta$ -galactosidase	lacZ	EC:3.2.1.23	4.6×10 <sup>2</sup>	6.4×10 <sup>2</sup>	PMID: 8008071; 23011886 (Estimated)	/	6.4×10 <sup>2</sup>
$J_{py}$	Pyruvate (extracellular) $\rightarrow$ Pyruvate (intracellular)	Pyruvate transporter	btsT CstA	/	8×10	6×10	PMID:20018695; 33260635; EcoCyc: G7942; EG10167 (Estimated)	/	6×10

<sup>†</sup> The classification of  $J_i$  follows the coarse-grained models shown in Figs. 1b and 3e.

\* In vivo  $k_{cat}$  values were obtained using experimental data shown in Table S2 combining with Eq. S134-S135.

<sup>‡</sup> See Fig. S1b for more genes which may play a secondary role.

**Table S2. Proteome and flux data<sup>10</sup> used to calculate the in vivo  $k_{\text{cat}}$ .**

	Culture 1	Culture 2	Culture 3	Culture 4
<b>Growth rate <math>\lambda^*</math> (h<sup>-1</sup>)</b>	0.82	0.87	0.97	1.03
<b><math>J_{\text{ac}}^{(N)*}</math> (mM OD<sub>600</sub><sup>-1</sup> h<sup>-1</sup>)</b>	0.39	1.18	2.68	2.84
<b><math>J_{\text{CO}_2, \text{r}}^{(N)*}</math> (mM OD<sub>600</sub><sup>-1</sup> h<sup>-1</sup>)</b>	7.44	6.05	4.30	3.04
<b>Gene name</b>	<b>Protein fraction obtained using absolute abundance (<math>\phi_i</math>)</b>			
pgi	0.09%	0.09%	0.10%	0.11%
pfkA	0.06%	0.06%	0.06%	0.06%
fbaA	0.32%	0.35%	0.35%	0.39%
tpiA	0.12%	0.15%	0.13%	0.18%
gapA	1.19%	1.29%	1.33%	1.47%
pgk	0.30%	0.31%	0.32%	0.36%
gpmA	0.15%	0.15%	0.15%	0.16%
eno	0.63%	0.70%	0.75%	0.83%
pykF	0.15%	0.15%	0.18%	0.21%
aceE	0.30%	0.32%	0.34%	0.41%
gltA	0.88%	0.80%	0.61%	0.48%
acnB	0.92%	0.84%	0.66%	0.57%
icd	1.55%	1.55%	1.31%	1.39%
suc A				
suc B	0.71%	0.75%	0.64%	0.55%
suc C				
suc D	0.88%	0.84%	0.66%	0.52%
sdh A				
sdh B	0.49%	0.45%	0.42%	0.35%
fumA	0.24%	0.21%	0.17%	0.13%
mdh	0.45%	0.45%	0.41%	0.39%
pta	0.10%	0.10%	0.10%	0.10%
ackA	0.06%	0.07%	0.06%	0.06%

<sup>†</sup> For calibration purposes, a factor of 1.03/0.97 was multiplied on the reference data<sup>10‡</sup>.

<sup>\*</sup> For calibration purposes, a factor of 2.84/3.24 was multiplied on the reference data<sup>10‡</sup>.

<sup>‡</sup> Here, (1.03, 2.84) and (0.97, 3.24) are both the data for ( $\lambda$  (h<sup>-1</sup>),  $J_{\text{ac}}$  (mM OD<sub>600</sub><sup>-1</sup> h<sup>-1</sup>)) of *E. coli* strain NCM3722 cultured with lactose in the same reference<sup>10</sup>. The former is specified in the source data of the reference's figure 1<sup>10</sup>, while the latter is recorded in the reference's extended data figure 3a<sup>10</sup>. With the above calibrations, the data for  $J_{\text{ac}}^{(N)}$ -  $\lambda$  relation shown here align to the same curve as that depicted in Fig. 1c.

## Supplementary Figures

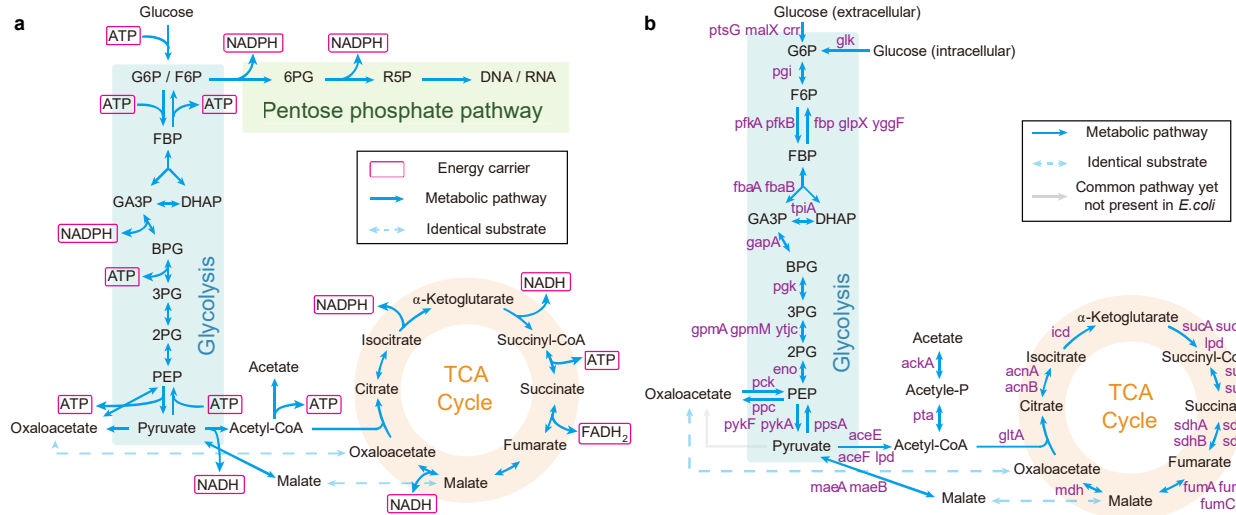


**Fig. S1. Details of the central metabolic network.**

(a) The energy production details of the central metabolic network. In *E. coli*, NADPH and NADH are interconvertible<sup>8</sup>, and all the energy carriers can be converted to ATP with ADP. The conversion factors are: NADH=2ATP, NADPH=2ATP, FADH<sub>2</sub>=1ATP<sup>7</sup>. (b) Relevant genes for enzymes in the central metabolic network.

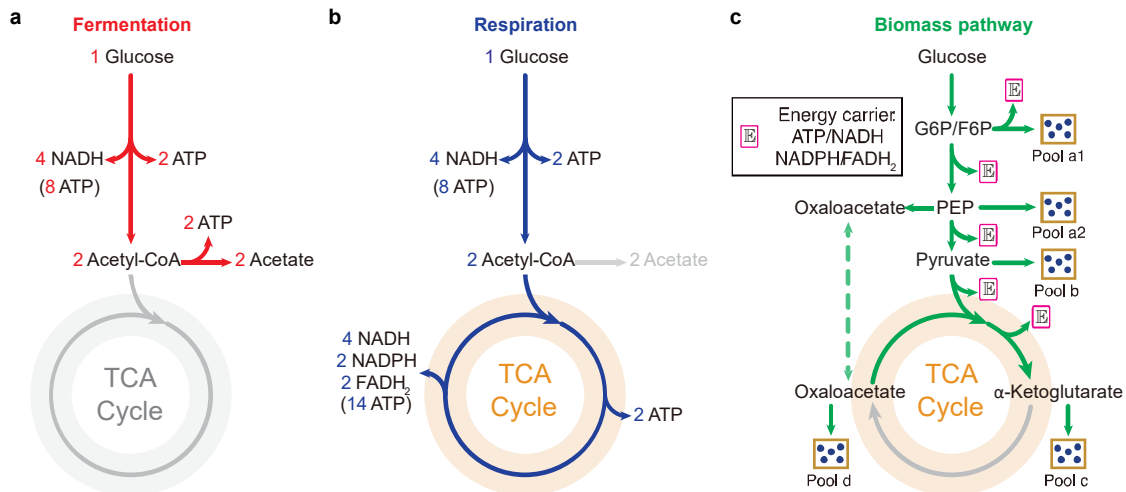


**Fig. S2. Three destinies of glucose metabolism.**

(a) The fermentation pathway, where a molecule of glucose generates 12 ATPs in *E. coli*. (b) The respiration pathway, where a molecule of glucose generates 26 ATPs. (c) The biomass pathway, where the glucose turns into precursors of biomass. Note that there is accompanied ATPs production in the biomass generation process (see Sec. 2.1).

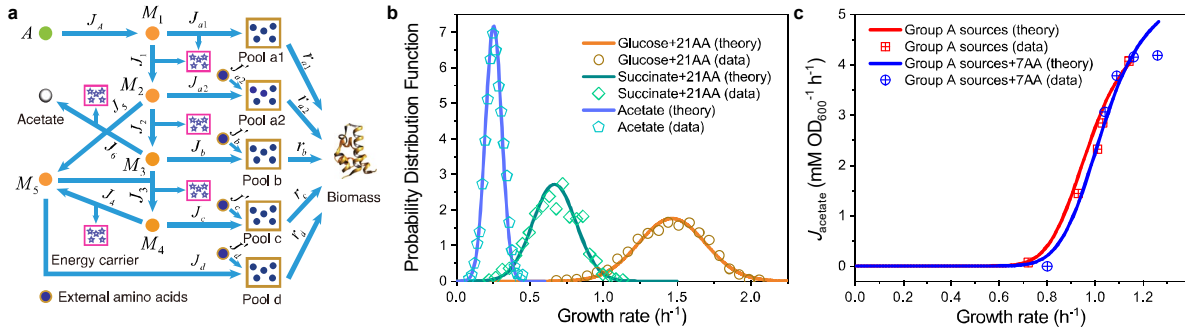


**Fig. S3. Model analysis for carbon utilization in mixtures with amino acids.**

(a) The coarse-grained model for the case of a Group A carbon source mixed with extracellular amino acids. (b) Model predictions (see Eqs. S157, S164-S165) and single-cell reference experimental results<sup>16</sup> of the growth rate distributions for *E. coli* in three culturing conditions. (c) Comparison of the growth rate-fermentation flux relation for *E. coli* in Group A carbon sources between minimum media and enriched (those with 7AA) media.

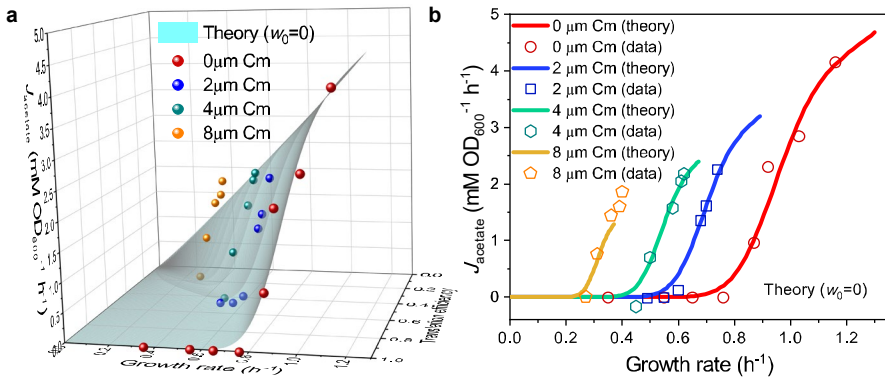


**Fig. S4. Influences of translation inhibition on overflow metabolism.**

(a) 3D plot of the relations among the fermentation flux, growth rate and the translation efficiency (Eqs. 79 and S160). (b) The growth rate dependence of acetate excretion rate as  $K_A$  varies, with each fixed dose of Cm. The translation efficiency is tuned by the dose of Cm, and the maintenance energy coefficient is set to be 0 ( $w_0 = 0$ ).

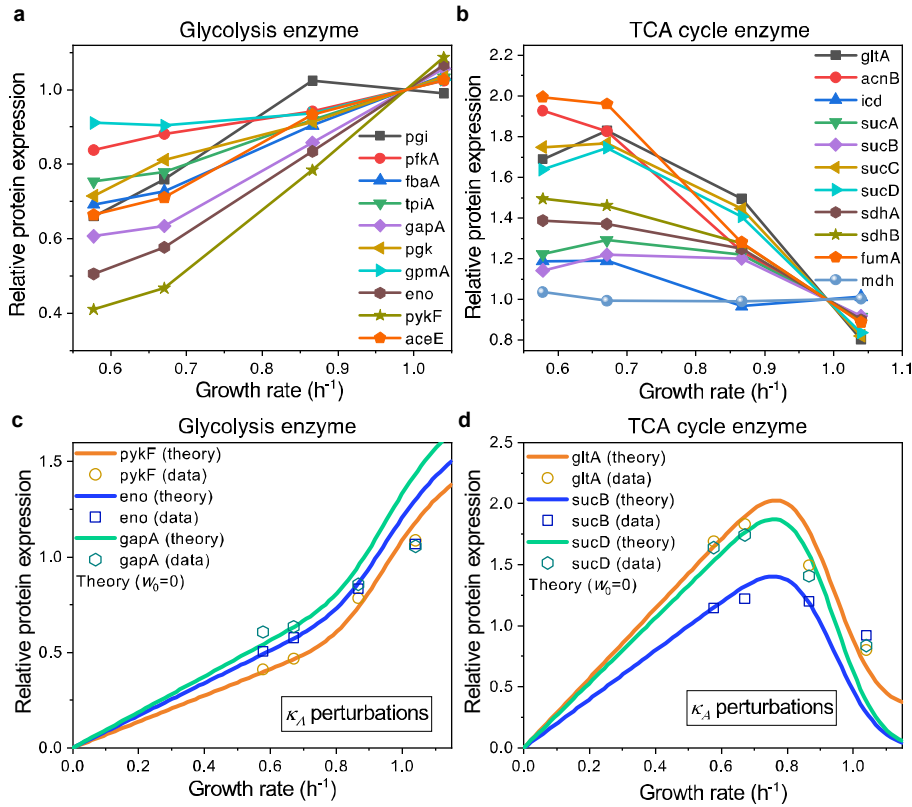


**Fig. S5. The relative protein expression of central metabolic enzymes under  $\kappa_A$  perturbations**

(a) Experimental data<sup>17</sup> of the catalytic enzymes for each step of glycolysis. (b) Experimental data<sup>17</sup> of the catalytic enzymes for each step of the TCA cycle. (c) Model predictions (Eq. S118) and experimental data<sup>17</sup> of representative genes from glycolysis. (d) Model predictions (Eq. S118) and experimental data<sup>17</sup> of representative genes from the TCA cycle. We apply  $W_0 = 0$  for the model settings in (c) and (d).

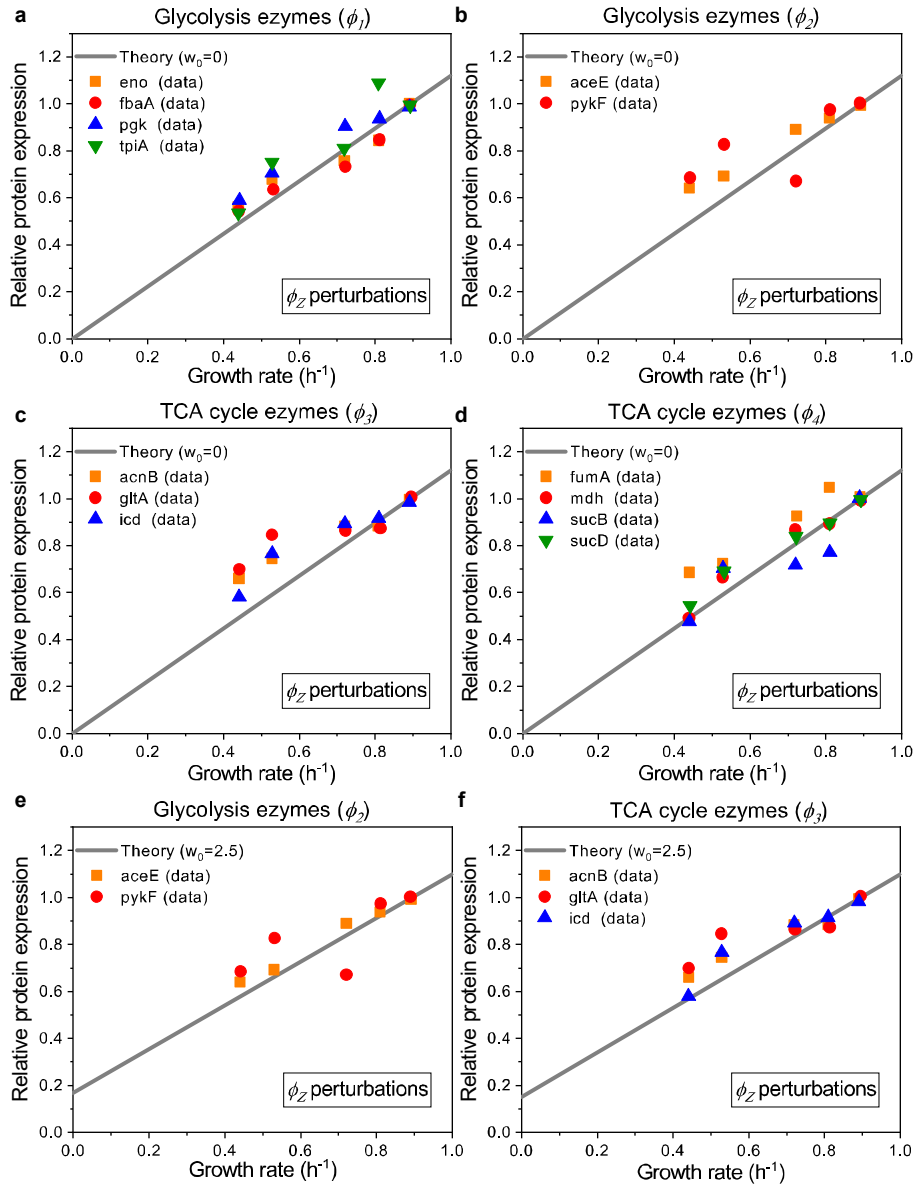


**Fig. S6. The relative protein expression of central metabolic enzymes under  $\phi_Z$  perturbations.**

(a, b, e) Model predictions and experimental data<sup>10</sup> of representative genes from glycolysis. (c, d, f) Model predictions and experimental data<sup>10</sup> of representative genes from the TCA cycle. (a-d) Results of  $\phi_Z$  perturbations with  $w_0 = 0$  (Eq. S120). (d) Results of  $\phi_Z$  perturbations with  $w_0 = 2.5$  (Eq. S121).

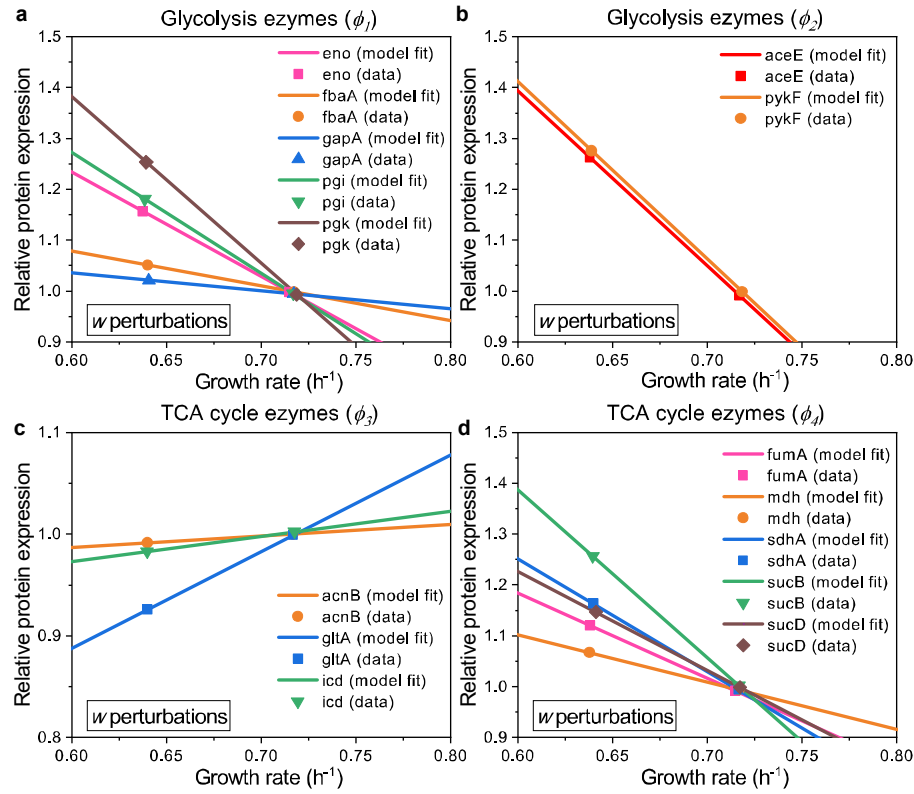


**Fig. S7. The relative protein expression of central metabolic enzymes upon energy dissipation.**

(a-b) Model fits (see Eqs. S127 and S123) and experimental data<sup>10</sup> of representative genes from glycolysis.  
 (c-d) Model fits (see Eqs. S127 and S123) and experimental data<sup>10</sup> of representative genes from the TCA cycle.

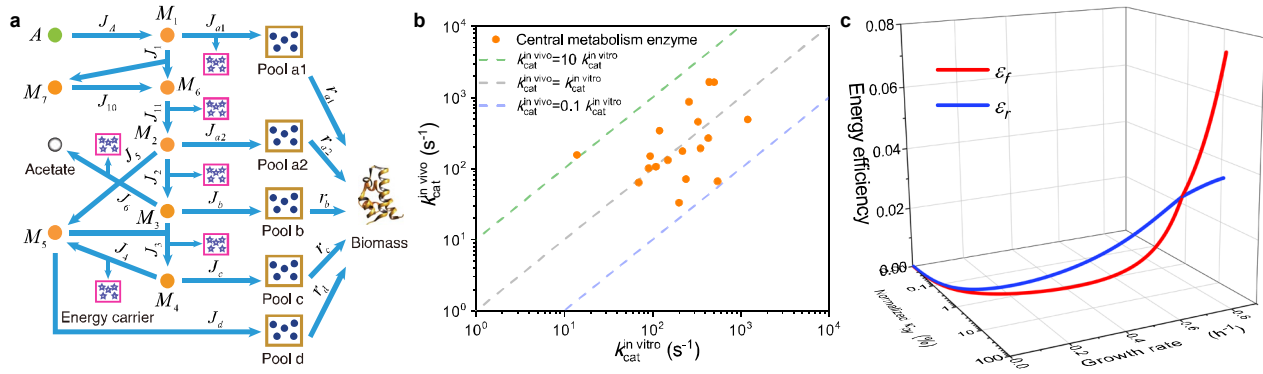


**Fig. S8. A coarse-grained model for experimental comparisons.**

(a) The coarse-grained model for Group A carbon source utilization. This model includes more details to compare with experiments. (b) Comparisons between the in vivo and in vitro catalytic rates for enzymes within glycolysis and the TCA cycle (see Table S1 for details). (c) The energy efficiencies of respiration and fermentation pathway vary with the growth rate as functions of the substrate quality of pyruvate (Eq. S93).

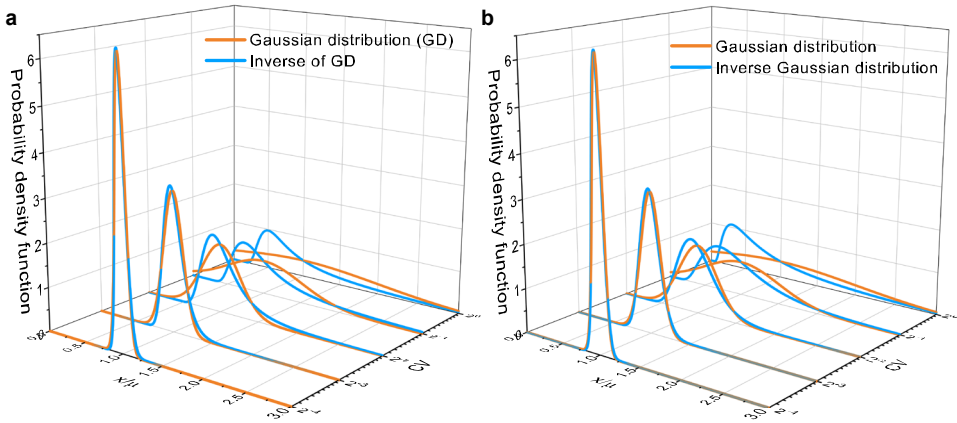


**Fig. S9. Asymptotic distributions of inverse Gaussian distribution and the inverse of Gaussian distribution.**

(a) Comparisons between the inverse of Gaussian distribution and the corresponding Gaussian distribution for each value of coefficient of variance (CV) (Eqs. S140 and S145). (b) Comparisons between inverse Gaussian distribution and the corresponding Gaussian distribution for each value of CV (Eqs. S142 and S146). Both inverse Gaussian distribution and the inverse of Gaussian distribution converge into Gaussian distributions when CV is small.